Near-Black Body Technology

for cheaper, more efficient,
more convenient energy conversion systems

What is a 'near-black body'?

A black body is an object that completely absorbs all incident radiation without reflection or transmission. A near-black body is a black body-like material or device which absorbs radiation emitted from any light source, including the sun, as much as possible. A near-black body can be used for high efficiency solar cells, detectors, etc.

Why IMCM at KIST?

The Institute for Multi-disciplinary Convergence of Materials (IMCM) at KIST is taking on the challenge of developing near-black body matters and systems in response to global energy agendas, by combining scientific knowledge and experience gained from KIST's involvements in the development and commercialization of innovative materials across various research areas.

KIST IMCM's Research Areas

- Materials Architecturing
- Opto-Electronic Conversion Systems
- Computational Science

The Fifth National Seal of Korea
Created using advanced
technolgies developed by KIST

TECHNICAL REVIEW •Current Status and Perspectives of Proteomics Research •DNA-Based Biosensor Array Chip and Sensing System Using CMOS Technology •Supercritical Fluid Technology: A Green Chemical Process for the 21st Century
FEATURE ARTICLES •Microcantilever Nanomechanical Sensor for Biomolecule Analysis •Daurinol as a Potent Anticancer Compound with Low Side Effects Derived from a Mongolian Medicinal Plant •Development of Methods for the Early Diagnosis of Ankylosing Spondylitis •Method for Suppressing Beat Noise in Brillouin Distributed Temperature and Strain Sensing •Controlling Liquid Behavior by Tuning Surface Wettability •Electric Actuation of Nanostructured Thermoplastic Elastomer Gels with Ultralarge Electrostriction Coefficient •Development of Efficient and Stable Organic Solar Cells •Sensitive and Advanced Methods for Detecting Thyroid Hormonal Changes •Extracellular Electron Shuttle Mediated Biodegradation of Explosive Compounds and Its Application to Multi-Contaminant Removal
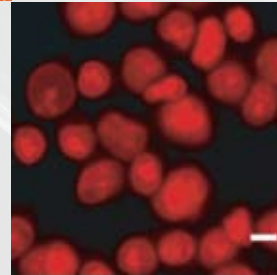
contents

FOREWORD

Korea was the only country among the developing countries in the 1960s determined to pursue the development of science and technology for its national growth. At the time, eighteen scientists with elite research backgrounds chose to return to their home country of Korea so that Korea could take the first step towards science and technology. A half a century later, KIST's role in paving the way for Korea's economic growth at an unprecedented pace has cemented itself in Korea's history. Its world-leading achievements in various industries, including the steel, shipbuilding, semiconductor and motor industries, have planted hope for other countries to follow in the footsteps of KIST.

KIST will continue to move forward in the next half century with new visions and goals, by equipping itself with a competitive edge on a global scale. If it was passion for science and technology in the 1960s that enabled the success of KIST and Korea's development, today KIST will create new history by becoming the hope for the world and by contributing to the growth and prosperity of the international community.

Since the first summer issue of 2008, KISToday has provided the latest news regarding KIST and its research activities to scientists all over the world. Now a new and improved KISToday with more contents will aim to tell new stories of KIST as it grows its readership to a wider audience.

KISToday will be covering the latest, cutting-edge research of KIST's numerous research divisions including the Brain Science Institute, Biomedical Research Institute, Institute for Multi-disciplinary Convergence of Materials, Green City Technology Institute, Future Convergence Research Division, and National Agenda Research Division. Moreover, KISToday will cover various stories and topics ranging from current news to the philanthropic activities of KIST members.

Through KISToday, you will be able to see KIST in a new light as it continues to engage in passionate and creative research in the current age of globalization with the same level of commitment the early KIST scientists had shown when they first planted the seeds of science and technology in Korea a half century ago.

Kil-Choo Moon
President

Current Status and Perspectives of Proteomics Research

Ji Eun Lee
Center for Theragnosis
• jelee9137@kist.re.kr

Cheol Ju Lee
Center for Theragnosis
• chlee270@kist.re.kr

Introduction

The use of mass spectrometry (MS) in proteomics research has been established as an indispensable tool for improving our understanding of molecular and cellular biology. Over the last decade, dramatic advances have been made in MS instrumentation, data analysis, and methods of sample separation. The focus of this technical review is to show how proteomic analysis using MS is currently conducted, and what the future direction of proteomics research is likely to be.

Background

Proteomics is the study of proteome which is the entire set of proteins expressed in a cell, tissue, or organism. Its purpose is to determine protein structures and functions in order to better understand biological systems. Proteins are vital parts of living organisms, affecting many biological phenomena such as diseases and aging. In comparison with gene products, the complexity of protein is significantly greater due to alternative splicing and post-translational modifications (PTMs). Single nucleotide polymorphisms (SNPs) is another main source of increasing protein heterogeneity, and similar genes also give rise to the expression of protein isoforms that have very similar amino acid sequences (see Figure 1).
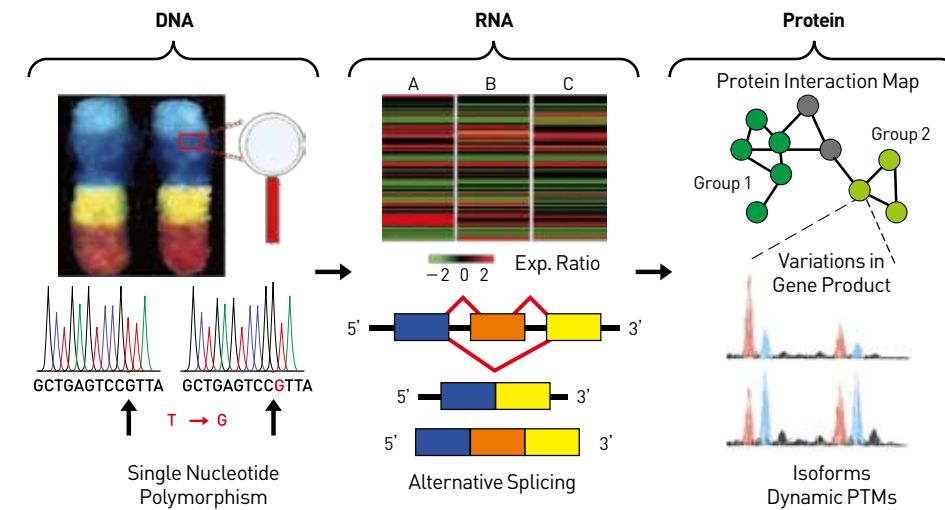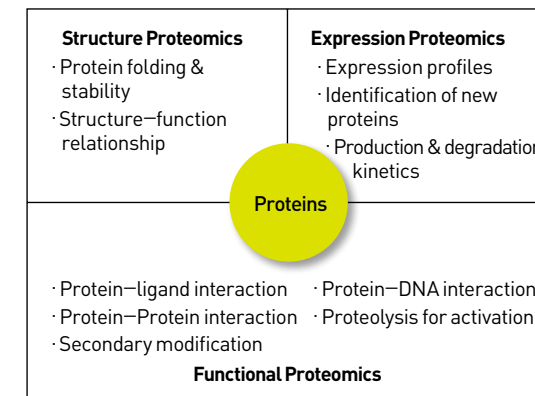

FIGURE 1 Protein complexity arising from a combination of molecular variation including SNP, alternative splicing, and PTMs [1]

While proteomics generally focuses on exploring protein expression, function, structure, cellular localization, and protein-protein interactions, it can be divided into three research fields as follows: structural proteomics, expression proteomics, and functional proteomics (see Figure 2) [2]. Structural proteomics attempts to investigate protein folding and three-dimensional structures by use of X-ray crystallography and NMR. Functional proteomics based on protein chip technologies mainly aims to elucidate the protein-protein interactions which are involved in cell signaling processes. Finally, expression proteomics includes protein identification and protein expression profiling by use of mass spectrometry (MS). Over the last 10 years, MS-based proteomics has made great advances in determining the primary structures of proteins and quantities of expressed proteins in a specific cell state and characterizing PTMs. In this technical review, we will examine the current status and perspectives of MS-based proteomic research.

Protein identification based on MS can be performed by either a bottom-up or top-down approach, as seen in Figure 3. In the bottom-up approach, proteins are digested with a protease such as trypsin, and proteolytic peptides are analyzed by use of mass spectrometry. After the masses of the proteolytic peptides are determined, the peptide ions are fragmented in a gas phase to produce information on the pep-

Structure Proteomics	Expression Proteomics
· Protein folding & stability · Structure–function relationship	· Expression profiles · Identification of new proteins · Production & degradation kinetics
· Protein–ligand interaction · Protein–Protein interaction · Secondary modification	· Protein–DNA interaction · Proteolysis for activation
Functional Proteomics	

Proteins

FIGURE 2 Types of proteomics

FIGURE 3 Bottom-up and top-down approaches for MS-based protein analysis [3]

FIGURE 4 Multidimensional Protein Identification Technology (MudPIT)
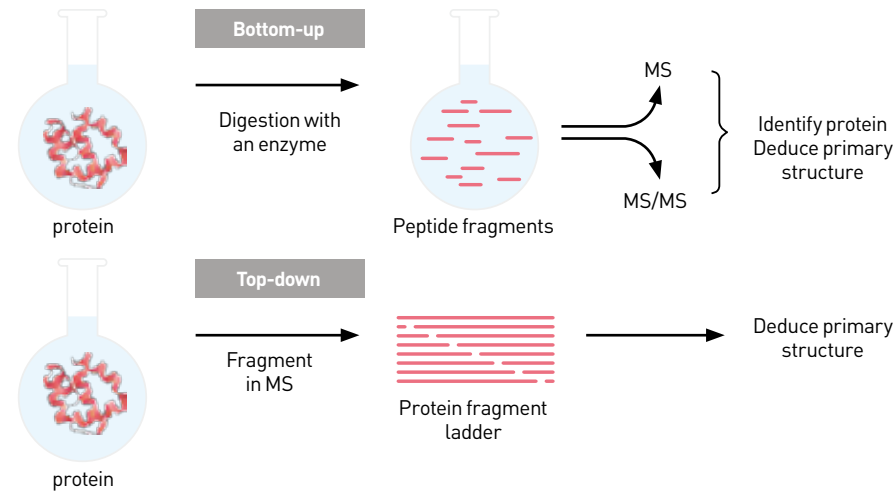
tide sequence and modifications. Then the peptides are matched to proteins through database searching processes. Since the bottom-up approach has made such great advances over the past 10 years, this approach is widely used for proteomic analysis in many laboratories because of the efficiency of peptide analysis in comparison with intact protein measurement.

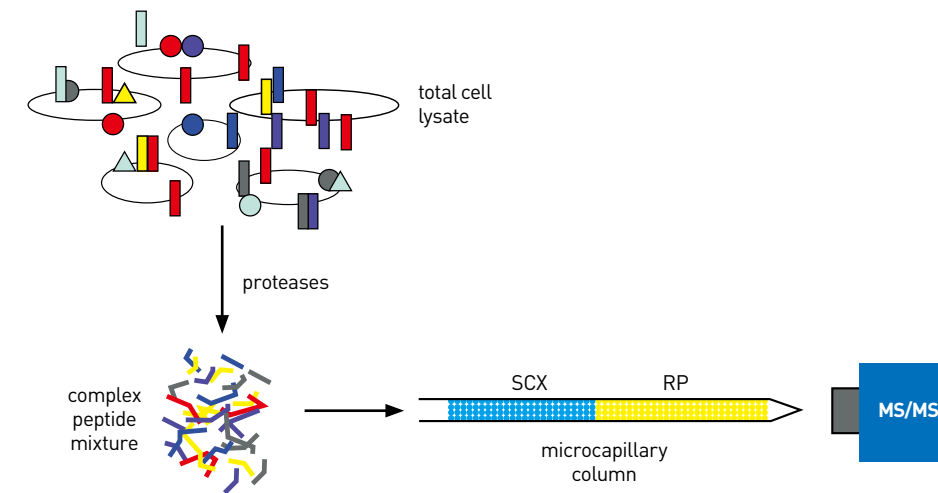In the top-down approach, intact proteins are directly ionized and subsequently fragmented in a mass spectrometer, thereby yielding the molecular masses of both the proteins themselves as well as their fragment ions. The top-down approach has the advantage of providing a complete description of the primary structure of the proteins along with PTM information, which allows for differentiating protein isoforms that have very similar amino acid sequences. In the top-down approach, one major challenge is the need to separate small quantities of complex mixtures of proteins before mass spectrometric analysis. Intact protein analysis based on the top-down approach has, therefore, traditionally focused on analyzing single protein targets rather than complex protein mixtures. Recently, techniques for analyzing complex proteomic mixtures by use of the top-down approach has greatly improved owing to advances in protein separation technologies.

A typical proteomic experiment consists of the following steps: (i) separation of proteins or peptides; (ii) acquisition of protein primary structures by use of MS; and (iii) protein identification.
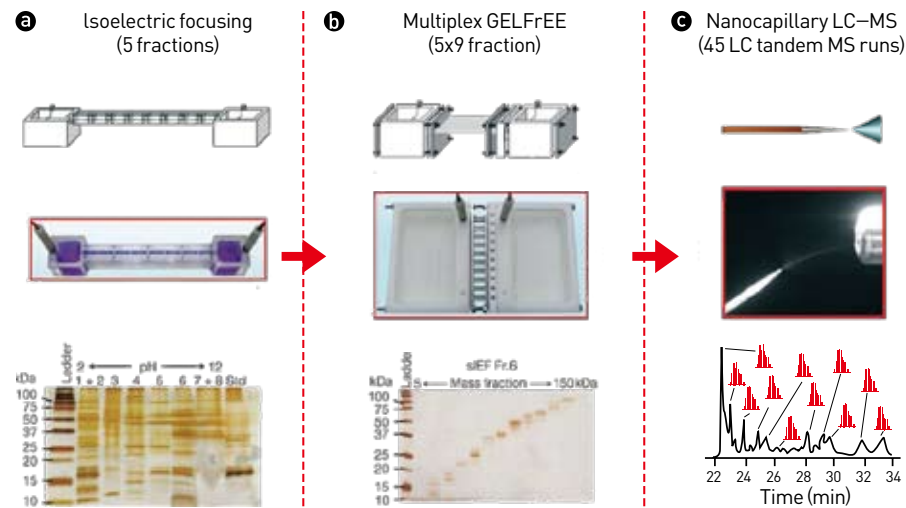
Separation science

Given the enormous complexity of proteomic mixtures, which can range from sub-
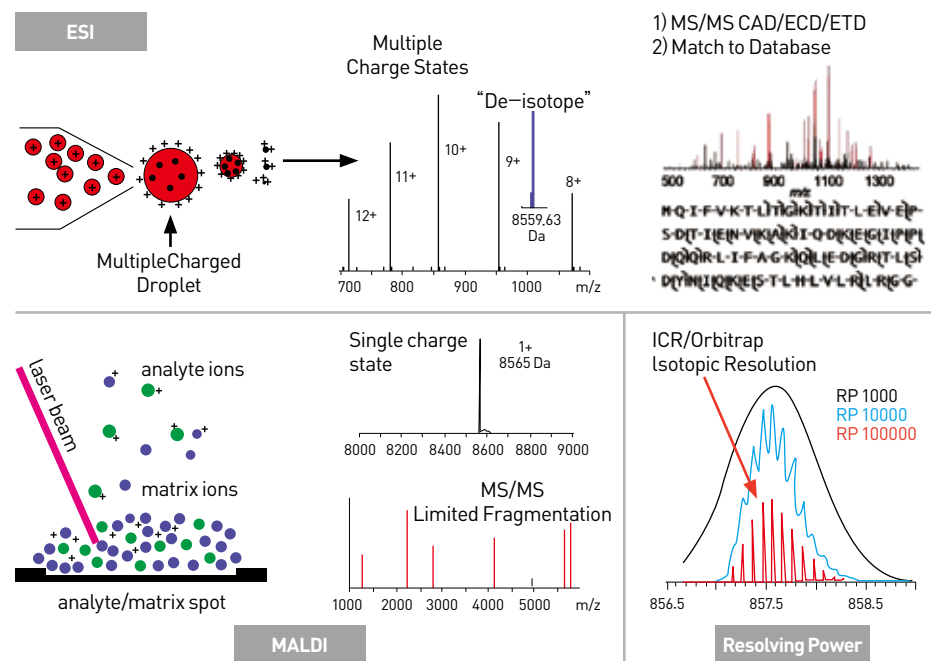
organellar complexes to whole-cell proteomics, mass spectrometry alone is not sufficient to characterize a proteome. Effective separations are critical to decrease the sample complexity and to increase the dynamic range of detection. For protein separations, one- or two-dimensional polyacrylamide gel electrophoresis (1D-PAGE or 2D-PAGE) has been traditionally used. In 1D-PAGE, proteins are separated on the basis of molecular weight. In 2D-PAGE, proteins are separated according to their net charge by isoelectric focusing in the first dimension and according to their molecular mass in the second dimension [4]. In the case of 2D-PAGE, several thousand proteins can be resolved in a single slab gel, and some protein forms that have PTMs, such as phosphorylation, can be resolved. The gel bands or spots, which are differentially expressed in different sample conditions, are usually excised and digested with a protease such as trypsin in order to generate the proteolytic peptides. 1D- or 2D-PAGE is typically used in a bottom-up approach because extraction of intact proteins for performing top-down proteomic analysis has a low recovery rate. Since 1D- and 2D-PAGE separation is often a laborious and time-consuming process, non-gel techniques, such as multidimensional protein identification technology (MudPIT), have been introduced for the bottom-up approach as a separation option (see Figure 4) [5]. That is, complex protein mixtures are first digested with proteases such as trypsin and then the resulting proteolytic peptides are subjected to 2D-liquid chromatography separation consisting of strong cation exchange chromatography followed by reversed phase liquid chromatography, thus allowing for identification of thousands of proteins by the bottom-up approach. In the top-down approach, effective protein separation is absolutely critical to successfully analyze complex protein mixtures. While the top-down approach for complex proteome analysis was previously hampered by the "front

FIGURE 5 Multidimensional protein separation in a solution phase allowing for comprehensive top-down proteomic analysis

ⓐ Isoelectric focusing (5 fractions)
ⓑ Multiplex GELFrEE (5x9 fraction)
ⓒ Nanocapillary LC—MS (45 LC tandem MS runs)

FIGURE 6 Soft ionization methods of peptides and proteins

Acquisition of protein primary structures by use of MS

For biological samples to be analyzed by MS, peptides or proteins must first be ionized. The two most common methods for ionization are electrospray ionization (ESI) and matrix-assisted laser desorption/ionization (MALDI) (see Figure 6) [1]. ESI and MALDI are "soft" ionization methods allowing the formation of ions without significant loss of sample integrity. In both methods, peptides or proteins are converted to ions by the addition or loss of one or more protons. In ESI, a liquid sample flows from a micro-capillary tube into the mass spectrometer, where a potential difference between the capillary and the inlet to the mass spectrometer results in the generation of multiply charged ions. By contrast, in MALDI, the peptide or protein sample is incorporated into matrix molecules and then subjected to irradiation by a laser which promotes the formation of singly charged molecular ions. MALDI has increased tolerance to salts and detergents by comparison to ESI. After peptides or proteins are converted to molecular ions via either ESI or MALDI, the ions are resolved on the basis of their mass and charge in a vacuum. The different instrumental configurations of the mass analyzers are seen in Figure 7 [7]. In time-of-flight (TOF) instruments, the ions are accelerated to high kinetic energy and are separated along a flight tube as a result of their different velocities. In a quadrupole mass analyzer, ions are transmitted through an electric field created by an array of four parallel metal rods. That is, a quadrupole can act to transmit all ions or as a mass filter to allow the transmission of ions of a certain mass-to-charge (m/z) ratio. Ion trap mass analyzers function to trap molecular ions in a 3-D electric field. The main advantage of an ion trap mass analyzer is its ability to allow ions to be stored and then selectively ejected from the ion trap, thereby increasing sensitivity. Fourier transform mass spectrometry (FT-MS) along with Orbitrap mass spectrometry are ion-traping techniques that use instruments with high resolution and mass accuracy within 10 ppm. Due to the hig-resolving power, the FT-MS instrument is optimal for intact protein analysis by use of the top-down approach. After the proteolytic peptides (bottom-up approach) or intact proteins (top-down approach) are detected via one of the mass analyzers (Figure 7), the parent ions are further subjected to fragmentation for obtaining amino acid sequence information. After peptides or intact proteins are introduced into the collision chamber, they interact with collision gas such as nitrogen or argon and undergo fragmentation primarily along the peptide backbone via a collision-induced dissociation (CID) mechanism. In addition, electron capture dissociation (ECD) and electron transfer dissociation (ETD) can be used to generate different peptide backbone fragmentation ions.
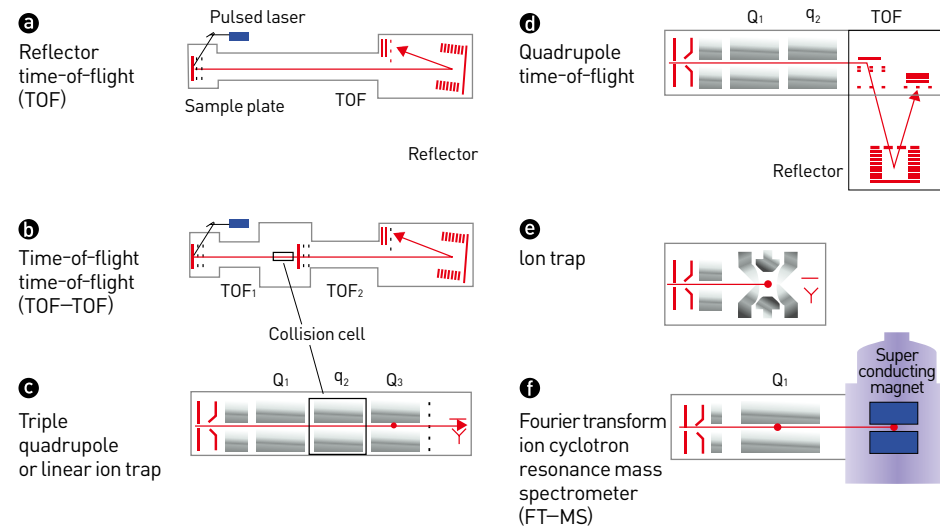
end" problem of sample handling prior to MS, recent advances in protein separation based on a solution phase has enabled researchers to perform comprehensive top-down proteomic analysis. Figure 5 shows that 2-D liquid electrophoresis consisting of solution isoelectic focusing (sIEF) followed by gel-eluted liquid fraction entrapment electrophoresis (GELFrEE) has been successfully used for performing top-down analysis of complex protein mixtures [6].
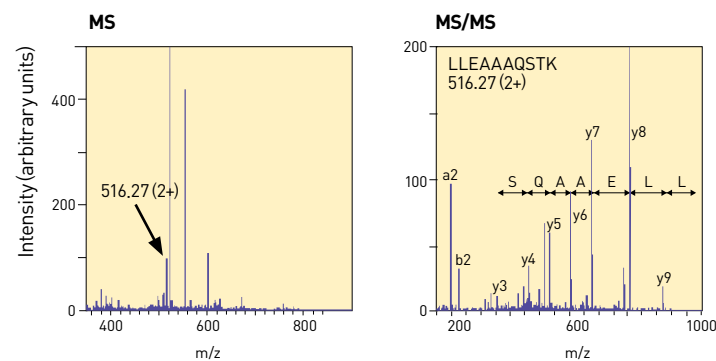
FIGURE 7 Types of mass analyzers used in proteome research

a Reflector time-of-flight (TOF)

Pulsed laser
Sample plate   TOF
Reflector

b Time-of-flight time-of-flight (TOF–TOF)

TOF₁   TOF₂
Collision cell

c Triple quadrupole or linear ion trap

Q₁   q₂   Q₃

d Quadrupole time-of-flight

Q₁   q₂   TOF
Reflector

e Ion trap

f Fourier transform ion cyclotron resonance mass spectrometer (FT–MS)

Q₁
Super conducting magnet

FIGURE 8 MS and MS/MS spectra of a proteolytic peptide originated from a protein

MS

516.27 (2+)

MS/MS

LLEAAAQSTK
516.27 (2+)

Protein identification

After mass spectral data is obtained from biological samples, proteins are identified through database searching processes. One method of protein identification is peptide mass fingerprinting (PMF) [4]. In this method, instead of acquiring MS/MS data from the parent peptide ions, the masses of peptides obtained from the proteolytic digestion of an unknown protein are compared to the predicted masses of peptides from the theoretical digestion of proteins in a database. If enough peptides from the real mass spectrum and the theoretical one overlap, protein identification can be made. Since no fragment information is available from the PMF method, it is critical to obtain an accurate measurement of the masses of multiple peptides. A more accurate protein identification method is to use peptide fragment information. That is, after the intact parent ion mass is first determined, the peptide amino acid sequence is determined from the fragment spectrum (see Figure 8) [7], and then the protein is identified

FIGURE 9 Common quantitative mass spectrometry workflows
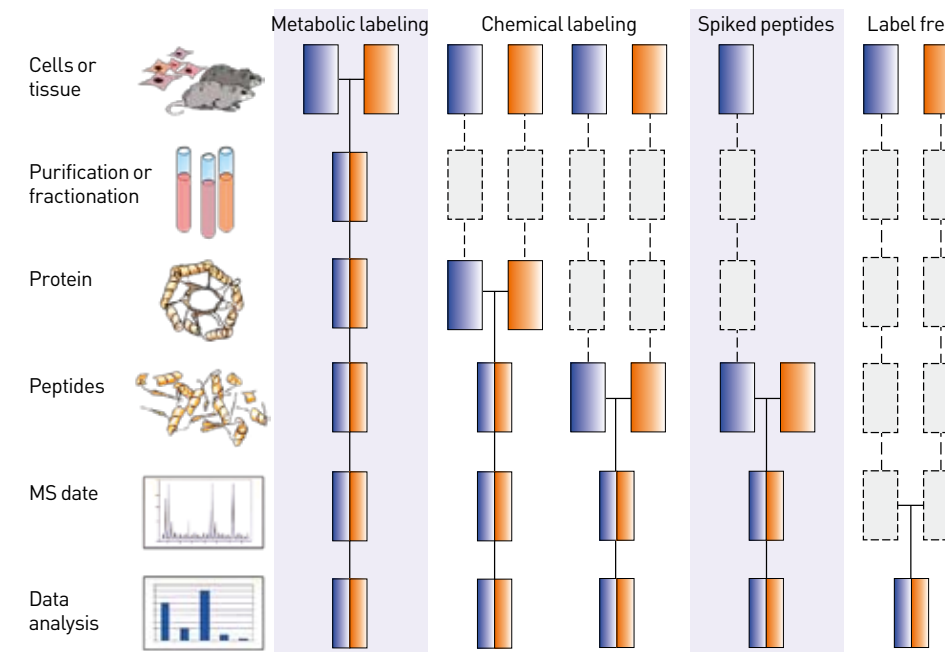
through a database searching process via protein search engines such as SEQUEST and Mascot.

Protein quantification

The most extensively used application of proteomics continues to be protein expression profiling which shows how the proteins are differently expressed. 2D-PAGE was previously used for performing protein expression profiling in different sample conditions, most of which are healthy samples or disease samples. However, due to efficiency and reproducibility issues raised from 2D-PAGE, MS-based quantification has gained increasing popularity. Quantification of proteins based on MS is usually performed either by stable isotope labeling or label-free approaches. Isotope labeling can be introduced as an internal standard into amino acid (i) metabolically, (ii) chemically, or (iii) as an external standard using spiked synthetic peptides as seen in Figure 9 [8]. In the case of chemical labeling, isotope labeling can be performed either on protein levels or peptide levels. Recently, we were able to successfully apply mTRAQ labeling reagents to the proteolytic peptides generated from different conditions of samples for performing quantitative proteomic analysis (see Figure 10) [9]. While stable isotope labeling can allow for accurately determining changes in protein levels, label-free quantitative methods do not require additional chemistry or sample

FIGURE 10 Quantitative analysis by use of mTRAQ-labeled peptides
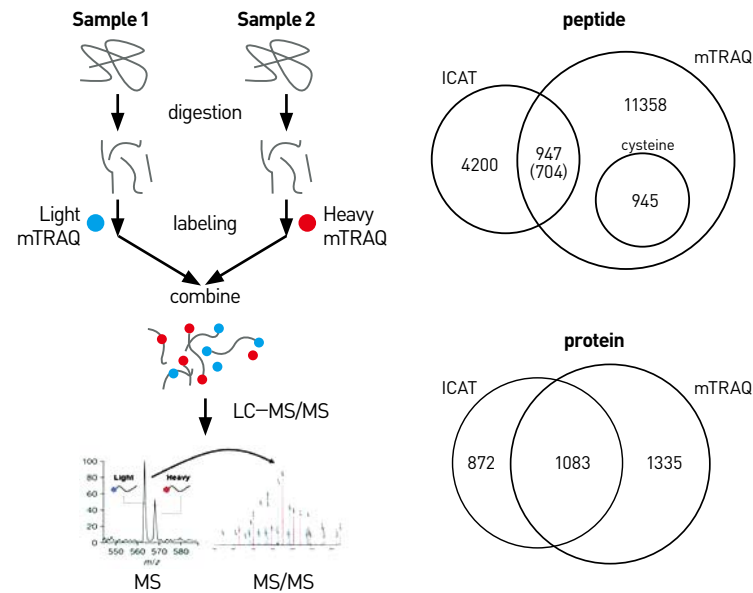
preparation to provide semi-quantitative information. Label-free approaches compare either the mass spectral peak intensities of peptides or the number of MS/MS spectra identifying peptides, an approach referred to as spectral counting. The label-free approach is often applied in order to perform biomarker discovery studies for finding candidate peptides or proteins related to a specific biological phenomenon or disease.

Recently, the importance of targeted quantitative proteomics called selected reaction monitoring (SRM) has also increased. In the SRM method, a proteolytic peptide of interest is first isolated and then fragmented to yield product ions whose signal abundances are indicative of the abundance of the peptide in the sample (see Figure 11). SRM is primarily performed on triple quadrupole mass spectrometers, where mass-resolving Q1 isolates the precursor, Q2 acts as a collision cell, and the fragment ions are detected in mass-resolving Q3. By spiking heavy-labeled (for example, D, 13C, or 15N) peptides to a complex matrix as concentration standards, SRM can be used to construct a calibration curve allowing for absolute quantification

FIGURE 11 Targeted quantitative proteomics based on the SRM method
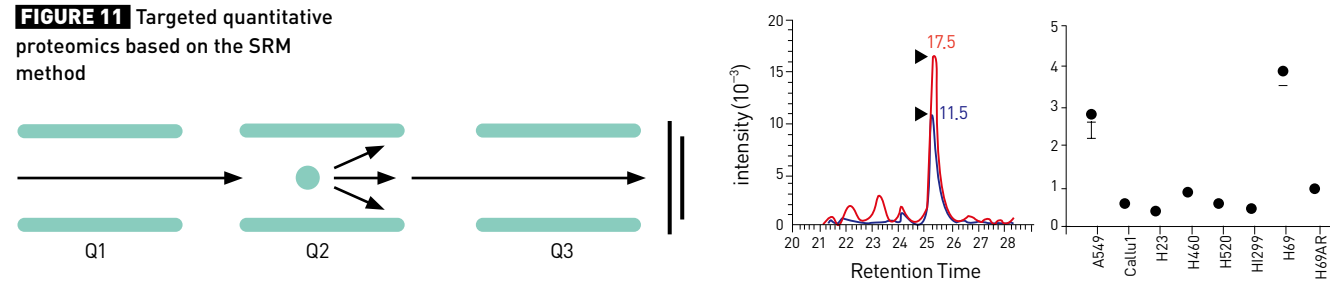
of the peptides. Since SRM involves targeted quantitative proteomics, it is useful for monitoring quantitative changes for low abundant proteins involved in cell signaling processes, cell division, and cell death. The sensitivity of the SRM method is lower than that of enzyme-linked immunosorbent assay (ELISA); however, it is expected that SRM will be a good alternative to ELISA when the antibody for a protein of interest is not available. Using the current SRM platform, 1 pg of proteins can be detected among 1μg of proteome, and the immuno-SRM method can be used to detect the proteins present in lower abundance.

Protein PTM analysis

PTM is the chemical modification of a protein after its translation, and thus cannot be obtained from genomic information. Multi-site PTMs modulate protein activity and protein-protein interactions, affecting fundamental cellular processes, such as cell proliferation and cell death. Protein PTM analysis by use of MS can determine PTM sites and explore PTM changes from different cell state conditions. While the bottom-up approach can be used for analyzing PTMs present on proteins, the full characterization of PTMs of proteins is difficult because proteins are digested with proteases prior to MS analysis and all of the proteolytic peptides cannot be detected. In other words, the top-down approach is best suited for protein PTM analysis. Although the top-down approach was previously performed on PTM characterization for single target proteins, recent advances in top-down proteomics platforms have been able to
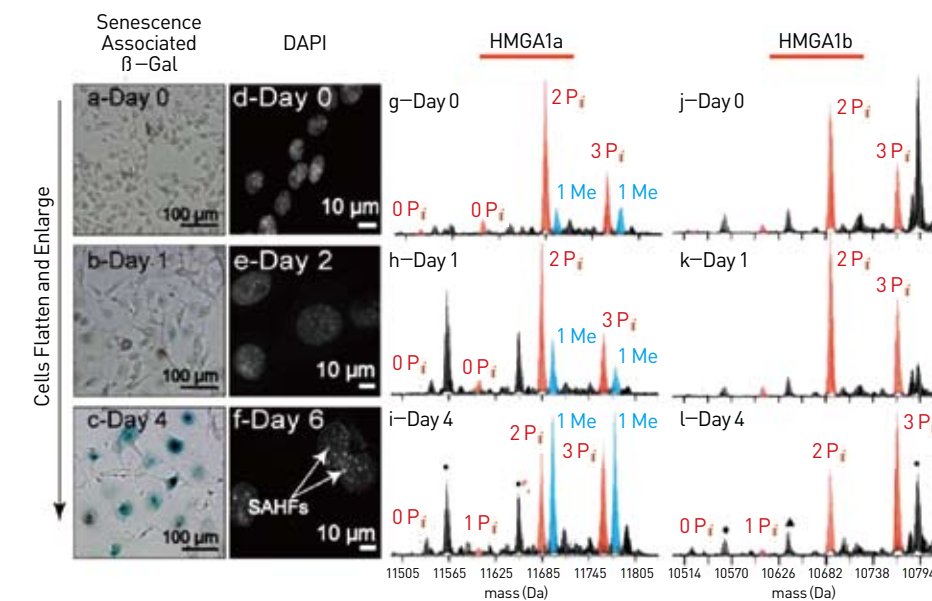
FIGURE 12 PTM dynamics of HMGA protein isoforms during cellular senescence

characterize PTMs and monitor the PTM dynamics of complex proteomic mixtures. Figure 12 represents the PTM dynamics of HMGA protein isoforms during cellular senescence. It can be observed that the PTM dynamics of HMGA 1a and HMGA 1b proteins having very similar amino acid sequences are differentially regulated.

Proteogenomics

While MS-based proteomics has made impressive strides in protein expression profiling and characterization over the last decade, another newly emerging field in proteomics is proteogenomics, which uses proteomic information to improve gene annotations [10]. Human genome sequencing is now complete, but a genome sequence alone is not sufficient for completely understanding biological functions. To fully understand the biological functions associated with a sequenced genome, accurate identification of the protein-coding genes in each genome is required. Since MS-based proteome analysis directly measures the expressed proteins by either a bottom-up or top-down approach, it can verify protein-coding regions of a genomic sequence. In addition, proteogenomics can allow for identification of missed protein-coding genes, confirmation of the expression of alternative splice variants, and determination of protein start and termination sites. Proteogenomics has already been applied to improve the gene annotations of various organisms in humans, the flowering plant Arabidopsis thaliana, and multiple species of Shewanella bacteria. Since tandem MS/MS data is searched against a six-frame translation of the genome sequence, rather than protein database, in proteogenomics, implementation of data mining and informatics tools integrating proteomics data to genomic information is critical.

In summary, MS-based proteomics research has made dramatic advances over the last decade in sample separation methods, MS instrumentation, and data analysis. Current proteomics technologies have enabled the identification of several thousand proteins, characterization of PTMs, and profiling the expression level of proteins in high throughput mode. Thus, proteomics holds great promise for future biomarker discovery associated with disease detection and tracking the outcomes of drug treatments.

References

[1] Tipton JD, Tran JC, Catherman AD, Ahlf DR, Durbin KR, Kelleher NL. J Biol Chem. 2011; 286(29): 25451–25458.
[2] 양혜정, 권대영. 식품기술. 2005; 18: 1–15.
[3] Chait B. Science. 2006; 314: 65–66.
[4] Graves PR, Haystead TA. Microbiol Mol Biol R. 2002; 66: 39–63.
[5] Whitelegge JP. Proc Nat Acad Sci USA. 2002; 99: 11564–11566.
[6] Tran JC, Zamdborg L, Ahlf DR, Lee JE, Catherman AD, Durbin KR, Tipton JD, Vellaichamy A, Kellie JF, Li MX, Wu C, Sweet SM, Early BP, Siuti N, LeDuc RD, Compton PD, Thomas PM, Kelleher NL. Nature. 2011; 480: 254–258.
[7] Aebersold R, Mann M. Nature. 2003; 422: 198–207.
[8] Bantscheff M, Schirle M, Sweetman G, Rick J, Kuster B. Anal Bioanal Chem. 2007; 389: 1017–1031.
[9] Kang UB, Yeom J, Kim H, Lee C. J Proteome Res. 2010; 9: 3750–3758.
[10] Ansong C, Purvine SO, Adkins JN, Lipton MS, Smith RD. Brief Funct Genomic Proteomic. 2008; 7: 50–62.
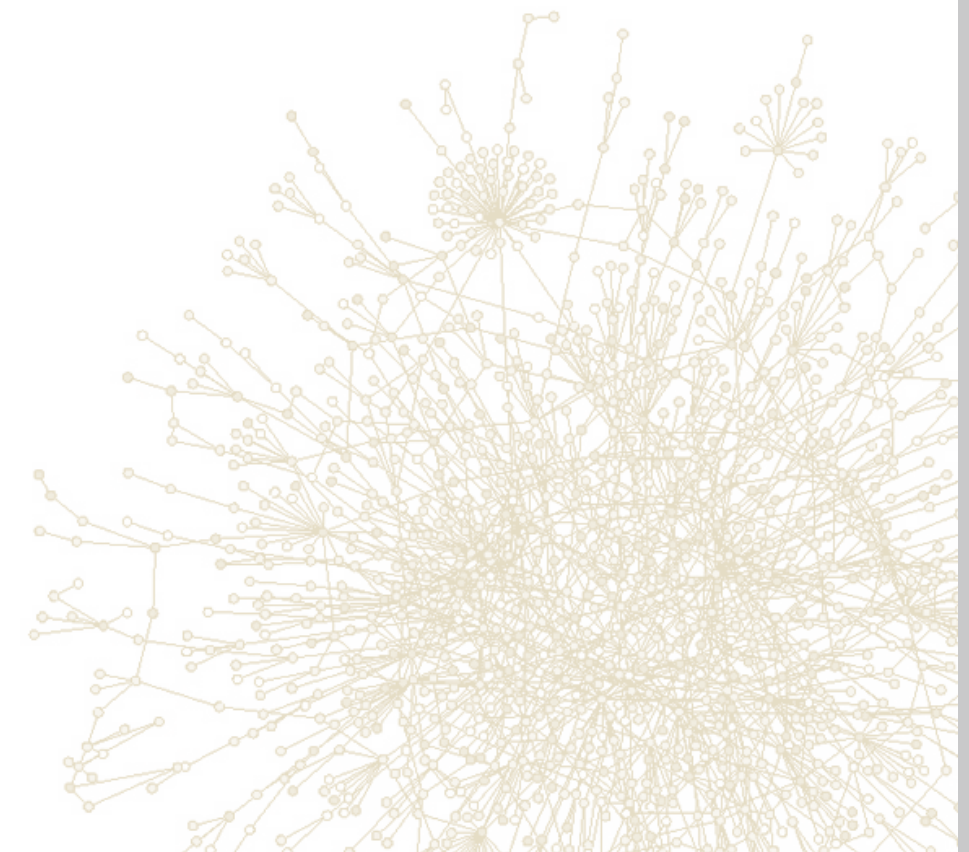
Microcantilever Nanomechanical Sensor for Biomolecule Analysis

Tae Song Kim
Center for BioMicrosystems
• tskim@kist.re.kr

Introduction

All objects in fixed motion have their own resonance properties determined by their geometric and ma-terial characteristics. In physics, resonance is the disposition of a structure to oscillate at a greater amplitude at certain frequencies, called the structure's resonant frequencies. At a resonant frequency, even small external sources of vibration can produce very large differences in the amplitude of the oscillation of the structures as they use up stored energy. The phenomenon of resonance finds application in magnetic resonance imaging (MRI) and in spectroscopy using nuclear magnetic resonance (NMR), as well as in sound systems and in frequency filters in electronic devices.

Recently, there has been growing interest in sensor systems research using a change in the resonant frequency of micro/nano-sensors, because micro/nano-sensors are able to detect and analyze targets at a molecular level. One of the popular micro/nano-sensors, a microcantilever, is a typical micro/nano electromechanical system (MEMS/NEMS) sensor platform that has a diving-board-shaped structure. When specific molecules are bound onto the recognition layer of a coated microcantilever, the resonant fre-quency of the microcantilever changes to a lower frequency range, since the resonant frequency of the microcantilever is related to its mass and stiffness. The shift in resonant frequency of the microcantilever allows not only the quantification of specific biomolecules, but also enables the analysis of the behavior of small molecules in a variety of environments. Eventually, we anticipate that the microcantilever sensor will lead to the development of innovative and highly sensitive systems for analyzing biomolecules, with applications in disease diagnostics and/or in monitoring the mecha-nical properties of nano-materials.

Research motivation

Technology for the detection of biological molecules based on numerous BioMEMS/NEMS devices has been used in a variety of applications, including re-cognition of biomaterials such as disease-related DNA sequences, specific proteins, and enzymes with several functions [1]. As shown in Figure 1, the general structure of a biomole-cules detection system consists of a transducer element, a biological recognition element (functionalized receptor layer), a biological analytes reaction system, etc. When the specific biomolecule is introduced into the biological analytes reaction system, those specific analytes interact with receptor molecules, and as a result a change in me-chanical, electrical, or optical signals is generated by the transducer.
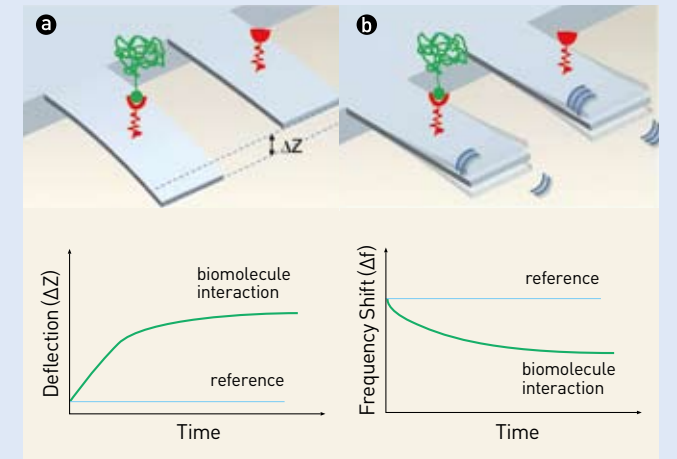
An increasing number of MEMS devices for biological and biomedical applications have been developed in recent years. These devices differ significantly in their designs and fabrication techniques and also in the areas of their application. BioMEMS devices are used to detect cells, tissues, microorganisms, viruses, proteins, DNA and small molecules of biochemical importance and interest. In general, the use of micro-and nano-scale detection technologies conveys advantages such as (i) providing higher sensitivity by detecting small changes in signals, (ii) reducing the reaction volumes and associated costs, (iii) reducing the time to get results due to smaller volumes resulting in higher effective concentrations, and (iv) facili-tating the miniaturization and portability of the whole system.
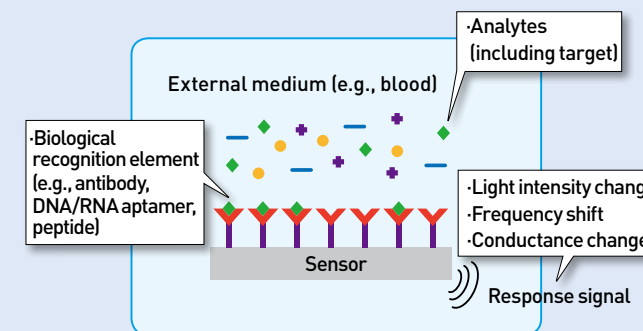
FIGURE 1 General biological molecules detection system

Microcantilever sensor

Mechanical detection of biomolecules such as cells, proteins, DNA, and small molecules has recently been achieved through the use of micro- and nanomechanical cantilever sensors [2]. There are two modes, static and dynamic, for the detection of biomolecules. In static mode, the biochemical reaction is performed on one functionalized side (the top) of the cantilever. When the biochemical-specific interaction occurs on the cantilever surface, a deflection of the cantilever is caused by a change in surface free energy and the resulting change in surface stress. We can measure the bending of the cantilever through several detection methods. In dynamic mode, the cantilever is excited mechanically so that it vibrates at its specific resonant frequency by a variety actuating methods such as an external drive, thermal vibration, ambient noise, or an embedded actuating layer. The resonant frequency of a recognition-layer-bearing cantilever is compared to the resonant frequency of the cantilever once a biological entity is captured. The change in mass and stiffness can be detected by sensing the resonant frequency shift resulting from biological-specific binding between receptors and ligands. A summary of the achievements of micro/nanocantilever biosensors is given in Table 1.

FIGURE 2 Scheme of the microcantilever-based biomolecule detection. The biomolecular interactions are revealed through (a) static deflection and (b) change in resonant frequency of cantilever sensors.

TABLE 1 Examples of cantilever-based biomolecule detection [2]

Research group	Device figure	Detection mode	Analyte	Detection limit
IBM Zurich Research Laboratory		Static	DNA	10 nM
North–western University		Static	Biotin	100 fg/ml
Oakridge National Laboratory		Static	SNP	–
UC Berkeley		Static	PSA	0.2 ng/ml
MIT		Dynamic	Goat anti–mouse IgG	0.7 nM
Cornell		Dynamic	dsDNA	1.65 ag
KIST		Dynamic	PSA	10 pg/ml
Purdue University		Dynamic	Vaccinia virus particle	1011 pfu/ml

Fabrication of piezoelectric layer-embedded microcantilevers

We fabricated microcantilevers by the micromachining process. We have previously reported the details of micro-

cantilever fabrication in [3,4]. Microfabricated cantilevers are composed of a Ta/Pt/PZT/Pt/SiO$_2$ layer on a SiN$_x$ supporting layer for simultaneous self-actuating and sensing. Their thickness, resonant frequencies, and Q-factor are about 1.98μm, 10~200KHz, and over 135, respectively. Figure 3 shows a microfabricated cantilever sensor and the process for achieving target detection after fabrication.
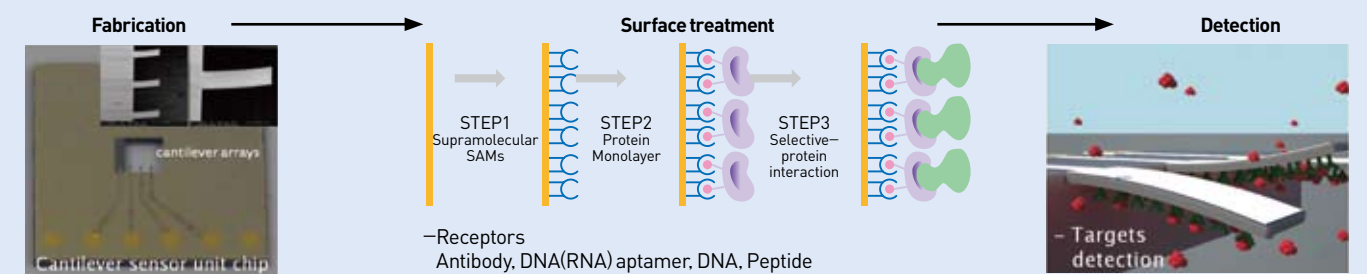
Microcantilever-based biomolecule detection

Prior to detecting biomolecules, the surface of the micro-fabricated cantilever is functionalized by adding biological recognition materials such as antibodies, aptamers, peptides and so on. These functionalized nanomechanical micro cantilevers detect several biomolecules based on changes in mechanical properties (i.e., resonant frequency) generated by receptor-ligand specific binding.

The magnitude of resonant frequency changes increases inversely with the size of the cantilever, resulting in an increase in minimum detectable sensitivity as the cantilever is made smaller. Limit of detection (LOD) was up to 1ng/mℓ in detecting four different proteins--prostate specific antigen (PSA), C-reactive protein (CRP), creatin kinase MB freaction (CK-MB) and hepatitis C virus (HCV) helicase. Moreover, we demonstrated the feasibility of microcantilever-based DNA detection [3, 5, 6, 7].

Analysis of microcantilever-based biopolymers in the presence of environmental changes
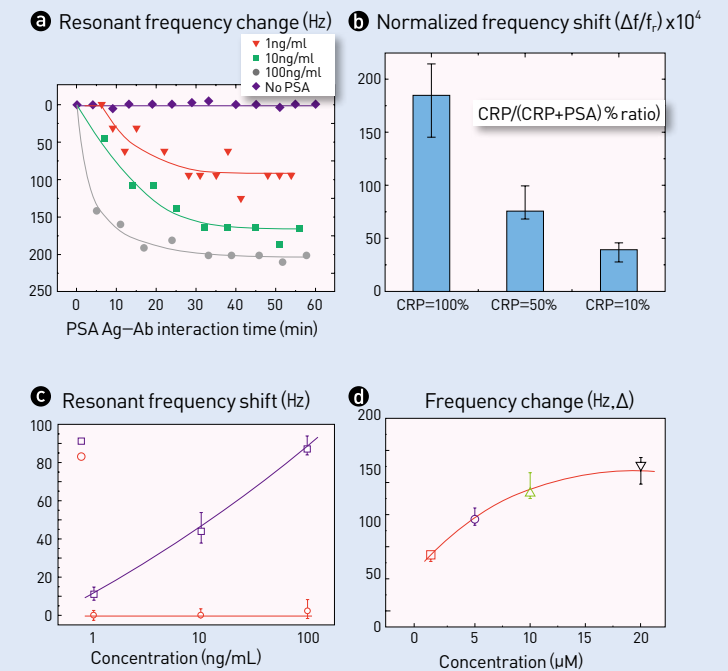
In order to study the ability of the cantilever response to indicate the behaviors of cancer marker proteins, we first focused on the behaviors of a free PSA system in regards to temperature. The temperature-sensitive protein activity of both the monoclonal antibody receptor for PSA (MAbs receptor) and the free PSA–MAbs receptor complex is

Fabrication　Surface treatment　Detection

STEP1 Supramolecular SAMs　STEP2 Protein Monolayer　STEP3 Selective–protein interaction

–Receptors
　Antibody, DNA(RNA) aptamer, DNA, Peptide

–Targets detection

**FIGURE 3** Scheme of microcantilever-based biomolecule detection

shown in Figure 5. The frequency shifted with a slope of only +5Hz per degree, due to the possible mismatch of the thermal expansion coefficients found in a multilayered cantilever. However, the frequency shift of the PSA MAbs-immobilized cantilever (line 2 in Figure 5c) revealed the presence of a transition near 35℃, indicating the possibility of deterioration in protein activity as a result of thermal denaturation. At an elevated temperature, the frequency decreased with a slope of –11.5Hz per degree, reached its maximum frequency shift value near 35℃, and then reversed to a slope of +48.7Hz per degree when approaching the protein-absent status value.

We investigated the humidity-sensitive protein activity of the MAbs receptor and the PSA–MAbs receptor complexes. We measured the water vapor sorption isotherm curve at 35℃ by controlling the relative humidity from 30% to 90% using deionized water. The water vapor sorption isotherm curve of the MAbs receptor-immobilized cantilever (line 2 in Figure 5c), reveals a decrease of the frequency and has a sigmoidal function. Notably, the sigmoidal curve of the water vapor sorption isotherm measured from the PSA–MAbs receptor complex (line 3 in Figure 5c) shows that the sensor response is larger than the one measured from the MAbs receptor, especially in the high humidity region, → 70%. We were able to observe the loss of stable conformations and/or the lack of activity when the proteins were exposed to the low humidity condition, indicating that the protein conformation is easily changed with respect

ⓐ Resonant frequency change (Hz)　**ⓑ** Normalized frequency shift ($\Delta f/f_r$) x10^4

CRP/(CRP+PSA) % ratio

PSA Ag–Ab interaction time (min)

CRP=100%　CRP=50%　CRP=10%

ⓒ Resonant frequency shift (Hz)　**ⓓ** Frequency change (Hz, Δ)
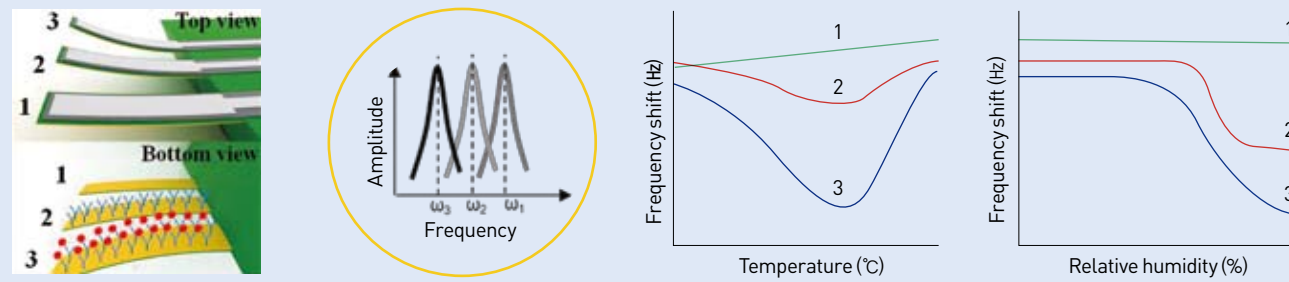
Concentration (ng/mL)　Concentration (μM)

FIGURE 4 Microcantilever-based detection result of (a) prostate specific antigen (PSA), (b) C-reactive protein (CRP), (c) creatin kinase MB fraction (CK-MB), and (d) hepatitis B virus-related DNA

to the hydration state. This is because water molecules are fun damental in protein folding mainly because of their role in defining hydrophobic attractions and their ability to activate ionic interactions between acidic and basic residues. The observed water vapor isotherms, in terms of the frequency shift, were consistent with the water vapor sorption isotherms that are reported for peptides, proteins, and structurally related materials, in
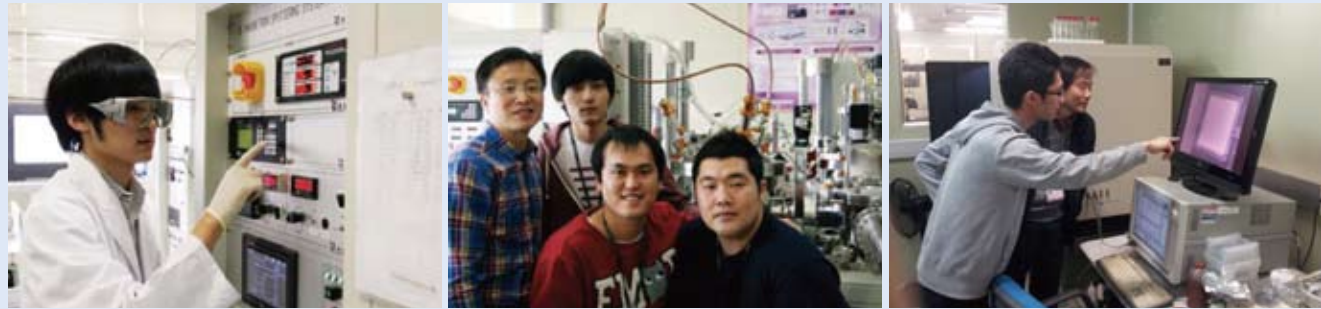
ⓐ **Protein dynamics via cantilever response**

Direct conversion of
biomolecular interaction to electric signal

ⓑ

Reversible process (1)
Irreversible process (2,3)

Ag–Ab interaction force

Temperature (°C)

ⓒ

Reversible process (1)
Irreversible process (2,3)

Ag–Ab interaction force

Relative humidity (RH %)
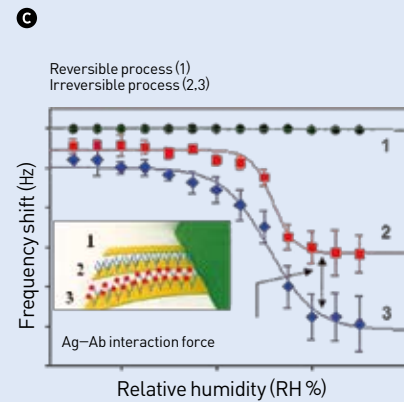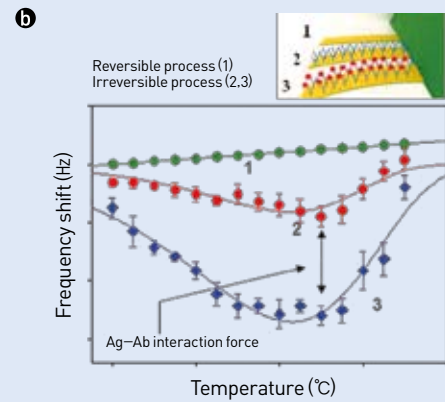
FIGURE 5 The cantilever systems relying on resonant frequency shifts enable the transduction of protein behaviors directly to an electrical signal. (a) Schematic showing that the change of protein dynamics can produce resonant frequency shift. (b) The temperature-sensitive protein activity of the MAbs receptor and PSA-receptor complex. (c) The humidity-sensitive protein activity of the MAbs receptor and PSA-receptor complex.

References

[1] Craighead H. Nature. 2006; 442: 387-393.

[2] Hwang KS, Lee S-M, Kim SK, Lee JH, Kim TS. Ann Rev Anal Chem. 2009; 2: 77-98.

[3] Hwang KS, Lee JH, Park J, Yoon DS, Park JH, Kim TS. Lab Chip. 2005; 4: 547-552.

[4] Lee JH, Yoon KH, Hwang KS, Park J, Ahn S, Kim TS. Biosens Bioelectron. 2004; 20: 269-275.

[5] Lee JH, Kim TS, Yoon KH. Appl Phys Lett. 2004; 84: 3187-3189.

[6] Hwang KS, Eom K, Lee JH, Chun DW, Cha BH, Yoon DS, Kim TS, Park JH. Appl Phys Lett. 2006; 89: 173905.

[7] Hwang KS, Lee S-M, Eom K, Lee JH, Lee YS, Yoon DS, Park JH, Kim TS. Biosens Bioelectron. 2007; 23: 459-465.

[8] Lee JH, Hwang KS, Yoon DS, Kang JY, Kim SK, Kim TS. Adv Mater. 2011; 23: 2920-2923.

terms of their water sorption on a dry solid (g water per g dry solid). Interestingly, the change of degree in protein hydration in the case of the PSA–MAbs receptor complex (line 3 in Figure 5c) is larger than that of the MAbs receptor (line 2 in Figure 5c), indicating that the water molecules generate not only the formation of a hydration layer by water sorption on the PSA–MAbs receptor complex, but also the generation of interaction forces in the PSA–MAbs receptor complex.

Daurinol as a Potent Anticancer Compound with Low Side Effects Derived from a Mongolian Medicinal Plant

Chu Won Nho
Functional Food Center,
Gangneung Branch
• cwnho@kist.re.kr

Kyungsu Kang

Introduction

Cancer is still one of the most life-threatening diseases and many drugs have been developed for treating various types of cancers. Unfortunately, while anticancer drugs can be very effective at killing cancer cells, they can also trigger side effects and cytotoxicity in normal cells. To avoid these harsh effects, anticancer compounds derived from medicinal plants have been considered good candidates for drug development since they have been consumed by humans for many years as part of traditional medicine . Our KIST research team has been studying many Mongolian medicinal plants which show promise in stopping the growth of cancer cells in colon, breast, stomach, and liver cancer models. This article focuses on the anticancer effects of a compound isolated from a Mongolian medicinal plant, *Haplophyllum dauricum,* which has been used as a traditional medicine in Mongolia and Russia [1,2]. The

compound, daurinol (Figure 1a), is shown to be a promising anticancer compound for development as an anticancer drug with low side effects compared to the existing clinical anticancer agent, etoposide (Figure 1a).

## Anticancer Effects of Daurinol

Our research demonstrated that daurinol displayed a potent antiproliferative effect on various human cancer cells with IC_{50} values (a concentration that inhibits 50% of cell proliferation) below 20 µM after 48 hours of treatment (Figure 1b). Daurinol demonstrated the greatest antiproliferative activity in human colorectal cancer HCT116 cells, with IC_{50} values of 23.19 ± 0.67 at 24 hours and 2.03 ± 0.18 µMat 48 hours treatment (Figure 1b). Therefore, we chose HCT116 cells as a model cell line in which to investigate the molecular mechanism of the antiproliferative effect of daurinol.

We then hypothesized that the antiproliferative activity of daurinol was due to inhibition of DNA synthesis. To test this, we measured cell viability and DNA synthesis after treatment with daurinol using CCK-8 and BrdU incorporation assays. Daurinol significantly inhibited cell viability (mitochondrial dehydrogenase activity) and BrdU incorporation (DNA synthesis) in HCT116 cells at all concentrations tested (1.25-20 µM). Etoposide was a more potent inhibitor of DNA synthesis (BrdU incorporation) than cell viability (mitochondrial dehydrogenase activity) (Figure 1c). To confirm whether the decrease in BrdU incorporation by daurinol was due to blocking DNA synthesis rather than decreasing cell viability by other cytotoxic effects, we performed an additional experiment in which we measured cell viability and BrdU incorporation at the same time in HCT116 cells at different levels of confluence after treatment with 5 µM daurinol or 10 µM etoposide, and plotted cell viability vs. BrdU incorporation. We then estimated the inhibition of DNA synthesis based on the distribution of the data. Both daurinol and etoposide displayed reduced BrdU incorporation rather than reduced cell viability as compared to the vehicle control. The relative DNA synthesis indices (the percentage of BrdU incorporation by cell viability) of daurinol and etoposide were significantly lower than that of the vehicle control at both 24 and 48 hours of treatment (Figure 1d).

Next, we investigated the effect of daurinol on the cell cycle progression of HCT116 cells using flow cytometric DNA content analysis. Daurinol (5 µM) induced S-phase arrest at 24, 48, and 72 hours of treatment (Figure 2a) in a dose-dependent manner (Figure 2b). We confirmed daurinol-induced S-phase arrest under G1/S synchronized conditions via hydro-xyurea synchronization (Figure 2c) and under G0/G1 synchronization conditions via serum starvation (data not shown).Because DNA replication occurs during the S-phase, we assumed that daurinol-induced S-phase arrest was due to the abrogation of DNA
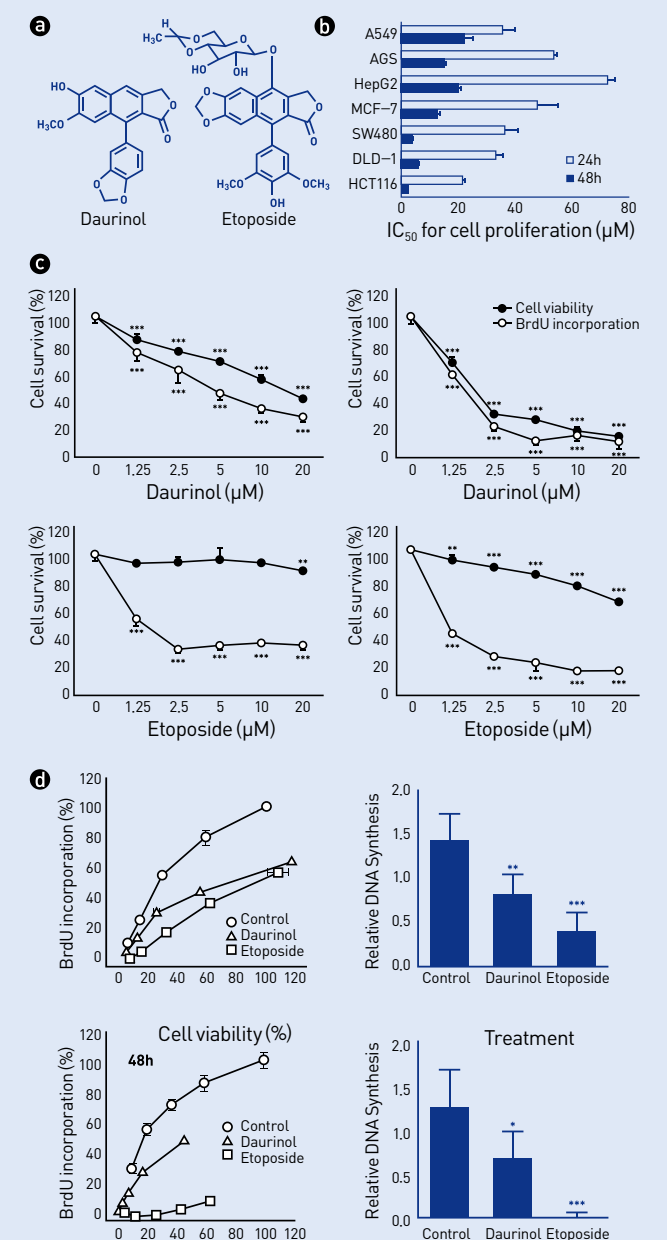
FIGURE 1 Daurinol inhibits cell proliferation and DNA synthesis. (a) Chemical structures of daurinol and etoposide. (b) Antiproliferative activity of daurinol was determined by cell viability assays in various human cancer cell lines. (c) Inhibition of cell viability and DNA synthesis by treatment with daurinol or etoposide for 24 and 48 hours was determined by CCK-8 assay (mitochondrial dehydrogenase activity) and BrdU incorporation ELISA in HCT116 cells. (d) Cell viability vs. BrdU incorporation (left). Relative DNA synthesis was calculated by BrdU incorporation (%) over cell viability (%) (right).
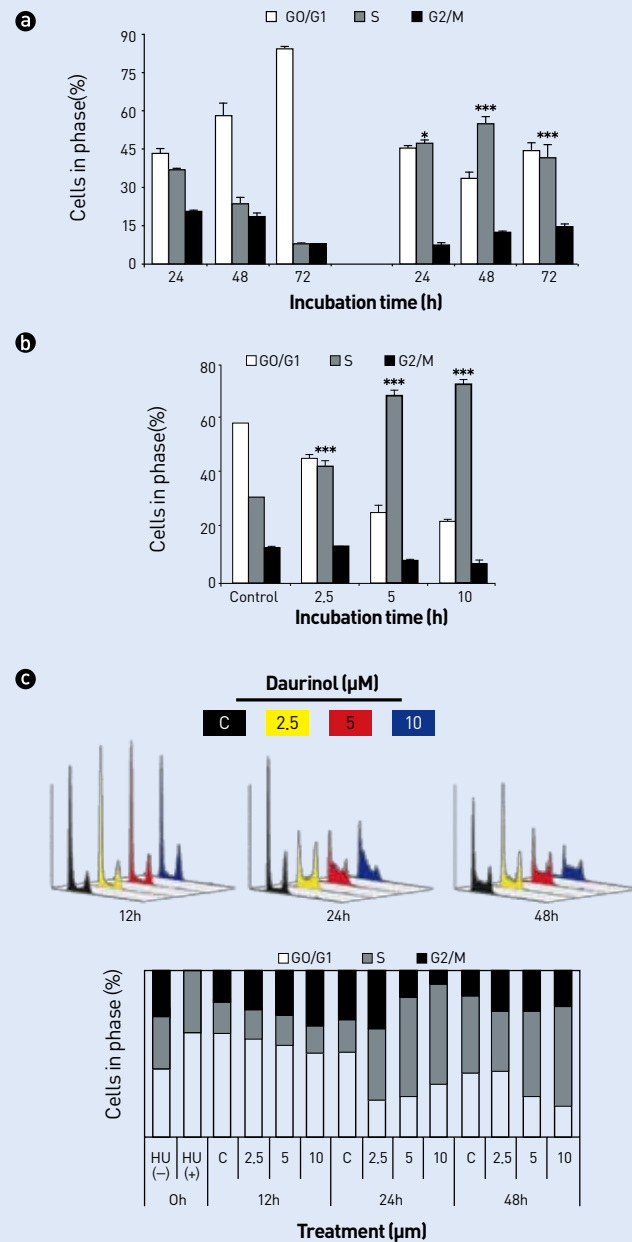
FIGURE 2 Daurinol induces S-phase arrest in HCT116 cells. Cell cycle distribution was evaluated by using flow cytometric DNA content analysis. (a) HCT116 cells were treated with 5 µM daurinol for 24, 48, and 72 hours. (b) HCT116 cells were treated with various concentrations of daurinol (0, 2.5, 5, 10 µM) for 48 hours. (c) Daurinol-induced S-phase arrest of HCT116 cells was confirmed in hydroxyurea-synchronized cells. Cells were pre-treated with 2 mM hydroxyurea (HU) for 12 hours to synchronize in G1/S phase. Then, cells were treated with daurinol (0, 2.5, 5, 10 µM) for 12, 24, and 48 hours. C, Vehicle control.

replication by the inhibitory activity of daurinol. Etoposide is known to be a potent agent for the induction of G2/M phase arrest in various cancer cells [3-6]. This difference in phases of cell cycle blockage was the first noticeable distinction between daurinol and etoposide, though both are inhibitors of DNA synthesis.
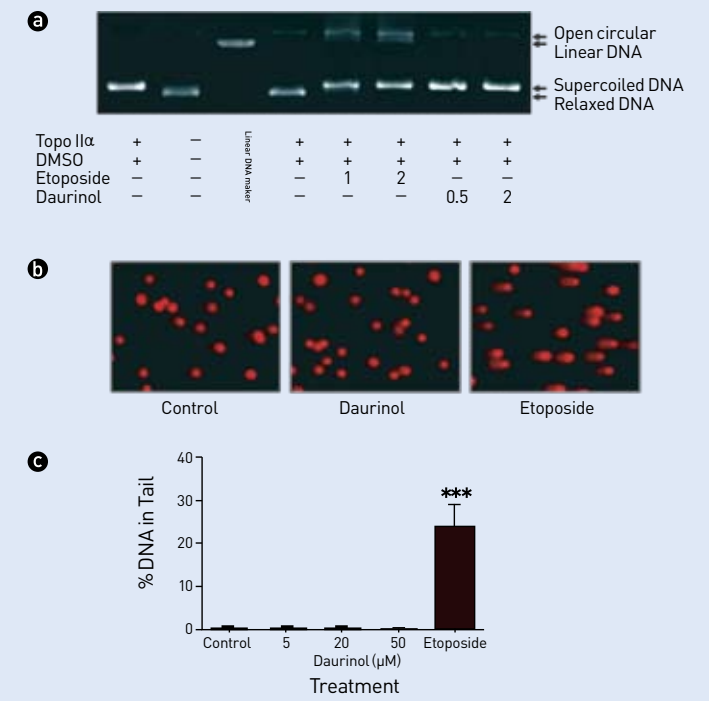
Inhibition of Topoisomerase IIα by Daurinol

Etoposide is a well-known topoisomerase poison, and it stabilizes the DNA cleavable complex [7]. Both etoposide and daurinol inhibited human topoisomerase IIα, preventing unwinding of the supercoiled DNA substrate (Figure 3a). As previously reported [7], etoposide induced the formation of open circular and linear DNA, which originated from the topoisomerase-DNA cleavable intermediate, but daurinol did not give rise to any open circular or linear DNA (Figure 3a).

We also measured DNA damage after treatment with daurinol or etoposide in HCT116 cells using comet assays. Etoposide (10 µM) clearly induced the formation of comet tails, indicating that etoposide significantly induces DNA damage (% DNA in tail). In contrast, even 50 µM daurinol did not induce the formation of DNA comet tails (Figure 3b, c). Because the formation of comet tails implies severe DNA damage in cells, we concluded that DNA damage induced by etoposide treatment is much greater than that of daurinol. The formation of comet tails occurs when the DNA cleavable complex is formed in cells, which is an important property of topoisomerase poisons [8]. Therefore, we concluded that daurinol must be a catalytic inhibitor of human topoisomerase IIα rather than a topoisomerase poison because treatment with daurinol induces less DNA damage compared to the etoposide treatment. This was the second key distinction between daurinol and etoposide.

No Abnormal Nuclear Enlargement Induced by Daurinol

We also measured nuclear size after treatment with daurinol using fluorescent microscopy and fluorescence pulse width analysis. Microscopic fluorescence observation and quantification of nuclear size using the circle measurement algorithm of the microscope software revealed that daurinol did not trigger nuclear enlargement compared to the vehicle control. Nuclear sizes in daurinol-treated cells were similar to vehicle control cells, while those of etoposide-treated cells were significantly larger (Figure 4a-c). Flow cytometric pulse width analysis also demonstrated that daurinol treatment did not induce a significant enlargement of cells or nuclei, as opposed to etoposide treatment. The FSC-H and FL2-W values (which refer to cell size and nuclear size, respectively) of the daurinol-treated cells had a similar distribution to vehicle-treated control cells, while etoposide-treated cells occupied much higher positions than controls (Figure 4d). The mean values of FSC-H were 418.8 ± 22.0 for the vehicle control, 411.8 ± 9.4 for 5 µM daurinol-, and 544.0 ± 11.8 for 10 µM etoposide-treated cells at 48 hours. The mean values of FL2-W were 207.1 ± 0.5 for the vehicle control, 203.2 ± 0.8 for 5 µM daurinol, and 322.6 ± 3.1 for 10 µM etoposide treatments. We also compared distributions on histogram plots using Kolmogorov–Smirnov statistics, which estimate the differential distribution of two histogram plots. The D/s(n) (the index of similarity) values of the daurinol-treated cells (2.5, 5, 10 µM for 48 hours) compared to vehicle control cells were significantly lower than those of etoposide-treated cells (10 µM for 48 hours) (Figure 4e). This difference between the effects of daurinol and etoposide may be the most important for chemotherapeutic applications. We hypothesized that the side effects of etoposide might originate from the abnormal nuclear enlargement that is caused by severe DNA damage and G2/M arrest. Therefore, we hypothesized that daurinol


FIGURE 3 Daurinol is a catalytic inhibitor of human topoisomerase IIα. (a) Inhibitory activity of daurinol and etoposide on human topoisomerase IIα was evaluated by in vitro biochemical assays. The supercoiled DNA (pHOT1) substrate was incubated with human topoisomerase IIα in the presence of daurinol (1, 2 mM) or etoposide (0.5, 2 mM). DNA relaxation was evaluated by 1% agarose gel electrophoresis in the presence of ethidium bromide. (b and c) Effects of daurinol and etoposide on DNA damage were determined by comet assays. HCT116 cells were treated with daurinol (5, 20, 50 µM) or 10 µM etoposide for 6 hours. (b) Images of cellular DNA damage were detected by fluorescence microscopy. Pictures are representative of three independent experiments. (c) The DNA damage index (% DNA in tail) was determined using comet score software.

would have fewer adverse side effects because it does not induce significant nuclear enlargement, as it can induce S-phase arrest without causing severe DNA damage.

Anticancer Effects of Daurinol in Nude Mice Xenograft

To test our hypothesis about the severity of daurinol side effects in vivo, we investigated the antitumor effects and side effects of daurinol and etoposide treatment in mice. Two independent in vivo experiments were performed
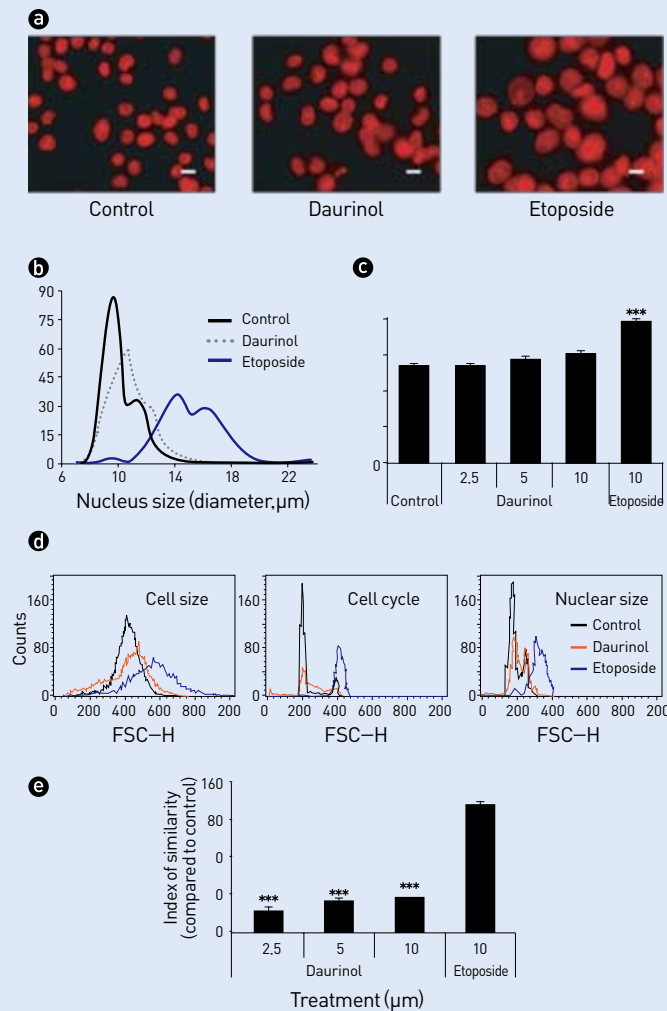
FIGURE 4 Effects of daurinol and etoposide on the nucleus size of HCT116 cells were evaluated by fluorescence microscopy (a-c) and flow cytometry (d and e). HCT116 cells were treated with daurinol (2.5, 5, and 10 μM) or 10 μM etoposide for 48 hours. Cellular DNA was labeled with propidium iodide for visualization and flow cytometric DNA content analysis. (a) Microscopic fluorescence images of HCT116 cells treated with 5 μM daurinol or 10 μM etoposide for 48 hours. (b) Distribution of nucleus size of HCT116 cells treated with 5 μM daurinol or 10 μM etoposide for 48 hours. (c) Mean value of nucleus diameter. (d) Flow cytometric analysis of HCT116 cells treated with 5 μM daurinol or 10 μM etoposide. The FSC-H, FL2-A, and FL2-W histogram plots represent cell size, cell cycle, and nucleus size, respectively. Histograms are representative of quadruplicate experiments. (e) Differences in the distributions of the FL2-W value (nucleus size) between vehicle control and chemical-treated cells were quantitatively determined using Kolmogorov-Smirnov statistics. Index of similarity is the D/s(n) value of Kolmogorov-Smirnov statistics.

using a nude mice xenograft model. The first experiment was performed to evaluate antitumor activity and toxicity, and their persistence following daurinol and etoposide treatments. Daurinol (1, 5, 10, 20 mg/kg) or etoposide (20 mg/kg) were administered three times weekly for two weeks, and mice were maintained for an additional two weeks before sacrificing. Both etoposide (1-20 mg/kg) and daurinol (20 mg/kg) displayed potent antitumor activities, as the tumor volumes of all treatment groups were significantly lower than those of the vehicle-treated group (Figure 5b, d). Tumor weights of mice treated with daurinol (5, 20 mg/kg) or etoposide had also significantly decreased (5, 20 mg/kg) or etoposide had also significantly decreased compared to the vehicle-treated group (Figure 5c). Importantly, the body weights of mice treated with daurinol were similar to those of vehicle-treated mice, whereas the weights of mice treated with etoposide had significantly decreased (Figure 5a).

A second round of *in vivo* experiments was performed to confirm antitumor activity and toxicity and to investigate changes in hematological parameters and protein expression. In these experiments, mice were treated with daurinol (5, 10, 20 mg/kg) or etoposide (20 mg/kg) twice weekly for three weeks. We again found significant antitumor activity of daurinol and etoposide (Figure 6b, c), and the body weights of mice treated with etoposide had slightly decreased compared to those of daurinol-treated and vehicle-treated mice (Figure 6a). The inhibition of DNA synthesis by daurinol and etoposide was also determined using BrdU immu-nohistochemical analysis. BrdU incorporation in mice treated with daurinol (5, 20 mg/kg) or etoposide (20 mg/kg) significantly decreased compared to vehicle-treated mice (Figure 6d), this result being consistent with our *in vitro* studies. Western blot analysis using total cell lysates prepared from xenograft tumors demonstrated activation of the ATM/Chk/Cdc25A pathway, although only the phosphorylation of Chk1 at Ser345 was significantly different (Figure 6e). No significant damage of
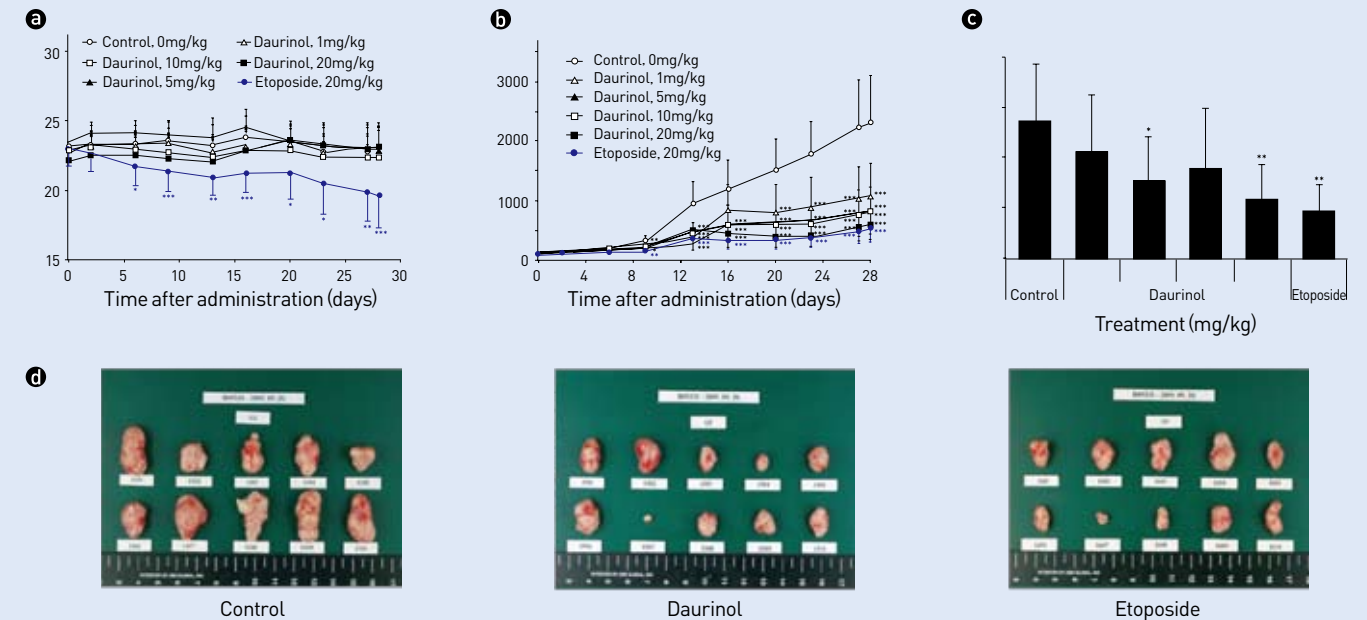
FIGURE 5 Antitumor activity of daurinol and etoposide in nude mice xenograft models of HCT116 cells. Daurinol (1, 5, 10, 20 mg/kg) or etoposide (20 mg/kg) were administered intraperitoneally three times weekly for two weeks. Body weights (a) and tumor volumes (b) were monitored for four weeks after the initial injection of chemicals to evaluate toxicity, antitumor effects, and their persistence of daurinol and etoposide treatment. (c) On day 29, tumors were removed and weighed. Data are expressed as mean ± SD (n = 10).*P< .05 and **P< .01, for significant differences from the vehicle-treated group. (d) Photographs of tumors removed from mice treated with vehicle control, daurinol (20 mg/kg), or etoposide (20 mg/kg).

normal organ tissues, including the liver, kidney, or colon, was observed in either the daurinol- or etoposide-treated mice (data not shown).

Anticancer Effects of Daurinol without Hematological Toxicity

We investigated hematological parameters in nude mice treated with daurinol or etoposide to evaluate the hematological toxicities of the tested chemicals. White blood cell counts (WBCs) of mice treated with etoposide (20 mg/kg) were significantly lower than those of vehicle-treated mice, while the WBCs of mice treated with daurinol (5, 10, 20 mg/kg) were comparable to vehicle-treated mice. Similarly, red blood cell counts (RBCs) and hemoglobin contents of mice treated with etoposide (20 mg/kg) were significantly lower than those of vehicle-treated

and daurinol-treated mice. Hematocrits (%) displayed similar patterns to the results of WBCs, RBCs, and hemoglobin. Etoposide treatment significantly decreased the hematocrit (%) compared to the vehicle-treated group, while daurinol treatment did not, except at the 10 mg/kg dose. The number of platelets between vehicle-treated and daurinol-treated mice was comparable, except in the 5 mg/kg daurinol treatment group. The platelet counts of mice treated with etoposide (20 mg/kg) increased slightly compared to the vehicle-treated group (Table 1).

Summary

In light of our research results, we propose that daurinol is a promising lead compound for the development of a novel anticancer agent that is similar to etoposide but has reduced side effects, including hematological toxicity
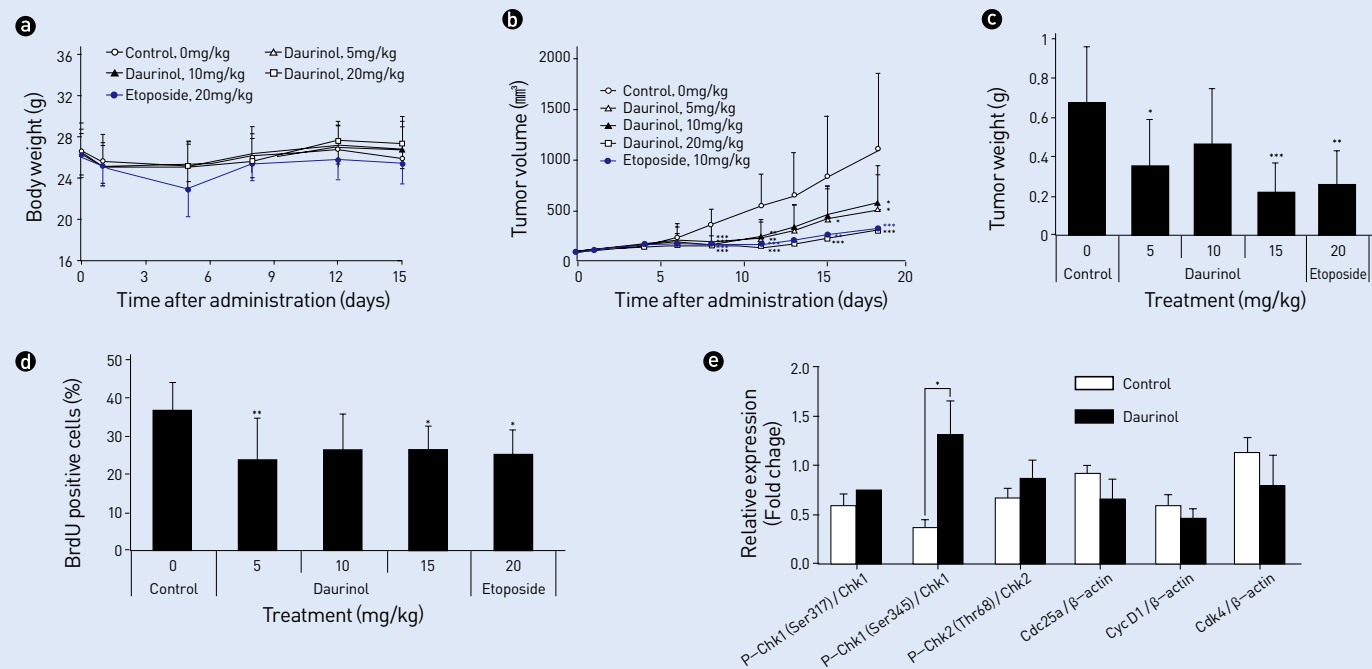
FIGURE 6 Evaluation of antitumor activities and molecular effects of daurinol and etoposide in nude mice xenograft models. Daurinol (5, 10, 20 mg/kg) or etoposide (20 mg/kg) were administered intraperitoneally twice weekly for three weeks. Body weights (a) and tumor volumes (b) were monitored for three weeks. On day 18, tumors were removed for immunohistochemistry and western blot analysis. (c) Tumor weights. (d) Inhibition of DNA synthesis in xenograft tumors was measured by BrdU incorporation immunostaining. Data are expressed as mean ± SD (n = 10). *P⟨ .05 and **P⟨ .01, for significant differences from the vehicle-treated group. (e) Western blot analysis of expression and phosphorylation of cell cycle regulatory proteins from tumors of nude mice treated with the vehicle control or daurinol (20 mg/kg). Columns and error bars indicate mean ± SEM (n = 5). *P⟨ .05 for significant differences from the vehicle-treated group.

TABLE 1 Effect of daurinol and etoposide on the hematological parameters in nude mice bearing HCT116 cell xenograft tumors

|	Control 0 mg/kg	Daurinol			Etoposide 20 mg/kg
		5 mg/kg	10 mg/kg	20 mg/kg	
WBCS (x103 cells/µl)	4.07 ± 2.42	2.60 ± 1.12	1.86 ± 0.74	1.63 ± 0.91	0.92 ± 0.43*
RBCS (x103 cells/µl)	9.66 ± 0.41	9.55 ± 0.37	8.82 ± 1.20	9.24 ± 1.03	7.74 ± 0.49*
Hemoglobin (g/dl)	15.59 ± 0.61	15.33 ± 0.68	14.27 ± 1.98	14.78 ± 1.60	12.31 ± 0.76*
Hematocrit (%)	48.61 ± 2.48	47.29 ± 2.09	43.48 ± 6.38+	45.44 ± 5.34	37.36 ± 2.92*
Platelets (x103 cells/µl)	1418 ± 145	916 ± 457+	1220 ± 462	1091 ± 470	1733 ± 263

(Figure 7). Therefore, strategies are needed to synthesize or derive daurinol and to optimize its antitumor efficacy, toxicity, solubility, and pharmacokinetics.

In summary, we have shown that daurinol, a novel plant arylnaphthalene lignan, is a potential anticancer agent that causes less hematological damage than the related clinical agent etoposide. However, further studies of the molecular mechanisms of the anticancer effects of daurinol, including upstream signaling and its mode of inhibition against human topoisomerases, as well as pre-clinical and clinical trials of daurinol, are needed.

FIGURE 7 Anticancer effects of dauriniol compared to etoposide

		Daurinol	Etoposide
In vitro	Inhibition of topoisomerase IIα	Catalytic inhibitor	Topoisomerase poison
	Cell cycle arrest	S phase arrest	G2/M phase arrest
	DNA damage	None	Severe
	Nuclear enlargement	Mild	Severe
	Cell and nuclear shape	●	●
In vivo	Loss of body weights	No change	Decrease
	Loss of WBCs	Mild	Severe side effect
	Loss of RBCs, Homoglobins	Mild	Severe side effect
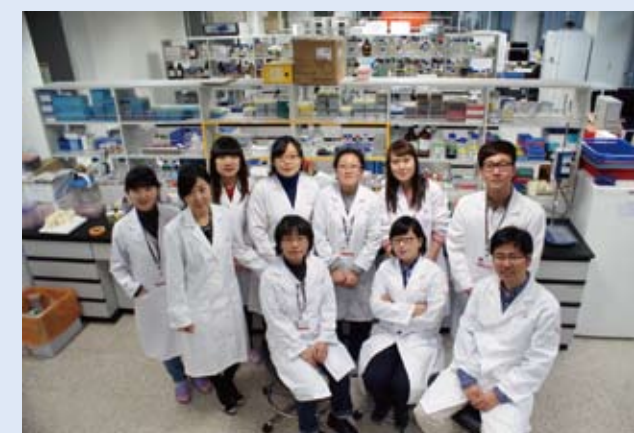
Note

References

[1] Batsuren D, Batirov EK, Malikov VM, Zemlyanskii VN, Yagudaev MR. Chem Nat Compd. 1981; 17: 223-225.

[2] Graham JG, Quinn ML, Fabricant DS, Farnsworth NR. J Ethno-pharmacol. 2000; 73: 347-377.

[3] Hande KR. Eur J Cancer. 1998; 34: 1514-1521.

[4] Larsen AK, Escargueil AE, Skladanowski A. Pharmacol Ther. 2003; 99: 167-181.

[5] Kang K, Lee SB, Yoo JH, Nho CW. Biotechnol Lett. 2010; 32: 1045-1052.

[6] Smith PJ, Soues S, Gottlieb T, Falk SJ, Watson JV, Osborne RJ, Bleehen NM. Br J Cancer. 1994; 70: 914-921.

[7] Boos G, Stopper H. Toxicol Lett. 2000; 116: 7-16.

[8] Gong Y, Firestone GL, Bjeldanes LF. Mol Pharmacol. 2006; 69: 1320-1327.
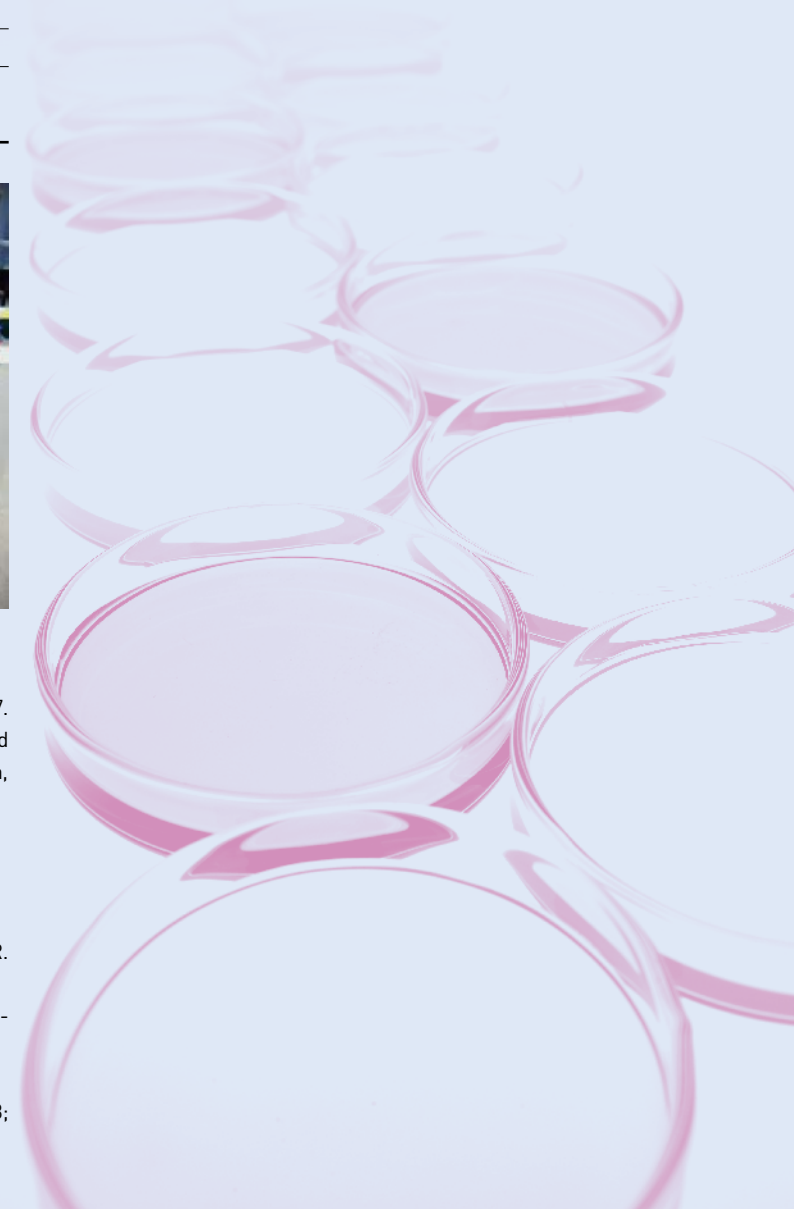
Development of Methods for the Early Diagnosis of Ankylosing Spondylitis

Chang Hoon Nam

Yeon Joo Kim

Interdisciplinary Human
Biotechnology Group, KIST Europe
• chnaghoon.nam@gmail.com

FIGURE 1 Typical symptoms of Ankylosing Spondylitis include: (a) posture, changes, particularly a rounded back; (b) inflammation of the eye, uveitis, or iritis; (c) bony ankylosis; (d) damage to organs such as the heart, lungs or kidneys.
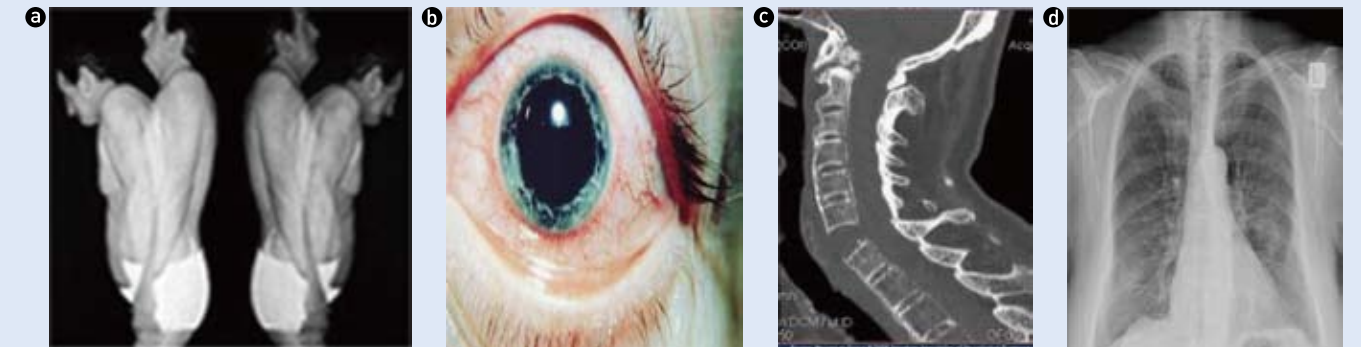
Introduction

Spondyloarthropathies (SpA) are a heterogeneous group of interrelated inflammatory diseases involving joint inflammation of the spine and areas affected by arthritis (axial and peripheral). These diseases share similar clinical, epidemiological, radiological and immunogenetic features. The diseases typically considered under the SpA umbrella include: ankylosing spondylitis (AS), Reiter syndrome (RS), reactive arthritis (ReA), psoriatic arthritis (PsA), IBD-associated SpA, and undifferentiated SpA (uSpA). This group of diseases is characterized by familial aggregation, absence of rheumatoid factor, and association with human leukocyte antigen (HLA)-B27 [1].

Ankylosing spondylitis (AS), a prototype of spondyloarthritis (SpA), is a chronic inflammatory arthritis that mainly affects the sacroiliac joints and the spine. Posture change, eye inflammation, bony ankylosis, and organ damage, often affecting the heart and lungs, are common features of AS (Figure 1). The worldwide prevalence of AS ranges from 0.3 up to 0.9% and it is known to be highly heritable with a 97% heritability rate in twins [2].

Early diagnosis of AS is very important because it can provide a window of opportunity for effective treatment and unnecessary interventions can be avoided. With the introduction of tumor necrosis factor inhibitor (TNF-α blocking agents) as a therapy in AS treatment, accurate and effective early diagnostic methods have become even more important. AS patients whose disease has been of short duration are more likely to respond to TNF-α blocking agents, which are effective anti-inflammatory biologics, than patients with longstanding disease duration [3]. However, there are still many challenges standing in the way of early diagnosis of AS.

There are various reasons for the long delays which can occur in diagnosing AS. First of all, radiographic changes, widely used as a diagnostic method, generally do not appear until comparatively late in the AS disease process. Additionally, the low specificity of the first symptom, low-back-pain, as well as the seeming inappropriateness of examining for AS in its early stages, further contributes to diagnostic delay [4]. So far, there is no single definitive method for the diagnosis of AS. The use of MRI is the most reliable diagnostic tool and is prescribed on the basis of symptoms. Laboratory test results, for example, erythrocyte sedimentation rate (ESR) or C-reactive protein level (CRP), should accompany the MRI studies [5, 6]. In order to develop a simple and effective diagnosis system to detect the early stages of AS, KIST Europe's Interdisciplinary Human Biotechnology Group has been conducting intensive research of immunoglobulin variable heavy chain gene usage analysis which is being conducted by using peripheral blood mononuclear cells (PBMCs) and quantitative polymerase chain reaction (Q-PCR).

Immunoglobulin production

Immunoglobulin variable heavy (IgVH) chains consist of variable (IgV) and constant (IgC) domains. During the process of B cell maturation and immunoglobulin (Ig) production, IgVs are produced by the rearrangement of V(D)J genes. Among the 40 functional variable region segments (V_H1-40), 25 diversity segments (D_H1-25) and 6 joining segments (J_H1-6), one of V_H, D_H and J_H are randomly chosen and produce the IgV domain. Subsequently, Ig production is completed with the connection of IgV fragments and constant (C) genes, including Cμ, Cδ, Cγ, Cα and Cϵ. Class switch recombination determines which type of C genes are combined with IgV fragments, and this process allows the formation of Ig isotypes ranging from IgM to IgD, IgG IgA and IgE. V(D)J recombination and class switch recombination is responsible for the immense diversity of antibodies during the development of B lymphocytes.

Usage analysis of immunoglobulin repertories

The main purpose for analysis of V, D and J segments'

TABLE 1 Immunoglobulin variable gene usage skewed in particular autoimmune diseases

Autoimmune	Methods	Sampling condition	VH skewed	Related isotype	References
SLE	Phage display library		VH5 over expressed	IgG	Roben (1996)
	Hybridoma	Splenocyte, blood follicular cell	VH4−21	IgM, IgG	Stevenson (1933)
MG		Thymus tissue	VH3	N/A	Sims (2001)
Celiac disease	Phagedisplay library	Peripheral blood, lymphocyte	VH4	IgA	Sblattero (2000)
RA	Human/Mouse heterohybridoma	Rheumatoid synovial tissue	VH4	IgM	Ermel (1997)
	Hybridoma	Rheumatoid synovial tissue	VH1 (9&16 AA long in CDR3)	IgM	Robbins (1990)
Sjogren's syndrome		Glandular rearrangements	VH CDR3 shortest		Dörner (2002)
Ankylosing Spondylitis	DNA/PCR results	Rearranged synovial membrane	VH5 overexpressed, VH4 underexpressed		Voswinkel (2001)

usage (hereafter referred to as VH usage) of the IgVH in autoimmune disease is to clarify whether specified gene families or genes involved in basic antibody production are different in AS patients as compared to healthy controls [7]. This analysis can reveal differences in the basic Ig V repertoire of patients with B cell and/or T cell-mediated autoimmune diseases compared to healthy controls, differences which could be derived from intrinsic abnormalities during the generation of Ig V genes or B cell development and function. Thus, the analysis of Ig V gene usage can offer new insights into the possible pathogenic role of B cells in autoimmune diseases. Several research studies have investigated the variable heavy chain gene (hereafter referred to as VH gene) usage in various autoimmune disease patients by using a variety of PCR-techniques such as phage display library and hybridomas (Table 1).

Diagnosis using Q-PCR

Q-PCR followed by classic PCR is the technique of choice to quantify a specific DNA region [8]. From fundamental molecular biology to biotechnology, Q-PCR is a widely used routine tool, and researchers have developed several analysis methods for Q-PCR which usually allow for the validation of small changes in target gene expression in a DNA sample in a fast, reliable and high-throughput manner [8]. The most important advantages to PCR-based diagnostics are in its high specificity and time saving aspects [9]. SYBR Green 1 fluorescence dye is the simplest and most commonly used detection method [8]. During PCR using SYBR, the quantities of newly synthesized products are monitored by the specific binding affinity of SYBR to the minor groove double-stranded DNA [8], and when the SYBR dye is included in the PCR reacting mixture, fluorescence increases proportionally to the produced double-stranded DNA [9]. To use the Q-PCR system for diagnostics development, proper quantification of PCR and the design of proper controls to quantify target gene expression are imperative [10, 11].

In the study described here, we chose the relative quantification method on account of the fact that reporting the relative change in gene expression is sufficient rather than determining the absolute copy number of transcripts. Primers for the human acidic ribosomal protein (HuPo) gene, a house-keeping gene, were used since the HuPo gene is known to be more reliable than the β-actin gene as

TABLE 2 Primers used for RT-PCR

Primer set	Complementary DNA				
	Forward primer (5'→3')				Reverse primer (5'→3')
PR1	HuVH2[ab†]	CAG ATC ACC TTG AAG GAG TCT GG	HUJH1−2* HUJH3* HUJH4−5* HUJH6* HUJH7°		TGA GGA GAC GGT GAC CAG GGT GCC TGA AGA GAC GGT GAC CAT TGT CCC TGA GGA GAC GGT GAC CAG GGT TCC TGA GGA GAC GGT GAC CGT GGT CCC TGA CCG TGG TCC CTT GGC CCC AGA
PR2	VH LEADER1[†] VH LEADER2[†] VH LEADER3[†]	CR CTC CTG CTG CTG ACC A CR CTG AGC TGG RTT TTC CT	CDC42BPB°		IgM, IgG
PR3°	CDC42BPB1 CDC42BPB2	GAG CAC TGG CCA AGC ACT A CGG ATG GGC TCT GTG TGG	CH EPSILON1 CH EPSILON2		N/A
HuPo[‡]	HuPo	CCA TTC TAT CAT CAA CGG GTA CAA	HuPo		IgA
CD 154[§]	CD 154	CAC CTT CTC TGC CAG AAG ATA CCA TTT CAA	CD 154		Voswinkel (2001)

*Sequences of primers were from Cowell et al., 1999.
[†]R=A or G. K=G or T. Y=V or T.
°Sequences of primers were from Kim et al., 2010
[†]Sequences of primers were from Westlind−Johnsson et al., 2003
[§]Sequences of primers were from Haifa et al., 2001

a control for Q-PCR in peripheral blood mononuclear cells (PBMCs) [12].

Development of early diagnosis methods for AS at KIST-Europe

In order to develop an early diagnosis system for ankylosing spondylitis (AS), a known autoimmune disease, VH segment usage was analyzed in the PBMCs of patients with AS. The first set of our experiments was conducted with the PBMCs of eight AS patients who were being treated at the rheumatology clinic at Gachon University Gil Hospital in Korea and nine healthy donors. The patients with AS met the Modified New York Criteria and were regularly taking non-steroidal anti-inflammatory drug (NSAIDs) and sulfasalazine. Age, sex, disease duration, erythrocyte sedimentation rate (ESR), serum C reactive protein (CRP) and HLA-B27 positivity were assessed. Total RNA was
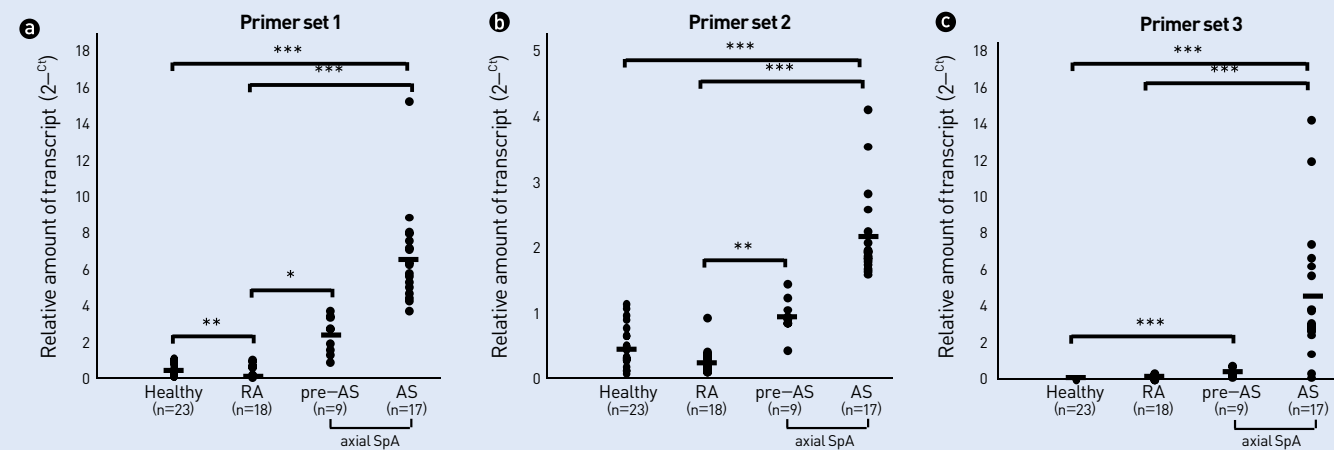
isolated from the PBMCs of both the healthy controls and AS patients using a RNAeasy Mini Kit (Qiagen, Hilden, Germany), and cDNA was synthesized using a Maxime RT PreMix (Oligo(dT)15 primer) Kit (Intron Biotechnology, Korea) following the manufacturers' instructions. PCRwas performed with primers as shown in Table 2. All primers were produced by MWG (Ebersberg, Germany).

To amplify VH regions, a set of 5'VH primers were used which are specific to each of the eight human VH gene families in combination with the mixture of five human JH gene families' primers. Through an active sequence search, two of the VH primers were added independently and were named VH2[ab] and VH4[ab]. The results from PCR with individual samples demonstrated that there were no significant differences in the PCR profiles between AS patients and the control group as produced by the PCR primer sets for VH1a-VH6a and for VH4ab; however, VH2[ab] genes represented by VH2[ab] forward primer were over-
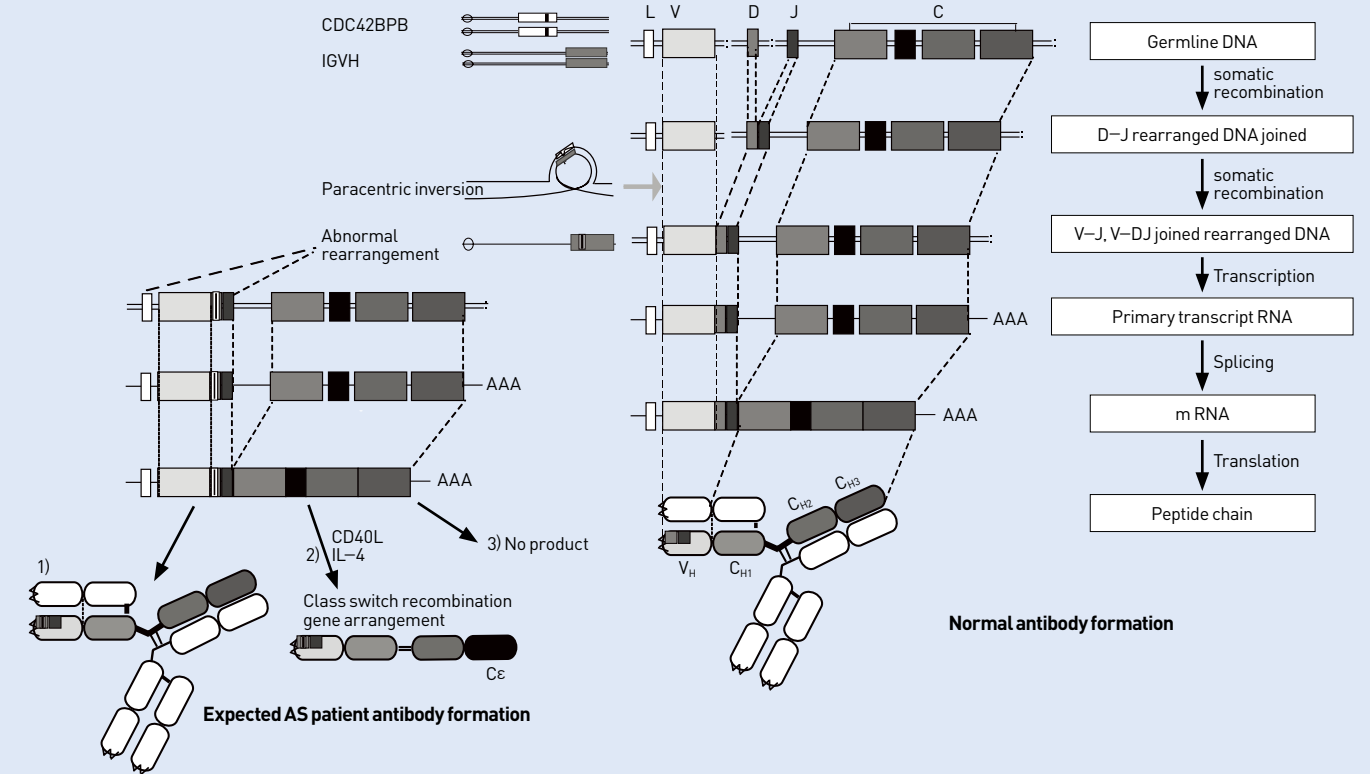
expressed exclusively in AS patients. The combination of VH2[ab] forward primer and five of the JH reverse primers were named PR1. On the basis of PCR analysis, Q-PCR was performed and a VH2[ab] library was constructed to analyze the sequence of over-expressed products. A significant difference was apparent in the level of expression of VH2[ab] genes between healthy donors and AS patients (relative amount of mRNA of VH2[ab] genes to human acidic ribosomal protein (HuPo), 0.68±0.55 [mean±SD] and 7.13±7.77, respectively; p←0.0001) The results of sequence analysis by bacterial cloning showed certain unique features of antibody VH fragments. Among the 100 sequence results, 48% of sequences revealed that a short fragment from the CDC42 BPB (CDC42 binding protein kinase beta) gene had been incorporated into a major part of cloned VH2[ab] PCR products. This short fragment was an intron fragment located in between a short stretch of VH2 and JH3. The inserted region encompassed 252 bps (36096-36348) of 125-kb of CDC42 BPB, which maps to 14q32.32 [14]. Subsequently, two more primer sets, PR2 and PR3, were designed in order to further investigate VH2[ab] genes. These

two sets of primer pairs amplified the inserted CDC42BPB gene and its surrounding regions. PR2 encoded from the VH leader gene to the inserted CDDC42BPB gene and PR3 encoded the CDDC42BPB gene to the IgC epsilon (Cε) region. Cε primer was chosen by conventional PCR analyses using Cμ, Cδ, Cγ, Cα and Cε primers and the result demonstrated that the expected PCR product could only be expressed by Cε primer.

The next set of experiments was conducted to evaluate the sensitivity and specificity of developed primers PR1, PR2 and PR3 for diagnosing AS. Q-PCRs were performed with an increased number of samples as follows: 9 from early-stage AS patients with symptoms consistent with AS but without X-ray evidence of structural damage in their joints, 17 from AS patients, 18 from RA (rheumatoid arthritis) patients and 23 from HCs (healthy controls). By using PR1, relative expression levels of uniquely assembled VH segments were determined to be approximately 28 times higher in AS patients and 6 times higher in early AS patients than HCs (Figure 2). In addition, PR1 was proved to have 96 % sensitivity and 95 % specificity in diagnosing

FIGURE 3 Human antibody VH region genes are constructed from gene segments. Unusual gene rearrangement or recombination may occur during construction of VH gene segments during B cell development in some of the AS patients. Paracentric inversion following recombination activating gene (RAG)-based recombination might be suggested to explain unique rearranged VH2ab gene structure.

FIGURE 2 Over-expression of VH2ab gene in axial SpA patients. Q-PCR was performed with cDNA from individual PBMC of HC, RA, pre-AS and AS patients using PR1 (a), PR2 (b) and PR3 (c). The relative amount of mRNA to HuPo was calculated as follows: ΔCt = Ct (experimental) - Ct (housekeeping), R = 2-(△Ct). Bars indicate means. Dots represent individuals. (*: P←0.01. **: P←0.05, ***: P←0.001)

early-stage AS. Q-PCRs conducted with PR2 and PR3 showed relative expression levels of uniquely assembled VH segments similar to those obtained with PR1. Further confirmation of the effectiveness of PR1, PR2 and PR3 was also made with considerably larger sample numbers. Q-PCR experiments were carried out with samples from 49 AS patients, 50 RA patients and 50 HCs. The results were in good agreement with our previous data.

Hypothesis

Sequence analysis and homology search of over-expressed VH2[ab] PCR products in AS patients' revealed unexpected

features of VH gene structure. In the sequences of VH2[ab] PCR products, a short stretch of intron sequences of CDC42 BPB was found between the VH and JH genes in the antibody repertoire of an AS patient. The most 5' end of this fragment included a region (15 nts) homologous to that of the VH2 germ line gene (IGHV2*70-12) and further analysis of inserted sequences helped identify a V-D junction and a DH6 sequence. Interestingly, the analysis of CDC42 BPB genomic sequences led to the identification of a heptamer-12bp spacer-nonamer RSS motif which was located following an insertion site of CDC42 BPB genes. In addition, a heptamer-like sequence (CACAGAG), which has a single nucleotide base, changed its features to those of a

generally known heptamer of RSS (CACAGTG). Nonamer-like sequences also appeared after 12 base pair spaces in the middle of the inserted CDC42 BPB intron genes. This gene structure implies that unusual gene rearrangement or recombination may occur during construction of VH gene segments during B cell development in some of the AS patients. Developing B cells and rearrangement of the V gene are known to depend on expressing recombination activating genes (RAGs). RAGs initiate V(D)J recombination by introducing a double-strand DNA break between the VH encoding region and recombination signal sequence (RSS). According to the sequence analysis, inserted regions in AS patients' antibodies contained RSS motifs of V-D and D-J junctions. Therefore, paracentric inversion following RAG)-based recombination initiation could explain the unique rearranged VH2[ab] gene structure (Figure 3).

To gather more supportive evidence for our hypo-thesis, CD40L gene expression was studied as well. CD40L is an inducer of Ig class switching, and it has also been reported that impaired CD40L expression can cause a defective Ig class switch recombination. Q-PCR analyses revealed that the CD40L gene was expressed at a rate two times higher in AS patients as compared with healthy controls as well as RA patients. This result suggests the potential involvement of CD40L in Ig class switching during AS pathogenesis, implying that there is a plausible link between immu-noglobulin production deficiency and AS.

The effect of uniquely rearranged VH segments in AS pathogenesis can be expected in several ways. If these segments continue to use the V region and produce antibodies, they might function as auto-antibodies. A binding partner screening from the serum of AS patients against this aberrant gene product would be informative. However, it is possible that the aberrantly rearranged Ig genes are not functional, making them incapable of producing protein. Nevertheless, aberrant Ig transcripts may still affect other Ig protein production or composition

in other ways. If an abnormally rearranged segment leads to the failure of antibody production, it could be translated to produce etiological or disease pro-gression signals. Moreover, even if it also failed to translate to polypeptides, it might still be able to induce an imbalanced antibody population or disturb the innate immune system. This implies that abnormally rearranged segments might indicate AS susceptibility.

Further investigations are required to verify whether distinct rearrangements of Ig VH genes are involved in B cell development or whether they function in terms of AS pathogenesis.

References

[1] Reveille JD, Arnett FC. Am J Med. 2005; 118(6): 592–603.
[2] Brown M A. Rheumatology (Oxford). 2008; 47: 132-37.
[3] Rudwaleit M, Listing J, Brandt J, Braun J, Sieper J. Ann Rheum Dis. 2004; 63: 665–670.
[4] Rostom S, Dougados M, Gossec L. Joint Bone Spine. 2010; 77: 108-114.
[5] Rostom S, Dougados M, Gossec L. Joint Bone Spine. 2010; 77: 108-114.
[6] O'Shea F, Salonen D, Inman R. J Rheumatol. 2007; 34: 5-7.
[7] Foreman AL, Van de Water J, Gougeon ML, Gershwin ME. Autoimmun Rev. 2007; 6: 387-401.
[8] Pfaffl MW. Nucleic Acids Res. 2001; 29: e45.
[9] Ståhlberg A, Zoric N, Aman P, Kubista M. Expert Rev Mol Diagn. 2005; 5: 221-230.
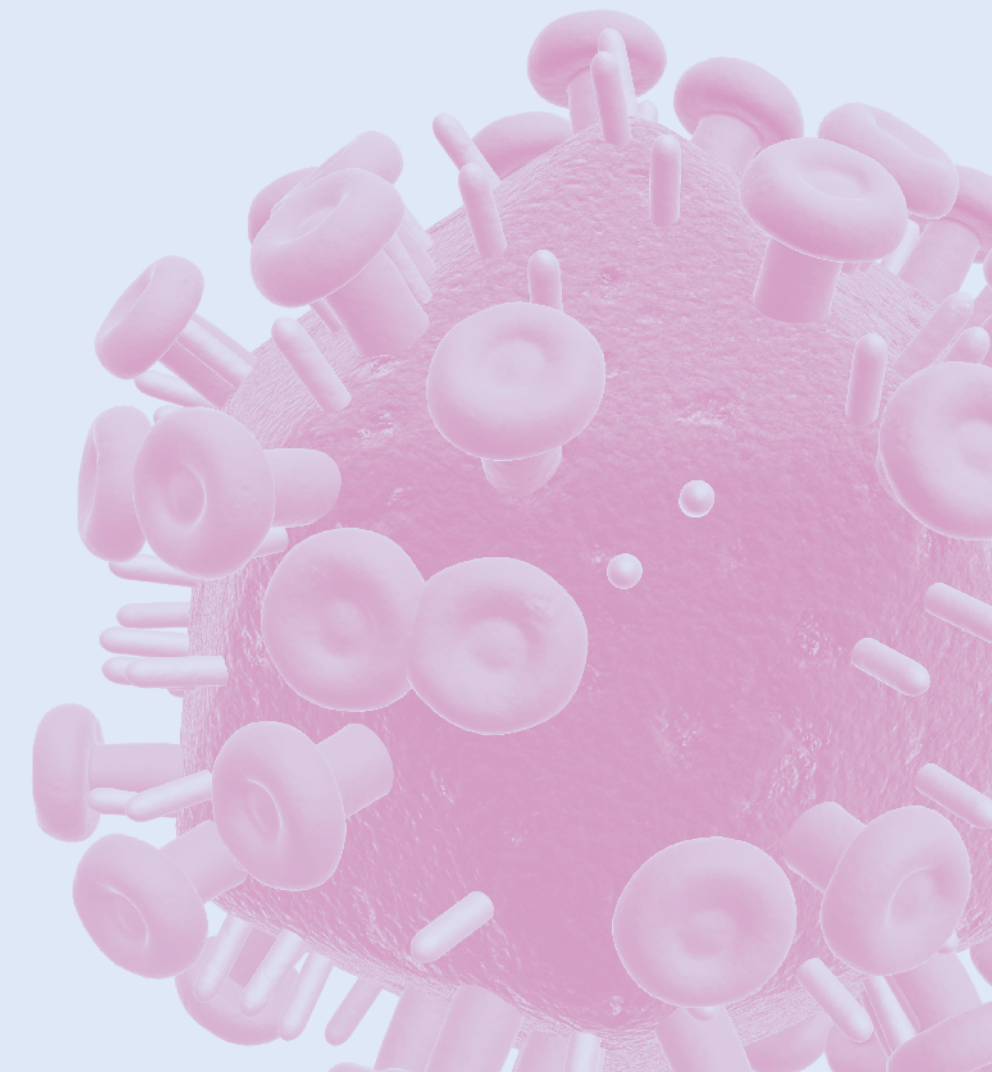[10] Ferre F. PCR Methods Appl. 1992; 2: 1-9.
[11] Raeymaekers L. Genome Res. 1995; 5: 91-94.
[12] Dheda K, Huggett JF, Bustin SA, Johnson MA, Rook G, Zumla A. Biotechniques. 2004; 37: 112-114, 116, 118-119.
[13] Schaad NW, Frederick RD, Shaw J, Schneider WL, Hickson R, Petrillo MD, Luster DG. Annu Rev Phytopathol. 2003; 41: 305-324.
[14] Moncrieff CL, Bailey ME. Genomics. 1999; 57: 297-300.

DNA-Based Biosensor Array Chip and Sensing System Using CMOS Technology

Seok Lee
Sensor System Research Center
• slee@kist.re.kr

Introduction

Recently, considerable research has been performed on the integration of sensors and bio-materials into biosensor systems. Even though various applications have been identified for biosensor systems in areas such as environmental and medical monitoring, security and defense fields, etc., development of these applications is at an early stage and intense research is required before commercialization is feasible. In this article, we present one possible approach among various methods under investigation in the Sensor System Research Center at KIST to develop a commercially viable biosensor system.

Our investigation focused on three main functional units of a biosensor system: (1) a sensor to pick up a sensing signal; (2) analog and digital signal processors to convert weak and noisy analog signals into meaningful digital information; and (3) a user-interface tool to wirelessly transmit processed signals to users for further applications. To be specific, we researched a carbon-nanotube (CNT)-based biosensor array chip (sensor unit), analog and digital signal processing chips (signal processing unit), and wireless communication through a smart-phone-based sensor monitoring module (user-interface tool). Among possible applications, we decided to utilize our biosensor system for lung cancer monitoring.

Through this type of research, we are trying to explore new worlds for application-oriented biosensor systems by integrating the two separate fields of biotechnology (BT) and information technology (IT) into one fusion technology.

Research Background

A sensor measures physical variation and converts it into electrical, mechanical or optical signals for meaningful signal acquisition. A sensor integrated with biological substances, called a biosensor, creates new ways to measure subtle changes and is applicable in many research fields.

The advantages of using a biosensor are that it provides fast and precise acquisition of signals with high sensitivity and can be easily modified for other purposes by changing the biological substances depending on the target applications. However, numerous issues, such as stabilization in the face of various external perturbations, portability, sample fixation, etc., remain to be resolved before biosensors will be ready for large-scale commercialization.

Recent trends in research on biosensors focus on portability for easy usage, low cost for wide popularity, and adoption of complementary metal-oxide semiconductor (CMOS) technologies. There are many possible forms of biosensors, but most recent research has focused on electro-chemical biosensors, which convert biological signals to voltage or current. Usually, a bio-sensor involves a very tiny signal. Therefore, System-on-Chip (SOC) circuit technology, which is able to acquire very tiny, but low-noise and low-offset signals, is also required. An additional requirement for a biosensor is to easily provide meaningful information to users.

To improve sensitivity, we incorporated carbon nanotubes (CNTs) into our biosensors. The use of CNTs is advantageous because the interface between sensors and biological systems, including neurons, is easy, and CNTs eliminate the need for previously required methods such as bound dyes or fluorescent probes.

Potential markets for biosensors include the following:
- Environment/ Conservation
  - BOD sensor, water and ocean pollution monitoring, pollution detection in various substances, heavy metal/toxic detection, M-TAS (total analysis system), etc.
- Food/Agriculture/Fisheries
  - Food safety monitoring, disease diagnosis in live animals and plants, quality control of meat/farm products, and various types of biological monitoring, etc.
  - This field currently represents 3% of the bio-sensor market; however, its growth rate is the highest among the applications identified thus far.

•Medical/Health
- Blood testing, gene analysis, functional genomics, proteomics, self-diagnostic testing (blood sugar level, HIV, etc.), pregnancy testing, endurance testing against toxic, medical devices, etc.
- This field currently represents 90% of the biosensor market, but 90% of these applications involve blood-sugar-level testing kits. (※Business Communications Company, Inc. (Norwalk, CT, USA), Theta (New York, NY), Provided by KISTI)
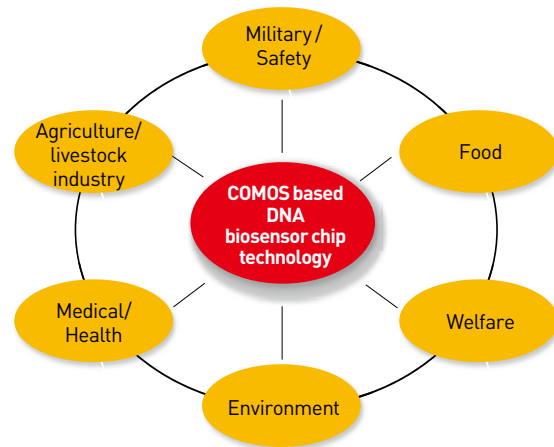
•Military/Safety
- Technologies designed for public safety, including illicit drug detection, explosive detection, bio/chemical weapon detection, etc.
- This area represents a newly e-merging market; however, due to security and regulatory consider-ations, only specially certified busi-nesses or government units are likely to participate in its deve-lopment.

FIGURE 1 Applications of CMOS based bio-sensor chip

Biosensor Chip

1X4 CNT sensor array

In this section, we briefly explain the general fabrication process for our biosensor. We manufactured a sensor array by fixing DNA or olfactory cells on CNTs. In order to manufacture the CNTs, we used a semi-conductor fab process and enabled a self-assembly effect of the CNT on the solid surface by means of an electric charge. We began by aligning markers on the SiO_2 semi-conductor substrate to protect the eventual CNT channels. We then coated the exposed substrate with a film of octadecyltrichlorsilane (OTS).In order to create a designed coating of OTS film, we used a patterning photoresist with a designed shape on the solid surface. We then eliminated the photoresist after dipping the semi-conductor substrate into an OTS solution. OTS film generated in this way prevents non-specific absorption of CNTs. When we dipped the SiO_2 semi-conductor substrate coated by OTS film into a suspension with well-distributed CNTs, the CNTs were selectively absorbed on the SiO_2 surface. Finally, using a photolithography process, we made electrodes on the semi-conductor substrate. This process for manufacturing a CNT sensor array is shown in Figures 2 and 3.
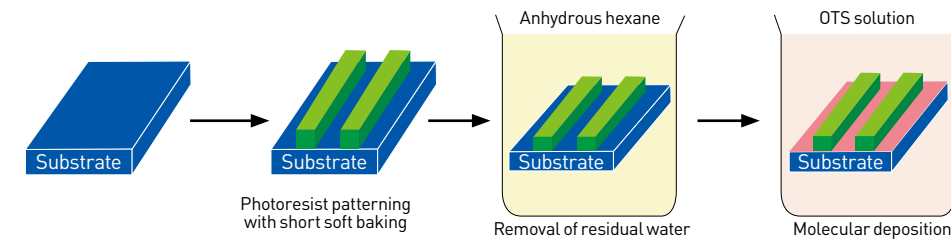

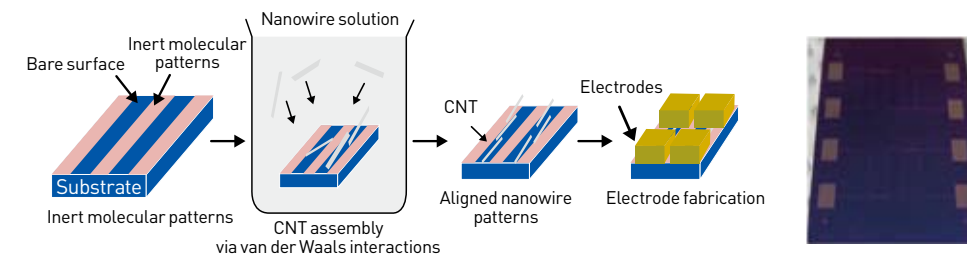**FIGURE 2** Coasting process of the hydrophobic film on the board

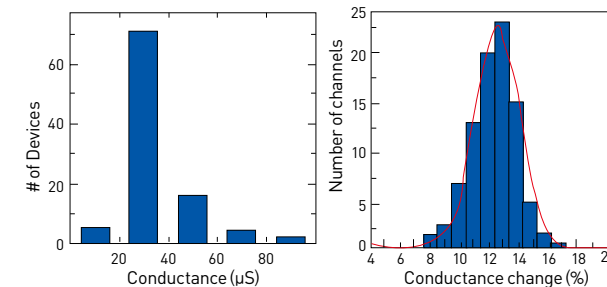**FIGURE 3** CNT sensor array manufacturing process and 1X4 CNT sensor array

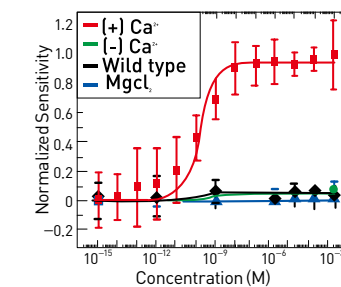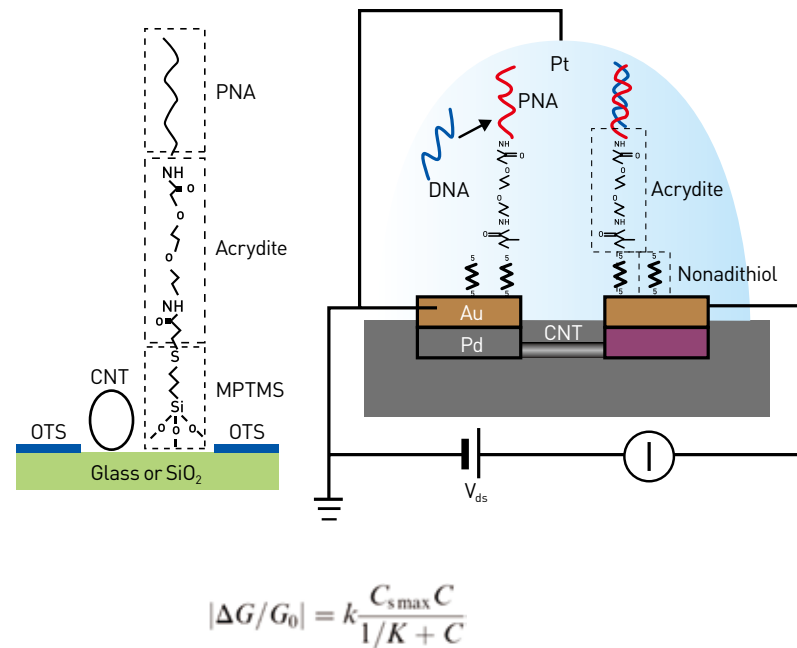**FIGURE 4** Conductivity of CNT sensor and reactivity distribution of DNA detection

FIGURE 5 Sensitivity graph of CNT sensor with odor substance concentration

The theory behind a CNT sensor is to detect a transition of current which runs on CNT channels with an electric field around the CNT caused by a target substance. The conductivity of our designed CNT sensor is focused on about 30us and reactivity with DNA detection has a Gaussian distribution with 12% mean reactivity.

We confirmed the detection algorithm of the CNT sensor. The CNT sensor really reflects the reactions between the receptor around the CNTs and the target substance. We also proved that the sensitivity graph of the CNT sensor was almost equivalent to the Langmuir isotherm theory, as can be seen in Figure 5.

**FIGURE 6** DNA fixing on the CNT and detecting of complementary DNA

$$|\Delta G/G_0| = k\frac{C_{s\,max}C}{1/K + C}$$

C: concentration of target substance; Csmax: maximum surface concentration of receptor; K: reaction constant; G: conductivity of CNT sensor

Fixing DNA on the sensor

It is very important to fix DNA or olfactory cells onto the CNTs. We accomplished this using various linker molecules. In order to use CNT channel characteristics with semi-conductivity for detecting DNA, we fixed DNA onto a SiO_2 surface around CNTs using MPTMS and Acrydite. In order to use characteristics of the Schottky barrier between the CNTs and electrodes, we fixed DNA onto the surface of the electrodes using Nonadithiol and Acrydite. Figure 6 shows the structure of fixed DNA on the CNTs and the detection algorithm of the complementary DNA.
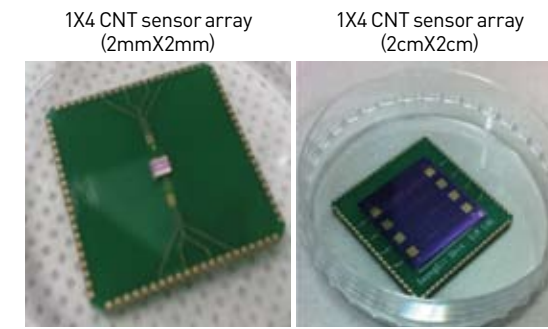
Sensor test results

We fixed DNA onto the CNT sensor and then inserted DNA into the sensor. As a result,
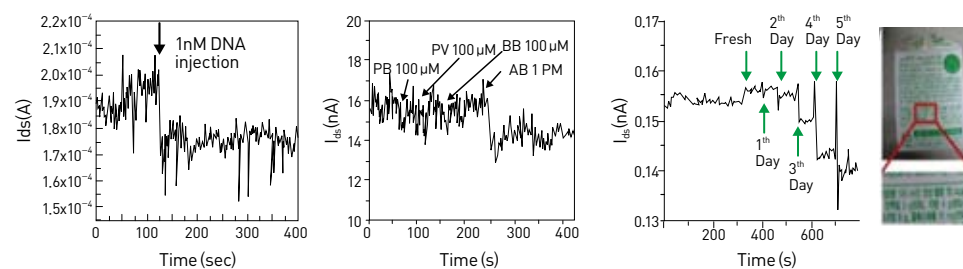
FIGURE 7 Detection of 1nM DNA, detection of 1pM odor substance using olfactory cell and decompositon graph of the milk
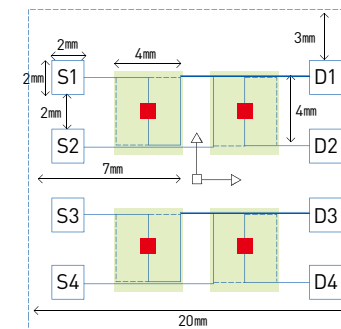
FIGURE 8 Structure of 1X4 CNT sensor chip


FIGURE 9 1X4 CNT sensor array chip

only complementary DNA reacted and we were able to measure DNA with a 1nM level concentration. In addition, we fixed olfactory cells onto the CNT sensor and were able to detect an odor at 1pM-level concentration. In order to apply this sensor to our daily lives, we devised a test to detect food decomposition. We fixed olfactory cells which reacted with hexanal into the CNT sensor. Hexanal is generated when food decomposes. We inserted decomposed milk and confirmed that it reacted with the CNT sensor. The test results are as follows. The design structure of the proposed 1X4 CNT sensor array is shown in Figure 8. It has four channels with source and drain electrodes. Its size is about 2cmX2cm. We made two kinds of sensors which are displayed in Figure 9. The difference between the two is their size. Initially, we designed a 1X4 CNT sensor array with a size of 2mmX2mm.To detect the targeted substance, we put a drop of liquid onto the sensor array. It was particularly important to separate each channel sensor in order to detect each channel independently, but this was impossible to do with the 2mmX2mm sensor array because of its small size. Therefore, we redesigned the 1X4 CNT sensor array with a larger 2cmX2cm size.

Signal Processing Unit and Sensor System

Analog signal processing unit

The structure of the proposed analog signal processing chip is reflected in Figure 10. It was designed to process an 8X8 DNA sensor signal and to consume little power because it will be used in a mobile sensor platform. It has 64 channels with 640 symbols per second, an operating voltage of 1V, and power consumption of 70uW. It includes an active input current mirror for sensor voltage bias and the initial amplification of sensor signal. It features a variable gain I-V converter for wide-range signal detection and SAR (successive approximation register) analog-to-digital converter (ADC) for rapid conversion of signals from analog to digital.

FIGURE 10 Low powered SoC structure for detecting 8X8 DNA sensor signal
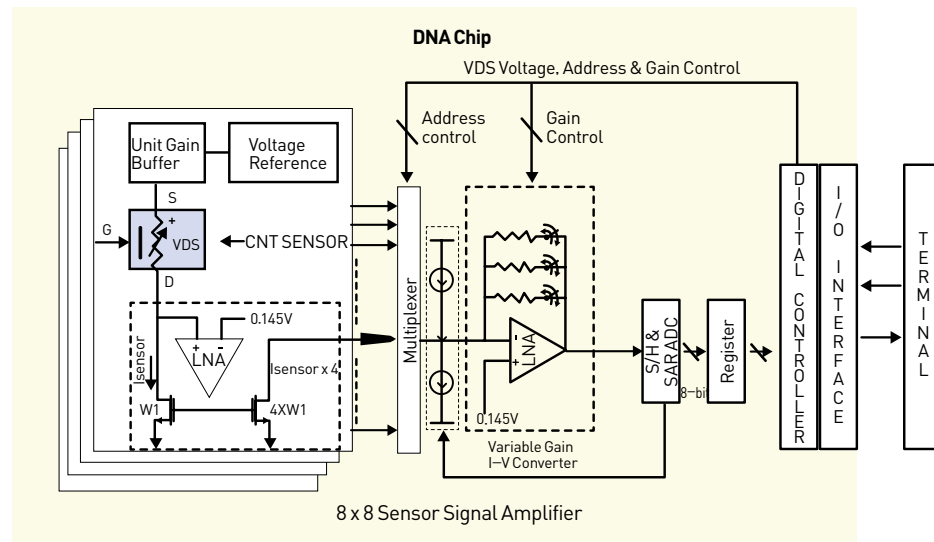
FIGURE 11 Simulation result of low powered SoC for detecting 8X8 DNA sensor signal

| Feature	Performance
Fabrication Process	Samsung 0.13um
Chip Die Size	4mm X 4mm
Number of Channels (External)	48 channels (total 64 channels)
Detection Speed	640S/s
Operating Voltage	1V
Power Consumption	70uW

TABLE 1 Chip performance

Simulation results of the analog signal processing chip described above is shown in Figure 11. The sensor model is defined as FET and we input a 0.5% current change. During the simulation, digital output changed 0.5% with 1 bit, indicating that the DNA chip worked well.

The manufactured chip was fabricated by the Samsung 0.13um process and had an area of about 4mmX4mm. It had 64 channels so it could detect 64 sensor channels. However we used only 16 channels in the test, so we can use 48 channels in practice. The inputted sensor signal ranged from 10nA to 10uA, equivalent to 10kΩ to 10MΩ at the resistant level. The performance of the manufactured chip is summarized in Table 1 below.
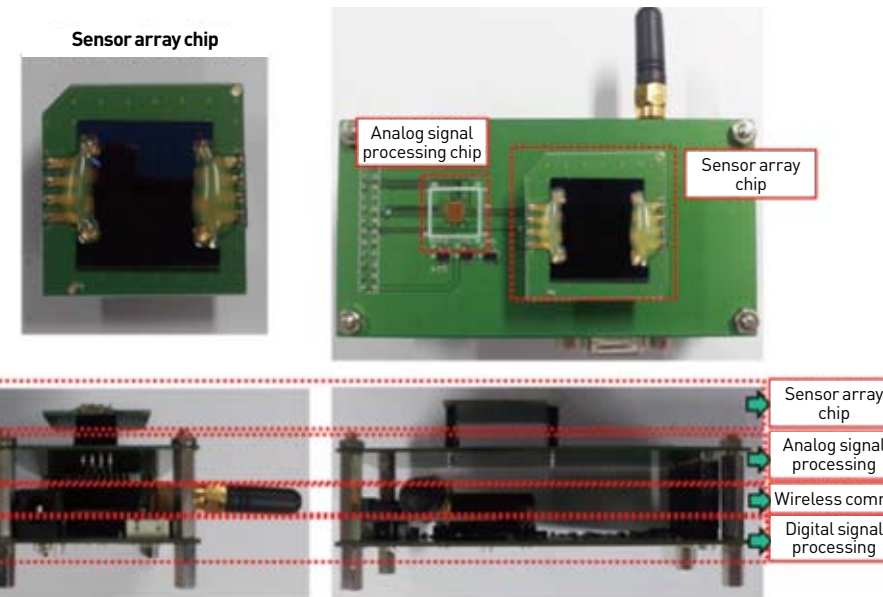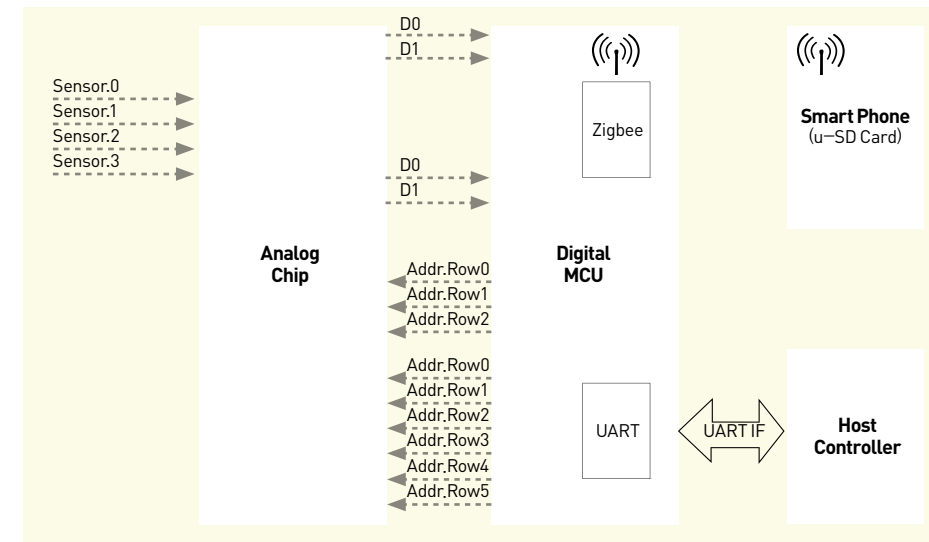
Sensing system

A digital interface circuit includes serial communication and a ZigBee communication interface. It uses a digital interfacing circuit and signal level converter for interfacing

Analog signal processing chip die
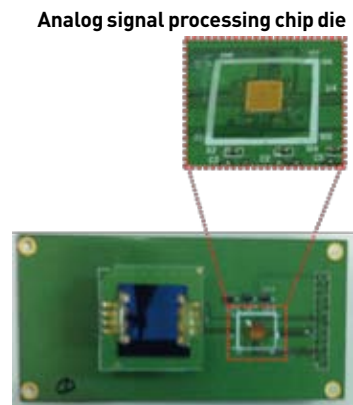
Analog signal processing board ver.1.1

FIGURE 12 Analog signal processing board and signal processing chip die

FIGURE 13 Interface of analog chip & digital MCU
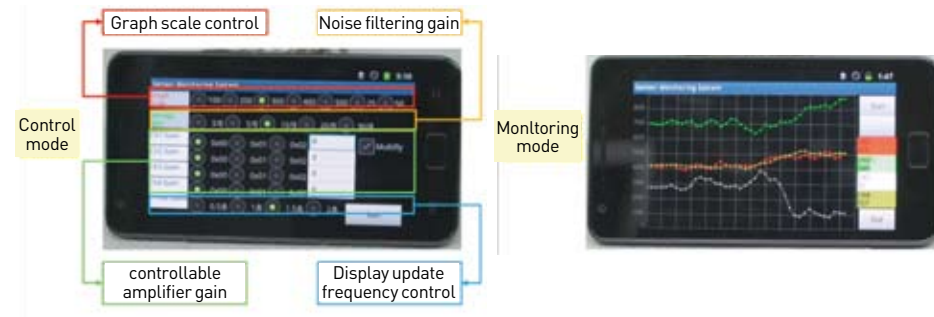
Sensor array chip

FIGURE 14 1X4 sensor array based sensing system

the signal levels between the analog and digital segments for 4-channel analog signal processing. A digital MCU receives the sensor channel data through a data line using a configured address and then sends it to a mobile device, such as a smartphone. Additionally, the MCU gets the sensor configuration information from the mobile device through a wireless datalink and control sensor. The interfacing structure is detailed in Figure 13.

We designed a sensor system that essentially functions as a type of Plug-In & Play. The sensor system platform included a biosensor chip that could be replaced after the

FIGURE 15 Smartphone application for sensor array control/monitoring

Graph scale control

Noise filtering gain

Control mode

Monltoring mode

controllable amplifier gain

Display update frequency control

FIGURE 16 Sensor system test

Lung cancer marker (hexanal) in serted

Mixed DNA inserted

Lung cancer detecting using sensor system

DNA detecting using sensor system

sensing function was accomplished. Since a biosensor with DNA/olfactory receptors cannot be refreshed because it senses liquid substance, we developed a Plug & Play-type sensor platform to permit replacement of the biosensor chip after use. The complete sensor system is shown in Figure 14.

The complete sensing system includes a biosensor array chip, an analog signal processing chip, a digital signal processing board and a wireless datalink module. Additionally, we developed smartphone application software to control the sensor and to monitor the sensor signal. This application was developed based on versions 2.2. and 2.3 of the android platform. It includes real-time sensor output monitoring, noise filtering of sensor outputs, control of amplifier gain parameter scaling, and configuration of logging frequency and display update rate. It also supports a ZigBee communication network for a USN (ubiquitous sensor network) using a ZigBee-supported micro SD card.

Test Results

We used two approaches for the testing of our sensor system. The first approach was to detect hexanal, a lung cancer marker, by using olfactory cells fixed into the 1X4 CNT sensor array. Channels 1 and 2 of the CNT sensor array were coated with olfactory cells for amyl butyrate, channel 3 was coated with olfactory cells for hexanal, and channel 4 was coated with olfactory cells for nonanal. In the test, we inserted the lung cancer marker into the sensor array and were able to confirm that channel 3, containing the olfactory cells sensitive to hexanal, reacted while the white decreased.

Our second approach was to detect a DNA sequence. We fixed the DNA sequence (CH1 : AGGTCGCCGCCC (12mer), CH2 : CCTAATAACAAT (12mer), CH3 : GTTCTTCTCATCATC (15mer), CH4 : CATTCCGAGTGTCCA (15mer)) into the 4 channels of the sensor array, and then inserted mixed DNA. As illustrated in Figure 16, all channels reacted to the inserted DNA mixture.

The results of both these tests indicate that the system operated successfully in a mobile platform and worked in real time.

Conclusion

Our research integrated biosensor technology and IT-convergence technology to develop a mobile sensor system which included a CNT-based biosensor array chip, analog signal processing chip, digital signal processing module, wireless communication module and smartphone application for monitoring purposes. Using this sensor system, we detected lung cancer markers with olfactory cells. We also detected DNA, thus proving the feasibility of this sensor system.

The future of bio-sensor technology is wide open for the development of useful applications in environmental, medical, health, safety, military and other fields. Considerable research will be needed before viable applications are ready for commercialization, but the sensor system research we have described in this article reflects the tremendous potential of this technology.

Method for Suppressing Beat Noise in Brillouin Distributed Temperature and Strain Sensing

Kwan Il Lee

Ji Ho Jeong

Sang Bae Lee

Center for Opto-Electronic Convergence Systems
• klee21@kist.re.kr

Introduction

Distributed fiber sensors based on Brillouin scattering provide an excellent method for measuring strain or temperature variations over long distances (> 100 km) with decent accuracy [1-9]. Brillouin sensors commonly share the operation principle that the shift of a local Brillouin frequency (v_B) is proportional to the strain and temperature variation applied to a fiber under test, and various types of measurement schemes have been proposed based on spontaneous or stimulated scattering by time- or correlation-domain approach [2-7]. Since the spontaneous scattering based method suffers from an extremely low level of the detected signal, several kinds of stimulated Brillouin scattering based sensors have been studied such as Brillouin optical time domain analysis (BOTDA) and Brillouin optical correlation domain analysis (BOCDA). In the case of BOTDA, a pulsed pump wave and a continuous probe wave are counter-propagated in a fiber under test (FUT) and the spatial resolution is determined by the pulse width. On the other hand, in BOCDA, a sinusoidal frequency modulation (FM) is applied to both continuous-wave (CW) probe and pump waves, which results in the generation of stimulated Brillouin scattering (SBS) only at a single correlation position along the FUT [6, 10-13]. The acquisition of the Brillouin gain spectrum (BGS) is carried out by applying various types of lock-in detection with the chopping of the pump or both pump and probe waves [6, 10, 14]. To measure the distribution of the BGS, the position of the correlation peak needs to be swept along the fiber by changing the FM frequency f_m. Since several frequency components appear in the operation of the BOCDA, it is not straightforward to avoid an intensity noise coming from the beating of the frequencies which may lead to the failure of the measurement by distorting the acquired BGS. So far such a beat noise in a BOCDA system has not been analyzed in detail, and no established solution has been reported.

In this article, we provide the first theoretical analysis of the beat noise in an ordinary BOCDA system, and show that the rise of the noise depends on the frequency relation between f_m and a chopping frequency f_l of the lock-in detection. Based on the results, we propose a novel method of continuously varying the chopping frequency to circumvent the beat noise in BOCDA.

Principle

In BOCDA, a pump wave and a probe wave counter-propagating along a fiber under test (FUT) are frequency-modulated with a sinusoidal waveform by direct current modulation of a laser diode (LD) to generate a single correlation peak within the FUT where the stimulated Brillouin scattering (SBS) occurs strongly and exclusively. The Brillouin gain of the probe wave is measured through a lock-in amplifier (LIA) operated synchronously to a reference wave used for the chopping of the pump wave [6]. The BGS is obtained by sweeping the frequency offset between the pump and the probe waves, and the measurement position is swept by changing the FM frequency (f_m) applied to the LD. The direct current modulation of the LD is necessarily accompanied by an intensity modulation in the output at the same frequency f_m, which generally distorts the shape of the measured BGS in the BOCDA [15].

In order to analyze the effect of the intensity modulation on the lock-in detection we assume the measurement configuration of the BOCDA as shown in Figure 1.

When a sinusoidal intensity modulation is applied, the intensity of the pump and the probe waves at a correlation peak can be expressed as follows:
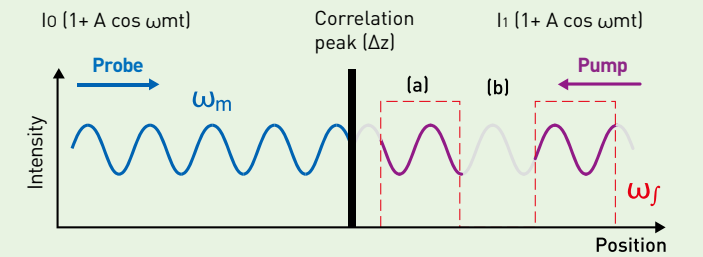
FIGURE 1 The interaction of the pump and the probe waves near a correlation peak in the BOCDA with an intensity chop of a square wave (dashed in red) applied to the pump wave

$$I_{Pump} = I_1(1 + A\cos\omega_m t) \tag{1}$$

$$I_{Probe} = I_0(1 + A\cos\omega_m t) \tag{2}$$

where A is the modulation depth with $0 \leq A \leq 1$ and $\omega_m \equiv 2\pi f_m$. According to the basic principle of the BOCDA, the frequency modulations of the pump and the probe waves are always in-phase at a correlation peak [6]. Therefore, it is notable that the intensity modulations of the pump and the probe waves are also in-phase at the correlation peak since the relative phases of the frequency and the intensity modulations are constant under the direct current modulation of a LD. In addition, the shapes of the intensity modulation for the pump and the probe waves are expected to be identical when a common sideband-generation method is adopted for the control of the frequency offset between the pump and the probe waves [3, 6]. If the effective length of the correlation peak (i.e., the spatial resolution of the BOCDA) is Δz and the Brillouin gain is small enough (as in ordinary cases), the probe intensities through the correlation peak in the presence (I_a) and the absence (I_b) of the pump wave (i.e., (a) and (b) in Figure 1) are calculated as follow:

$$I_a = I_{Probe}e^{g_B I_{Pump}\Delta z} \approx g_B \Delta z \cdot I_0 I_1(1 + A\cos\omega_m t)^2 + I_0(1 + A\cos\omega_m t) \tag{3}$$

$$I_b = I_0(1 + A\cos\omega_m t) \tag{4}$$

where g_B is the Brillouin gain coefficient of the fiber. We assume the intensity chop of the pump wave is applied in the form of a square wave at an angular frequency ω_l (dashed rectangle in Figure 1), and the intensity of the probe wave is converted to a voltage by a photo detector (PD) with a conversion coefficient B to be input to the phase-detector of the LIA. Using the square wave at ω_l as a reference wave, the voltage output from the phase-detector of the LIA is calculated by integration as follows:

$$V_{out} = B\left[\int_{\tau}^{\tau+\frac{\pi}{\omega_l}} I_a dt - \int_{\tau+\frac{\pi}{\omega_l}}^{\tau+\frac{2\pi}{\omega_l}} I_b dt\right]$$

$$= \int_{\tau}^{\tau+\frac{\pi}{\omega_l}}\left\{C_1\left(1+A\cos(\omega_m t+\varphi(\tau))\right)^2 + C_2\left(1+A\cos(\omega_m t+\varphi(\tau))\right)\right\}dt$$

$$- \int_{\tau+\frac{\pi}{\omega_l}}^{\tau+\frac{2\pi}{\omega_l}}\left\{C_2\left(1+A\cos(\omega_m t+\varphi(\tau))\right)\right\}dt \qquad (5)$$

where τ is a starting time of the phase-detection, $\varphi(\tau) \equiv (\omega_m - \omega_l)\tau + \varphi_0$ is a relative phase between the modulation and the chopping waves (φ_0 is a constant offset), $C_1 \equiv Bg_B\Delta z I_0 I_1$, and $C_2 \equiv BI_0$. The integration is easily evaluated and the result is rearranged in terms of C_1 and C_2 as follows:

$$V_{out}(\tau) =$$

$$C_1\left\{\left(1+\frac{A^2}{2}\right)\frac{\pi}{\omega_l}+\frac{4A}{\omega_m}\cos\left(\omega_m\tau+\varphi(\tau)+\frac{\pi\omega_m}{2\omega_l}\right)\sin\left(\frac{\pi\omega_m}{2\omega_l}\right)+\frac{A^2}{2\omega_m}\cos\left(2\omega_m\tau+2\varphi(\tau)+\frac{\pi\omega_m}{\omega_l}\right)\sin\left(\frac{\pi\omega_m}{\omega_l}\right)\right\}$$

$$+C_2\left\{\frac{2A}{\omega_m}\sin\left(\omega_m\tau+\varphi(\tau)+\frac{\pi\omega_m}{\omega_l}\right)-\frac{2A}{\omega_m}\sin\left(\omega_m\tau+\varphi(\tau)+\frac{\pi\omega_m}{\omega_l}\right)\cos\left(\frac{\pi\omega_m}{\omega_l}\right)\right\} \qquad (6)$$

As seen in (Equation 6), V_{out} is a function of τ including beat-frequency components such as $2\omega_m - \omega_l$ and $4\omega_m - 2\omega_l$. In practice, the waveform of the intensity modulation or the intensity chop of the pump wave may include higher-order harmonic terms by modification, which would contribute more frequency components to V_{out}. Since ω_m is swept according to the position of the correlation peak in distributed measurements, it is possible for some of the beat-frequency components to pass the low-pass filter of the LIA and distort the acquired BGS to give rise to a beat

noise.

In particular cases of $\omega_m = 2n\omega_l$ (n is a positive integer) in (Equation 6), all the τ-dependent components of V_{out} vanish to yield a simple equation as follows:

$$V_{out} = C_1\left(1+\frac{A^2}{2}\right)\frac{\pi}{\omega_l} = Bg_B I_0 I_1 \Delta z\left(1+\frac{A^2}{2}\right)\frac{\pi}{\omega_l} \qquad (7)$$

Therefore, one can expect to acquire a pure BGS that is free from the beat noise of the LIA by controlling f_l according to f_m in the following way:

$$f_l = \frac{f_m}{2n} \qquad \text{(n: positive integer)} \qquad (8)$$

It is worthwhile to comment on the ω_l-dependence of V_{out} in (Equation 7). According to (Equation 5), V_{out} is calculated by the integration during the time interval of $1/f_l$ for simplicity, so it finally includes the term of $1/f_l$. However, in common use of a lock-in amplifier, the integration time (i.e. time constant) is fixed and V_{out} does not depend on the chopping frequency f_l.
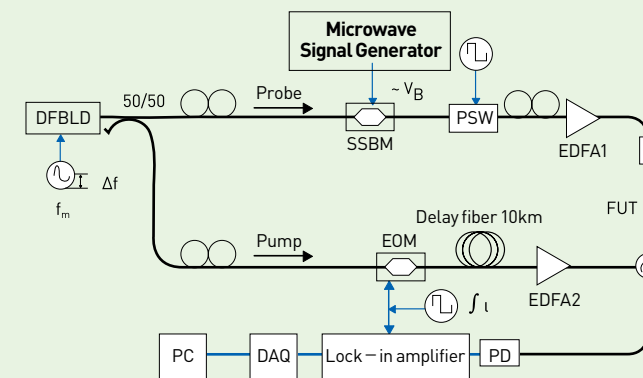
Experimental results

We set up a BOCDA system to confirm our theoretical analysis as shown in Figure 2. A 30 m single-mode fiber (SMF) was used as a FUT, the v_B of which was about 10.853 GHz. A 1548nm distributed feedback LD (DFB-LD) was used as a light source, and a sinusoidal frequency modulation was applied to generate a correlation peak within the FUT. The modulation frequency f_m was varied between 2.993 and 3.004MHz depending on the measurement position (i.e., the correlation peak), and the modulation amplitude (Δf) was about 3.4GHz, from which the spatial resolution and the measurement range were estimated to be about 10cm and 32m, respectively. The output from the LD was divided into two beams by a 50/50 coupler. One of the beams was used as the Brillouin pump wave after passing through a 10km
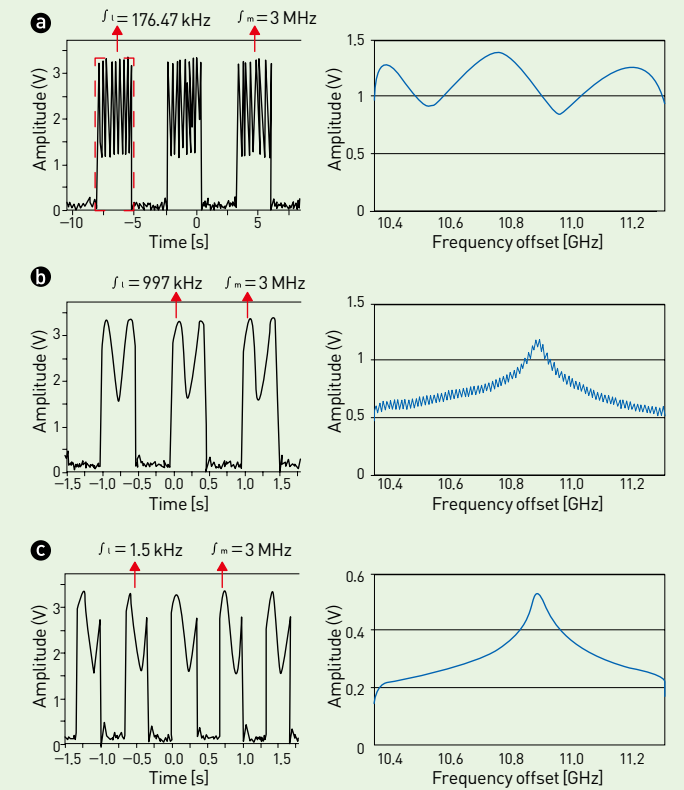
delay fiber to control the order of correlation peak and a high power erbium doped fiber amplifier (EDFA) to boost up the pump power to 23dBm. The other beam was injected into a single sideband modulator (SSBM) which was driven by a microwave signal generator, so that the first lower sideband, serving as the probe wave, was generated and propagated along the FUT in the opposite direction to the pump wave. Additionally, a polarization switch (PSW) was inserted after the SSBM for suppressing the polarization dependence of the Brillouin signal [16], and another EDFA was used to compensate for the insertion loss of the SSBM. The pump light was chopped by an intensity modulator with a square waveform for lock-in detection. A 125MHz photo receiver was used as a detector and the BGS was obtained through a LIA (SR844). In the distributed measurement, the BGS was acquired every 10cm along the FUT, sweeping Δv from 10.3 to 11.3GHz. The sweep time was 0.1 s and the number of data point for a single BGS was 1200.

At first, the time constant and the output filter of the LIA were set 300µs and 24dB/octave, respectively, as a common configuration for BOCDA systems, and the BGS were measured varying f_l under f_m fixed to 3MHz so that the ratio f_m to f_l was swept from 1 to 20 with a step of 0.01. Figure 3 shows some of the measured BGS together with corresponding shapes of the pump wave. As seen in Figure


FIGURE 3 Examples of the measured Brillouin gain spectrum (right) and the corresponding pump waveform (left) with different frequency ratio f_m to f_l: (a) 17, (b) 3.01, and (c) 2.

3a and 3b, strong distortions of the BGS with low and high frequency noises appear in some cases, while a clear BGS is also observed in other cases like Figure 3c depending on the frequency ratio. It is notable that the amplitude of the beat noise periodically became larger when the frequency ratio approaches odd numbers as exampled by Figure 3a and Figure 3b and minimized near the ratio of even numbers like Figure 3c. We think this feature could be explained by (Equation 6) where the acquired BGS becomes temporally and also spectrally modulated due to the τ-dependent parts of V_{out} which periodically vanishes at frequency ratios of even numbers. It is also remarkable that in this first measurement the occurrence of the beat noise was limited to narrow frequency bands near particular frequencies of f_l corresponding to the range within ±0.02 in

FIGURE 2 Experimental setup of a BOCDA system
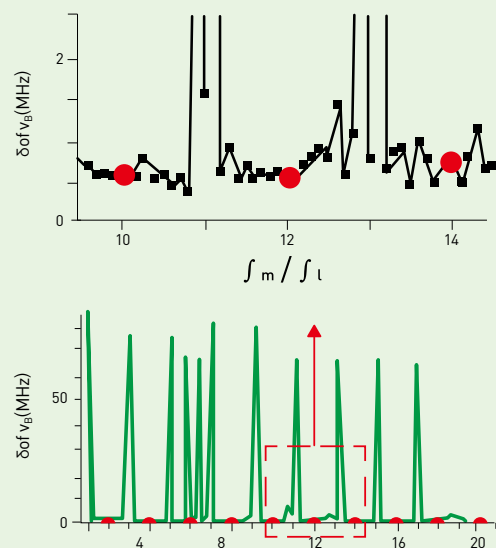
FIGURE 4 Standard deviation of the detected Brillouin frequencies in 20 repetitive measurements as a function of f_m / f_l. Note that red spots correspond to f_m / f_l of even numbers, and the insets are the zoomed views.
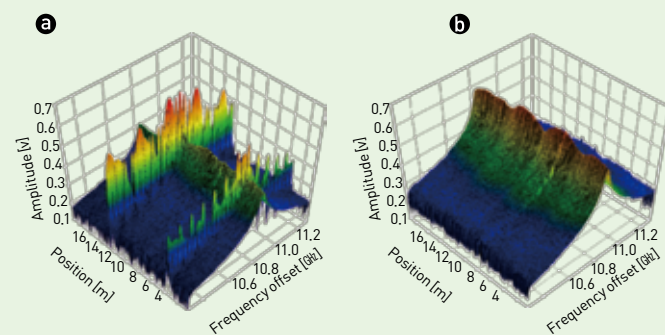
FIGURE 5 Comparison of the distributed measurements of the BGS along a 30 m FUT by BOCDA system based on (a) ordinary lock-in detection with a fixed chopping frequency f_l =1.004987MHz and (b) variable frequency lock-in detection with $f_l = f_m /4$.

terms of the frequency ratios (for example, 3±0.02, 5±0.02 etc.), which is due to the existence of the output filter in the LIA suppressing high frequency beat noises.

For inspecting the detailed properties of the beat noise, we turned off the output filter of the LIA and measured the BGS varying f_l under f_m fixed to 3MHz so that the ratio f_m to f_l

was swept from 1 to 20 with a step of 0.1. This time, the BGS was acquired 20 times for each f_l.

Figure 4 is the standard deviation of the Brillouin frequency v_B fitted from the BGS of the 20 repetitive measurements as a function of the frequency ratio which indicates the measurement error. This result shows that the measurement error is also decreased to below ±1MHz when the frequency ratio is chosen among even numbers (red spots) as expected in (Equation 8). On the other hand, the beat noise tends to reach local maxima when the frequency ratio approaches odd numbers, which is partly explained by the fact that effects of τ-dependent terms in (Equation 6) related to $\sin(\pi\omega_m/2\omega_l)$ and $\cos(\pi\omega_m/\omega_l)$ are maximized at such cases.

From the above results, it is expected that the beat noise can be minimized by varying f_l of the lock-in detection in such a way that the ratio of f_m to f_l remains equal to an even number during the position sweep in BOCDA systems. To confirm the performance of the proposed scheme, we carried out distributed measurements with BOCDA systems using the ordinary and the variable frequency lock-in detection. The time constant and the output filter of the LIA were reset to 300μs and 24dB/octave, respectively. In the case of the ordinary lock-in detection f_l was fixed to a prime number (1.004987MHz), and in the case of the variable frequency lock-in detection f_l was varied according to (Equation 8) with the frequency ratio of 4. The measurement results are shown in Figure 5, where the acquired BGS's were strongly distorted at some positions (i.e. f_m's) by the beat noise in the ordinary lock-in detection as depicted in Figure 5a. On the contrary, it is confirmed that stable and clear BGS's are maintained along the FUT with the variable frequency lock-in detection as shown in Figure 5b.

Conclusion

We have analyzed the beat noise phenomenon related to intensity modulation and lock-in detection in Brillouin optical correlation domain analysis, and newly proposed variable frequency lock-in detection as a simple way to circumvent the beat noise. Additionally, we think our scheme can be applied to a standard modulator with double sidebands as well as to an SSBM, since the rise of the beat noise is connected only with the frequency relation between the current modulation of the LD and the chopping for lock-in detection. Moreover, this new method will be useful in stabilizing the operation of BOCDA systems in strain monitoring of civil structures, especially for long-range measurement where large variation of the FM frequency is necessary for the position sweep.

Note

This article is based on our recent paper: Optics Express. 2011; 19: 18721.

References

[1] Li H-N. Eng Structures. 2004; 26: 1647–1657.
[2] Horiguchi T, Kurashima T, Tateda M. IEEE Photon Technol Lett. 1990; 2: 352-354.
[3] Nikles M, Thevenaz L, Robert P. Opt Lett. 1996; 21: 758-760.
[4] Bao X, DeMerchant M, Brown A, Bremner T. J Lightwave Technol. 2001; 19: 1698-1704.
[5] Alahbabi MN, Cho YT, Newson TP. J Opt Soc Am B. 2005; 22: 1321-1324.
[6] Hotate K, Hasegawa T. IEICE Trans Electron. 2000; E83-C: 405-412.
[7] Mizuno Y, Zou W, He Z, Hotate K. Optics Express. 2008; 16: 12148-12153.
[8] Soto MA, Bolognini G, Di Pasquale F. Opt Lett. 2011; 36: 232-234.
[9] Dong Y, Chen L, Bao X. Opt Lett. 2011; 36: 277-279.
[10] Song KY, He Z, Hotate K. Opt Lett. 2006; 31: 2526-2528.
[11] Li W, Bao X, Li Y, Chen L. Opt Express. 2008; 16: 21616-21625.
[12] Jeong JH, Lee K, Jeong J-M, Lee SB. OSA/CLEO. 2011; paper CFM3.
[13] Jeong JH, Lee K, Song KY, Lee SB. ECOC. 2011; 4: paper Tu.6.LeCerbin.
[14] Song KY, Hotate K. IEEE Photon Technol Lett. 2006; 18: 499-501.
[15] Song KY, He Z, Hotate K. J Lightwave Technol. 2007; 25: 1238-1246.
[16] Hotate K, Abe K, Song KY. IEEE Photon Technol Lett. 2006; 18: 2653-2655.

Controlling Liquid Behavior by Tuning Surface Wettability

Myoung Woon Moon
Center for Computational Science
• mwmoon@kist.re.kr

**Kwang Ryeol Lee**

Seong Jin Kim

Introduction

Academic and industrial researchers have recently been paying considerable attention to tuning the wettability of surfaces in relation to two specific phenomena: superhydrophobicity (an extreme water-repelling state) and superhydrophilicity (an extreme water-attractive state). These properties have proven useful in various industrial applications such as anti-fouling, dehumidification, desalination, and water–oil separation. Both extreme wetting states can be achieved by tuning surface roughness and surface energy. Superhydrophobicity is commonly defined as a state in which a spherical-shaped water drop exhibits a high contact angle (exceeding 160°) with a surface and has a low hysteresis of difference in advancing and receding angles of droplets. At the other extreme, superhydrophilicity shows very low wetting angles-near zero, and the presence of water film on surfaces. These properties can be achieved by forming multi-scale roughness of micro/
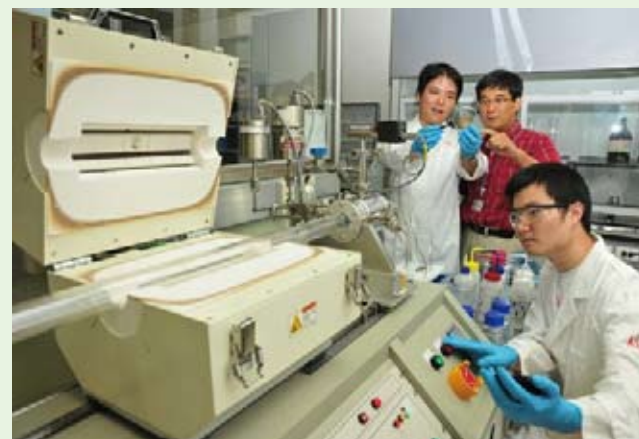
nano-scales and applying material coatings with specific energy characteristics on various materials or structures like metals or semiconductors, or curved or textile woven/non-woven structures. In the latest research studies, by controlling or tuning surface energy on nanostructured or hierarchically-structured surfaces, wettability can be easily contrasted or patterned on hydrophobic/hydrophilic surface domains by mimicking the back of the Namib beetle [1].

Recent research has been investigating how liquids act on these extremely hydrophobic/hydrophilic surfaces. In this context, our group has been focusing on understanding and controlling liquid behaviors on highly modified surfaces to obtain further insight on superhydrophobic and superhydrophilic surfaces. This article summarizes our efforts related to three important issues. First, we will describe how a superhydrophobic surface loses its properties in the condensation process when small liquid droplets grow directly on the surface (a superhydrophobic surface can only repel liquids from an out-source) [2]. Second, we will show that superhydrophilicity does not last a long time due to high surface energy [3,4]. Third, we will demonstrate the complexity of predicting the spreading behavior of liquid on a superhydrophilic surface because spreading phenomena include imbibition layers [4,5].
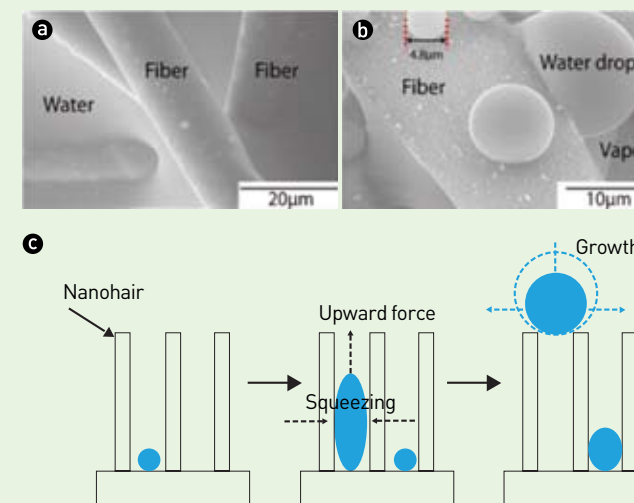

FIGURE 1 ESEM images of the condensation behavior of water vapor on (a) superhydrophilic NWF and (b) superhydrophobic NWF. The vapor pressure in the chamber was 6.6 and 6.2 Torr in (a) and (b), respectively. (c) Schematic of water repulsion behavior of a flat substrate with high aspect-ratio and hydrophobic nanohairs with small spaced intervals [2].
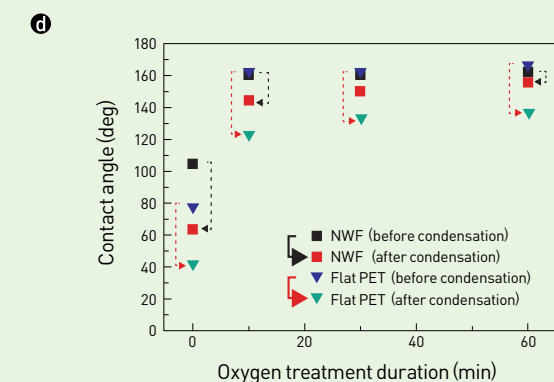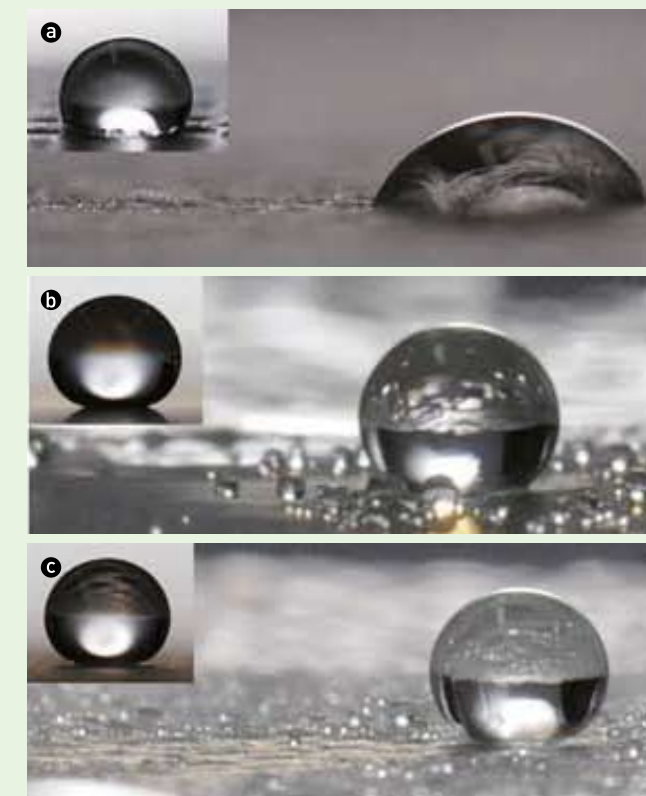
FIGURE 2 The images of sessile water drops on (a) pristine NWF, (b) flat superhydrophobic PET, and (c) superhydrophobic NWF, all of which have gone through vapor condensation on their surfaces. The insets of each figure show the water drops deposited on dry surfaces. (d) The contact angle of water drops on the superhydrophobic NWF and the flat superhydrophobic PET substrates before and after condensation of water vapor versus the oxygen plasma treatment duration [2].

As−modified films

60~80°

← 10°

Wetting angle after exposure to ambient air
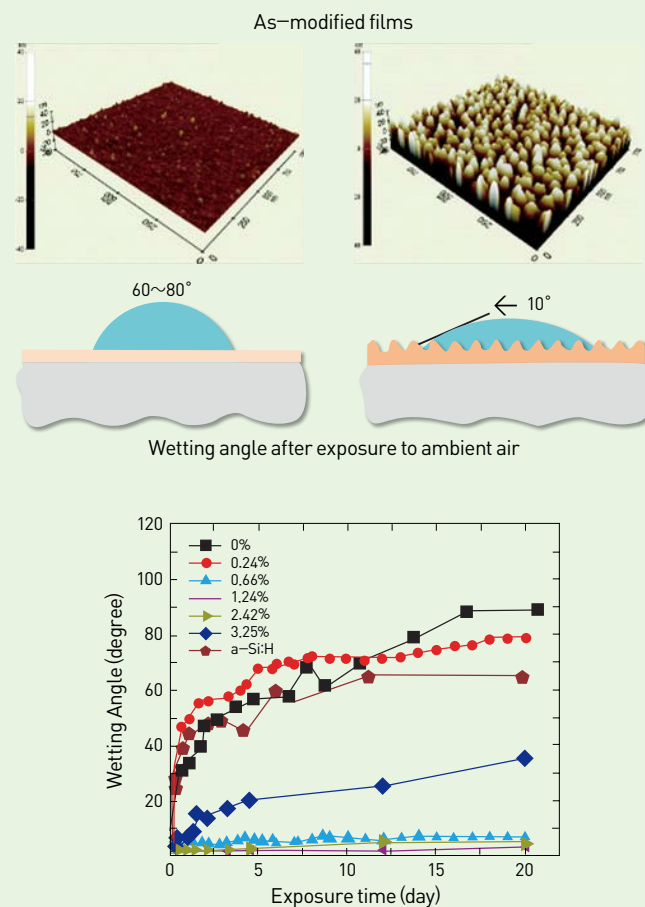
FIGURE 3 Wetting angles on flat and rough surfaces on Si-DLCs (left) and wetting aging measured on Si-DLCs with various Si content versus exposure duration (right) [3]
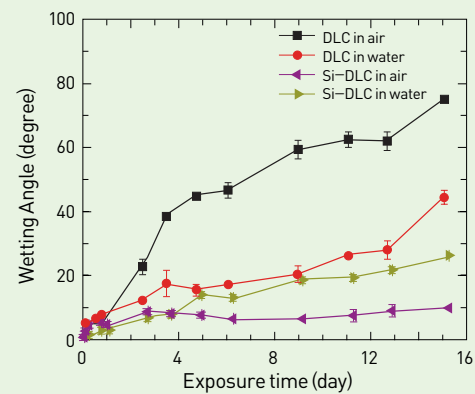

FIGURE 4 Contact angle behaviors of the oxygen-plasma-treated pure DLCand Si-DLC films with 1.24% of Si as a function of exposure time in ambient air and immersion time in DI water [3]

Durable superhydrophobicity for the condensation process

As mentioned above, a superhydrophobic surface easily suffers from compromised performance during the condensation process. Liquid condensed on the surface forms a thin liquid layer. Therefore, when a drop of liquid is deposited on a condensed surface, it is similar to the situation in which a drop of liquid is deposited on a pre-wetted surface. Unfortunately, we do not have any technique to obstruct the growth of liquid on a surface during the condensation process in air with high humidity. However, as an alternative, we have suggested a method to repel a liquid drop condensed on a surface, as shown in Figure 1 [2]. In this method, when a liquid drop grows to a specific size, it is expelled from a nano-pillar array because the gap size between nano-pillars is narrower than the volume of the drop which is then forced out as shown in Figure 1c. To demonstrate this concept, we fabricated a nano-pillar array with a high-aspect ratio using oxygen plasma etching on polymer substrates of flat surface and fabric. Fabric structure is well-suited for practical uses because it has a micro-structure itself. In this experiment, we used a non-woven fabric (NWF) structure as a fabric. We fabricated a nanostructured superhydrophobic PET fabric with a hierarchical structure of micro- and nano-morphologies. As indicated in Figure 2 [2], the nano-structured flat surface and fabric showed small decreases of contact angle after the condensation process and revealed robust superhydrophobicity. By contrast, specimens without a nano-pillar array showed large decreases of contact angle.

Long-lasting superhydrophilic surfaces with nano-structure

A superhydrophilic surface refers to a surface which has high surface energy. Unfortunately, such a high surface energy is usually energetically unstable in the presence

ⓐ

t=0.003 s   t=0.011 s   t=0.021 s   t=0.033 s

ⓑ

t=0.03 s   t=0.08 s   t=0.33 s   t=0.75 s
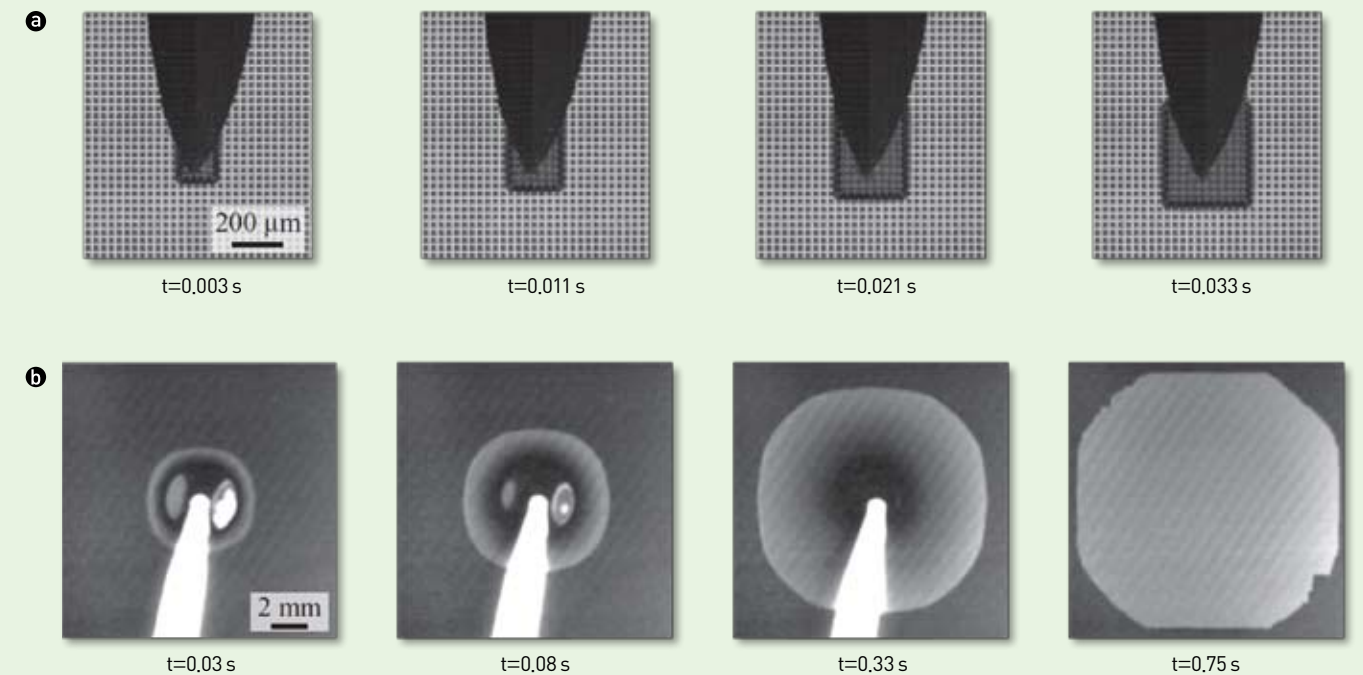
FIGURE 5 Comparison of the spreading behaviors of water films (a) in the absence of bulk and (b) driven by the bulk on identical micropillar arrays. In (a), a flexible needle tip keeps its conformal contact with the substrate resulting in a film flow, whereas in (b), the drop separates from the pipette at t =0 [4].

of air or water and leads over time to a decrease in superhydrophilicity because a chemical change occurs on the surface which reduces surface energy. Silicon dioxide is a well-known material having high hydrophilicity due to its higher surface energy and stable chemical structure. A glass surface consisting primarily of SiO_2 is known to have a low contact angle for water, less than 10 °. However, the high hydrophilicity of glass also easily disappears with time due to contamination from the air. Hydrocarbon from air easily adheres to a surface having high surface energy. To solve this time-dependent wettability aging, we fabricated a thin film coating having nano-scale roughness (we will not designate it as a pillar due to its low aspect ratio) on a SiO_2-rich surface [3]. The thin film consisted of amorphous carbon and SiO_2, and the surface of the film consisted mainly of SiO_2 deposited by oxygen plasma treatment

on Si-DLC (Si-incorporated carbon film) (see Figure 3). Results showed that chemical structure didn't change and hydrophilicity was sustained with a very low contact angle (less than 10 °) on the nano-scaled roughened surface during 20 days of exposure to air. It is believed that nano-scale roughness does play a role in preventing chemical changes from air contamination. Figure 4 indicates the variation of contact angle after oxygen plasma treatment on DLC (not forming SiO_2) and Si-DLC (forming SiO_2) in both air and water environments. The contact angle increased easily on the DLC surface given time in both air and water, whereas the contact angle remained very low on Si-DLC exposed to air. In the case of water immersion however, Si-DLC showed an increase of contact angle. These different results for air and water exposure are considered to originate from different contamination mechanisms.

Developing long-lasting properties inside a water environment remains a subject of further study for us.

Complex spreading behaviors on superhydrophilic surfaces

In the previous section, we only considered the static contact angle on superhydrophilic surfaces. However, it is also important to increase the spreading speed of a liquid to rapidly reach a liquid film state, not a lens state, on the superhydrophilic surface. A liquid film state is useful for real applications like dehumidifying plate and anti-fogging. However, spreading behavior on superhydrophilic surfaces is different from a traditional spreading model and complex because it accompanies an imbibition layer, which means that there are two different spreading parts as shown in Figure 5 [4,5]. To understand the spreading of a fringe layer (imbibition part), we performed an experiment designed to eliminate the bulk part by directly pushing a micropipette or syringe tip on the surface as indicated in Figure 5a. In this case, rectangular spreading occurred because spreading in the zipping direction (the normal direction for the entire spreading process) is energetically more favorable than the case of advancing direction (the entire spreading direction) for the regular pillar array. However, when there is internal pressure to push the fringe layer in the advancing direction, like bulk flow, circular spreading occurs even though the zipping direction is energetically favorable. Such circular spreading lasts until the driving pressure of the bulk flow is stronger than the driving pressure of the fringe layer. In other words, a liquid spreads in a circular shape during the initial stage. However, the spreading shape may change into that of a rectangle due to the effect of the fringe layer. Figure 5b shows a spreading shape that was converted from a circle to octagon. Moreover, because the spreading behavior was dominated by the bulk flow, not by the fringe layer, the kinetics of the total spreading also followed the kinetics of bulk flow. Both spreading behaviors followed the scaling law of $\sim(\gamma a^3 t/\mu)^{1/4}$. This scaling law was obtained from the concept that bulk spreads on the pre-wetted surface from the fringe layer [4].

Conclusion

Recently, researchers have focused on developing methods to fabricate superhydrophobic and superhydrophilic surfaces. Although such efforts have been successful in fabricating these surfaces by cheap, easy and clean methods, many issues remain which stand in the way of making these methods feasible for real applications. To solve such problems, we need to understand and control the behavior of liquid on these surfaces. In our research described above, we considered three different issues and provided our results and insights related to how liquid acts on different surfaces. Tuning nano-structure on superhydrophobic and superhydrophilic surfaces resulted in the development of durable superhydrophobic surfaces for the condensation process and long-lasting superhydrophilic surfaces for wettability aging in the air. Additionally, we analyzed the complex spreading behavior associated with the fringe layer on superhydrophilic surfaces and found that it is the first step to understanding the interactions between the bulk and fringe layers in controlling the spreading of a liquid drop on a super-hydrophilic surface.

References

[1] Parker AR, Lawrence CR. Nature. 2001; 414: 33-34.

[2] Shin B, Lee K-R, Moon M-W, Kim H-Y. Soft Matter. 2012; 8: 1817.

[3] Yi JW, Moon M-W, Ahmed SF, Kim H, Cha T-G, Kim H-Y, Kim S-S, Lee K-R. Langmuir. 2010; 26(22): 17203-17209.

[4] Kim SJ, Moon M-W, Lee K-R, Lee D-Y, Chang YS, Kim H-Y. J Fluid Mech. 2011; 680: 477-487.

[5] Kim J, Moon M-W, Lee K-R, Mahadevan L, Kim H-Y. Phys Rev Lett. 2011; 101: 264501.

Electric Actuation of Nanostructured Thermoplastic Elastomer Gels with Ultralarge Electrostriction Coefficient

Chong Min Koo
Center for materials architecturing
● koo@kist.re.kr

Introduction

Electrostrictive dielectric elastomers have garnered attention as promising candidates for next-generation compact actuators, sensors, artificial muscles and micro-robots, owing to their attractive properties such as large electromechanical strain [1-4], fast response [4], high power to mass ratio [5-6], facile proccessibility, and affordability. However, dielectric elastomers demonstrate large actuation only at high electric fields (above 50 V/μm), a factor which significantly impedes their use for real applications.

When an electric field is applied across film thickness, a film of electrostrictive materials is compressed in the longitudinal direction and spreads in the lateral planar direction. Unlike piezoelectricity, which has a linear relationship with an applied field, this electrostriction behavior demonstrates that the total thickness strain, s_z, has a quadratic relationship with the applied electric field (E), as delineated by the following equation.

$$s_z = R_{33}E^2,$$ (1)

where R_{33} represents the sensitivity of the strain response of a material to the applied electric field.

In general, the electric actuation of dielectric elas-tomers is driven by the two mechanisms of Maxwell stress and a true electrostrictive effect, as illustrated in Figure 1 [7, 8]. The electrostriction of a dielectric elastomer is usually dominated by Maxwell stress, which is caused by the Coulomb interaction between oppositely charged compliant electrodes, expressed as (Equation 2).

$$s_M = R_M E^2 = -\frac{\varepsilon_0 K}{2Y}E^2$$ (2)

where R_M is the Maxwell stress contribution for R_{33}, and Y is the compressive modulus. K and ε_0 are the dielectric constant and the vacuum dielectric permittivity, respectively. A higher dielectric constant can lead to stronger electrostatic charge accumulation. Meanwhile, the true electrostrictive effect that originates from direct coupling between the polarization and mechanical response generally constitutes a minor contribution to the electrostriction of a dielectric elastomer. For a linear dielectric, the strain is induced by a change in the polarization level in the material, as expressed in (Equation 3)

$$s_{ES} = R_{ES}E^2 = QP^2 = Q\varepsilon_0^2(K-1)^2E^2$$ (3)

where R_{ES} is the true electrostriction contribution for R_{33}, and P and Q are the polarization and the electrostrictive coefficient of the material, respectively. Here Q is the material-related parameter that determines the true electrostrictive strain to a given polarization.

To date, endeavors to reduce the operational electric fields of the dielectric elastomers have mainly focused on enhancing the dielectric constant of a dielectric elastomer itself or dispersing high dielectric fillers to improve the Maxwell stress effect [5, 6, 9]. However, for these composite approaches, it is difficult to control the dispersibility of fillers in the matrix, and, moreover, side effects such as increased dielectric loss and decreased break-down voltage arise [9]. Unfortunately, the true electrostriction effect is rarely taken into careful consideration in the electric actuation of dielectric elastomers.
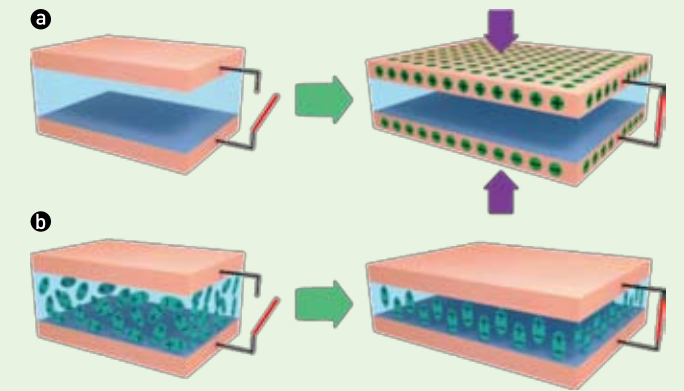

FIGURE 1 Schematic illustrations of two electric actuation mechanisms of a dielectric elastomer. (a) Maxwell stress that originates from the Coulomb interaction between oppositely charged compliant electrodes. (b) A true electrostrictive effect that originates from direct coupling between the polarization and mechanical response.

In this work, we demonstrate that the introduction of periodic nanoscale interfaces to dielectric elastomer gels lead to an unexpected high true electrostriction effect, resulting in a large electromechanical strain response at a relatively low electric field. A triblock copolymer, poly (styrene-*b*-ethylbutylene-*b*-styrene)-*graft*-maleic anhydride (MA) or poly (styrene-*b*-ethylbutylene-*b*-styrene) (SEBS) gel, plasticized by a mineral oil was employed as a thermoplastic elastomer gel.

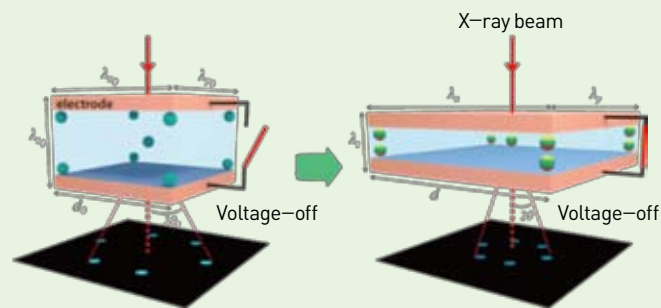## Nanostructured Thermoplastic Elastomers

Mechanical and dielectric properties and inter-domain spacings of the thermoplastic elastomer gels used in this work are listed in Table 1. For a typical sample name, e.g. MA20 gel, the number denotes the block copolymer content in the oil-swollen gel. The polymer content was varied from 20 to 40 wt% in this study. All the as-prepared SEBS and MA gels had a micellar network morphology at room temperature, as shown in Figure 2. The average diameter of the micelles was around 18 nm. The average domain spacing (d_0) of SEBS and MA gels are listed in Table 1.
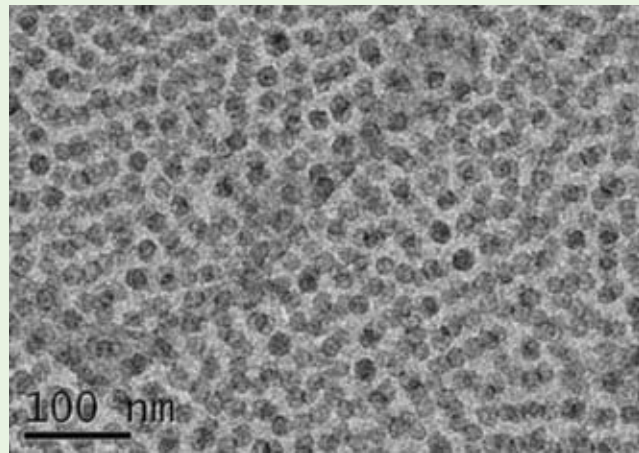
FIGURE 2 TEM image of the SEBS20 nanostructured thermoplastic elastomer

Measurement of Electric Actuation Strain

The true electric actuation strain of a nanostructured thermoplastic elastomer gel can be evaluated from the nanostructure dimension change measured via in-situ synchrotron SAXS during electromechanical actuation, as described in Figure 3. Generally, thermoplastic elastomers with a soft nature are known to satisfy affine deformation, that is, the microstructure dimension in a sample deforms in the same manner as the bulk dimension does [10]. If a material follows incompressible and isotropic radial planar

FIGURE 3 A schematic diagram of in-situ synchrotron SAXS measurement of thermoplastic elastomer gels during electromechanical actuation

extension, the thickness strain can be evaluated on the basis of microstructure dimension change according to (Equation 5).

$$V = \pi \lambda_{x0} \lambda_{y0} \lambda_{z0} = \pi \lambda_x \lambda_y \lambda_z \qquad (4)$$

$$s_z = \frac{\lambda_z}{\lambda_{z0}} - 1 = \frac{\lambda_{x0} \lambda_{y0}}{\lambda_x \lambda_y} - 1 = \frac{1}{\left(\frac{\lambda_x}{\lambda_{x0}}\right)^2} - 1 \approx \frac{1}{\left(\frac{d}{d_0}\right)^2} - 1 \qquad (5)$$

where λ is the bulk dimension at each direction, and d is the mean domain spacing of the nanostructured material. Figure 4 shows the variation of the reflection peak position of a representative thermoplastic elastomer sample with the applied field strength. The reflection peak shifted to a lower q, as the electric field increased. Domain spacing d was calculated by Bragg's law ($d = \frac{2\pi}{q} = \frac{n\lambda}{2\sin\theta}$). This equation provides an accurate strain evaluation that excludes the influence of flexure motion of the sample.

Electric Actuation of Nanostructured Thermoplastic Elastomers

Figure 5a shows the variation of d/d_0 of the SEBS and MA gels with various compositions of the triblock copolymer as a function of the applied electric field. As the polymer
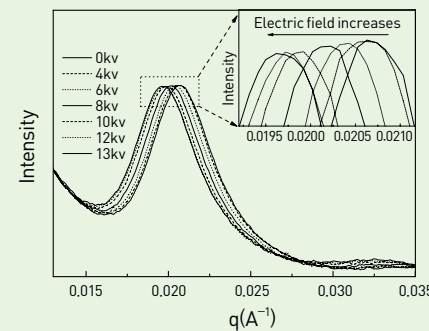

FIGURE 4 1D SAXS patterns of SEBS20 as a function of the applied electric field strength. Inset magnifies the selected area.
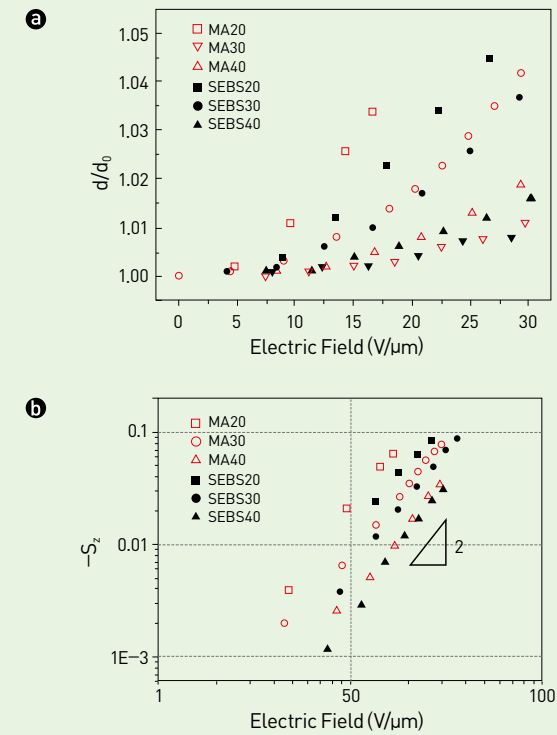
FIGURE 5 (a) Variation of normalized domain spacing for SEBS and MA gels at various polymer contents (in wt%). (b) The thickness strain of the SEBS and MA gels at various polymer contents (in wt%).

content was decreased, d/d_0 increased more rapidly with the applied field. This is due to the low compressive modulus of a gel with low polymer content. However, the MA gel showed a higher increase in d/d_0 than the SEBS gel at the same polymer content and the same electric field. As shown in Figure 5b, the thickness strains of the SEBS and MA gels, evaluated by (Equation 5), were proportional to the square of the electric field. This verifies that the SEBS and MA gels actuate according to an electrostrictive mechanism described by (Equation 1). As the polymer content was decreased, the strain increased more rapidly with the applied electric field. The MA gel had a higher strain than the SEBS gel at the same polymer content and the same electric field level. To our knowledge, the thickness strain value measured by the synchrotron SAXS
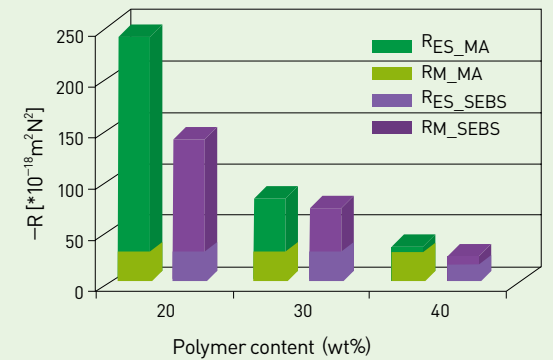
FIGURE 6 Comparison between Maxwell stress contribution, R_M and true electrostriction contribution, R_{ES}, of SEBS and MA gels to the strain sensitivity, R_{33} at 15 V/μm. R_{33} represents the sum of R_M and R_{ES}.

is the closest to the true strain ever measured in the field of dielectric elastomer studies, because the nanostructure dimensional change depends on the thickness dimension change, not on the translational movement like the bending motion, while the conventional laser sensing method is likely to overestimate the thickness strain due to the bending movement of the dielectric elastomer [11].

Figure 6 presents a comparison between the measured R_{33} and the contribution from the Maxwell stress effect, R_M at 15 V/μm. The sensitivity of the strain, R_{33}, and the contribution from the Maxwell stress effect, R_M, could be calculated by (Equation 1) and (Equation 2), respectively, as the field induced strain is proportional to the square of the applied electric field. The contribution from the electrostrictive effect, R_{ES}, can be simply obtained by R_{33}-R_M. Both $-R_{33}$ and $-R_M$ increased with a decrease in the polymer content. However, as the polymer content was decreased, $-R_{33}$ increased more rapidly than $-R_M$. This indicates that the true electrostriction contribution, R_{ES}, became more significant in the electrostriction behavior of the thermoplastic elastomer gel with lower polymer content. In addition, the MA gel showed a higher true
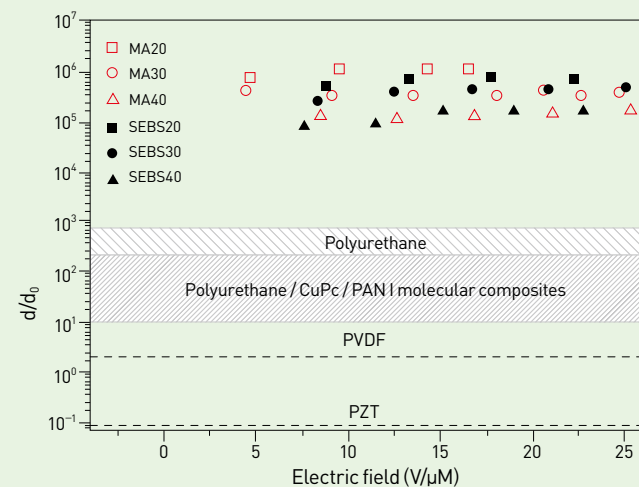
FIGURE 7 The electrostrictive coefficient, Q, of the SEBS and MA gels as a function of the applied electric field. The Q values of several ferroelectric materials and dielectric materials are included as references.

electrostriction contribution than the SEBS gel, particularly at low polymer content.

Figure 7 shows the true electrostrictive coefficients, Q, of the SEBS and MA gels at various polymer contents, obtained using (Equation 3). Both the SEBS and MA gels had ultralarge Q values, compared with those of conventional ferroelectric materials such as inorganic PZT and organic PVDF, and even compared with a polyurethane dielectric elastomer, a fluoroelastomer, and a polyurethane-based molecular composite with highly improved dielectric permittivity, as listed in Table 2 [5]. The Q value increased as the polymer content in the gel decreased. The MA gel showed a larger Q than the SEBS gel at the same polymer content. We note that MA20 demonstrated the largest Q value ($\sim 1.1 \times 10^6$ m^4/C^2) reported to date.

This strong true electrostriction effect could be attributed to the high density of interfaces between dielectric mismatched periodic domains, which results in the development of an inhomogeneous electric field across

the film thickness. The nonuniform field distribution can enhance the strain response, given that coupling between the strain and electric field in a dielectric elastomer is described by a quadratic relationship, delineated by Equation 2 and Equation 3 [2, 5, 6].

Conclusions

The electromechanical actuation of nanostructured SEBS and MA gels have been investigated via in-situ synchrotron SAXS measurements. The well defined nanostructures of the thermoplastic gels make it possible not only to measure the true thickness strains free from any flexural deformation effect, but also to monitor the directional dependence of the dimension change of the nanostructured thermoplastic elastomer single crystal in nanoscale order. The nanostructured gels had ultralarge true electrostrictive coefficients that became even larger as the gel became softer. Such unique behavior stemmed from the presence of a high density of nanoscale multidomain structures, which built up inhomogeneous electric fields in the gels. In this work, the introduction of a dielectric mismatched nanostructure to a dielectric elastomer is suggested as a valuable pathway to enhance the electromechanical strain response of a dielectric elastomer.

Note

References

[1] Pelrine R, Kornbluh R, Pei Q, Joseph J. Science. 2000; 287: 836.
[2] Shankar R, Ghosh TK, Spontak RJ. Adv Mater. 2007; 19: 2218.
[3] Shankar R, Krishnan AK, Ghosh TK, Spontak RJ. Macromolecules. 2008; 41: 6100.
[4] Shankar R, Ghosh TK, Spontak RJ. Soft Matter. 2007; 3: 1116.
[5] Huang C, Zhang QM. Adv Mater. 2005; 17: 1153.
[6] Zhang QM, Li H, Poh M, Xia F, Cheng ZY, Xu H, Huang C. Nature. 2002; 419: 284.
[7] Guiffard B, Seveyrat L, Sebald G, Guyomar D. J Phys D: Appl Phys. 2006; 39: 3053.
[8] Li JY, Rao N. Appl Phys Lett. 2002; 81: 1860.
[9] Shankar R, Ghosh TK, Spontak RJ. Macromol Rapid Commun. 2007; 28: 1142.
[10] Koo CM, Hillmyer MA, Bates FS. Macromolecules. 2006; 39: 667.
[11] Kim B, Park YD, Kim J, Hong SM, Koo CM. J Polym Sci Part B: Polym Phys. 2010; 48: 2392.
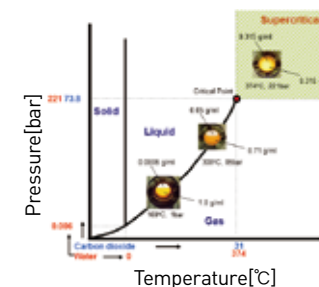
Supercritical Fluid Technology: A Green Chemical Process for the 21st Century

Jae Hoon Kim
Clean Energy Research Center
• jaehoonkim@kist.re.kr

As we move forward into this new century, we must consider the environmental ramifications of the hazardous waste generated by various chemical processes. Many toxic solvents, such as methylene chloride and hexane, have been widely used for chemical and material synthesis. Most solvents used in industry are considered to be volatile organic compounds (VOCs) and their use has been controlled to reduce air pollution. Supercritical fluids are an attractive alternative to the traditional organic solvents because they can be easily recycled and they provide ease of product separation. A supercritical fluid is the state of matter in which a compound is subjected to conditions above its critical pressure and critical temperature but at a pressure low enough to prevent the solid from forming (Figure 1). Carbon dioxide and water, which are nontoxic, inert, cheap and readily available, are the most widely used supercritical fluids.

In addition to their environmental benignity, the unique physical properties of supercritical fluids, including extremely low surface tension, low viscosity, and tunable density, make them an appropriate medium for overcoming some of the constraints associated with traditional chemical processes. For example, the zero surface tension of supercritical fluids makes them excellent wetting agents even on very low-surface-energy substrates. In addition, the zero surface tension is advantageous in preventing capillary collapse of sol-gels and high-aspect-ratio structures and during drying,
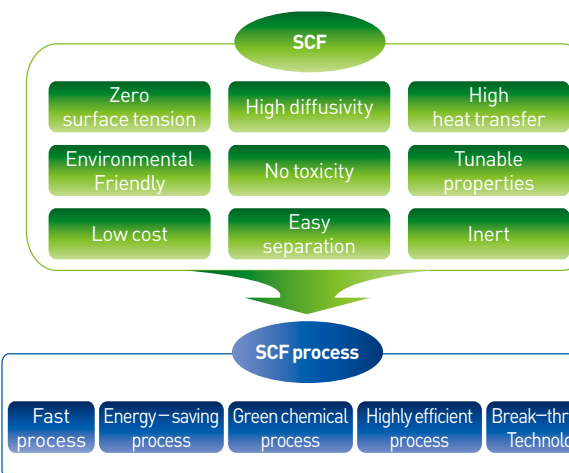
and in allowing easy penetration into small features or patterned surfaces (e.g., microelectronics microelectromechanical systems). Low viscosity of supercritical fluids can enhance reaction rates in typical diffusion-limited chemical reactions. The ability to tune the physical properties of supercritical fluids by changing process variables such as temperature and pressure can provide a very high degree of control over the evaporation or drying process. Moreover, the high vapor pressure and high diffusivity of supercritical fluids ensures that there will be no residual solvent left in the products. Herein, the use of supercritical fluids in various areas of next-generation energy production and energy materials will be discussed.

Nanomaterials synthesis in supercritical fluids for energy storage applications

Synthesis of nanomaterials in supercritical fluids is a very promising technique to produce nano-sized particles with highly crystalline structures. The beneficial properties of supercritical water and supercritical alcohols, such as high diffusivity of reactants in the supercritical medium, fast reaction rate, high degree of supersaturation, and lower dielectric constant, can result in high quality, ultrafine nanoparticles at a high rate (less than 1 min). In addition, supercritical hydrothermal synthesis is an environmentally benign method and readily scalable when running in a continuous mode. Figure 3 shows various types of nanomaterials that have been synthesized in supercritical water and supercritical alcohols. This includes NiO, ZnO, MnO_2, Fe_3O_4, CeO_2, $LiFePO_4$, and $Li_4Ti_5O_{12}$. Among theses, $LiFePO_4$ and $LiTi_5O_{12}$ are

potential candidates for cathode and anode materials in large-scale 2nd generation lithium batteries such as those used in plug-in hybrid electric vehicles (PHEV) and backup power systems.

As shown in Figure 4, nanosized $Li_4Ti_5O_{12}$ particles of quasi-sphere shape having a size of 20–50 nm were synthesized in supercritical water. In contrast, much larger micron-sized particles with a heavy degree of aggregation between neighboring particles were produced when the conventional solid-state method was used.

FIGURE 3 Nanomaterials synthesized in supercritical water and supercritical alcohols [1-12]
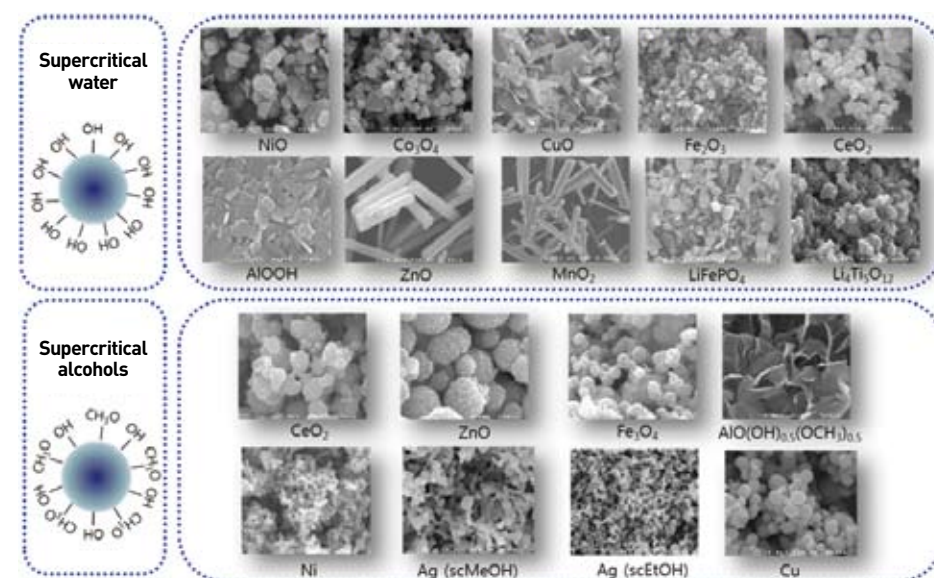
Thus, low synthetic temperature and low calcination temperature associated with supercritical water process can result in high-surface-area $Li_4Ti_5O_{12}$ particles with a small degree of aggregation. When supercritical alcohol was used, $Li_4Ti_5O_{12}$ particles with unique mesoporous nano/micro morphology were synthesized. The primary $Li_4Ti_5O_{12}$ nanoparticles were slightly agglomerated and formed micron-sized spherical particles by e.g. interparticle interactions, leaving empty space among the nanoparticles, resulting in hierarchically mesoporous microsphere morphology.

The obtained $Li_4Ti_5O_{12}$ synthesized in supercritical water and supercritical methanol show excellent rate performance. The samples were progressively charged and discharged at 17.5 mA g^{-1} (0.1 C), 175 mA g^{-1} (1 C), 350 mA g^{-1} (2 C), 700 mA g^{-1} (4 C), 1,400 mA g^{-1} (8 C), 1,750 mA g^{-1} (10 C), and 3,500 mA g^{-1} (20 C), as shown in Figure 4. The $Li_4Ti_5O_{12}$ particles synthesized in supercritical water exhibit much higher specific capacity compared to the $Li_4Ti_5O_{12}$ particles synthesized by the solid-state method.

Large-size particles and interparticle aggregation are responsible for the low capacity and the poor capacity retention of the solid-state synthesized particles. The $Li_4Ti_5O_{12}$ particles synthesized in supercritical methanol exhibit much higher specific discharge capacity at current rates up to 20 C than those of the $Li_4Ti_5O_{12}$ particles synthesized by solid-state method. The capacity was 155.6 mAh g^{-1} at 4 C and 79.7 mAh g^{-1} at 20 C. These values are significantly higher than those of the micrometer-sized $Li_4Ti_5O_{12}$ synthesized by the solid-state method (96.5 mAh g^{-1} at 4 C and 25.8 mAh g^{-1} at 20 C). When compared to the nano-sized $Li_4Ti_5O_{12}$ prepared in supercritical water, the mesoporous $Li_4Ti_5O_{12}$ showed much better performance at the rate regime up to 8 C. The better rate performance of the $Li_4Ti_5O_{12}$ synthesized in supercritical methanol can be due to the mesoporous channels allowing the electrolytes to penetrate inside of the structure, resulting in much higher interfacial contact with nano-sized LTO building blocks and better accessibility of the active material.

Recently, we demonstrated that metal nanoparticles (Ni, Ag, and Cu) and low-oxidation-state metal oxide (Fe_3O_4) nanoparticles can be synthesized in supercritical alcohols utilizing the reducing effect inherent to the supercritical alcohols [13-15]. On the basis of our previous results, we reasoned that supercritical alcohols may act as a cheap, non-toxic reducing agent for effectively deoxygenating GO to graphene-like sheets. Typically highly deoxygenated grapheme oxide sheets that resemble graphene are produced as a colloidal suspension in water or other organic solvents using strong reducing agents such as hydrazine and dimethyl hydrazine. However, the use of highly toxic and potentially explosive reducing reagents is not attractive in commercial-scale applications. Therefore, development of a facile, green, and fast method for the mass production of reduced graphene oxide (RGO) with a high carbon-to-oxygen ratio and high electronic conductivity remains a great challenge.

Figure 5 shows the use of supercritical alcohols for the synthesis of RGO nanosheets. The newly synthesized RGO nanosheets have high values of carbon-to-oxygen ratio and electrical conductivity of 11.89 and 10,600 S m^{-1}, respectively.

Solid-state

Supercritical Water

Supercritical Methanol
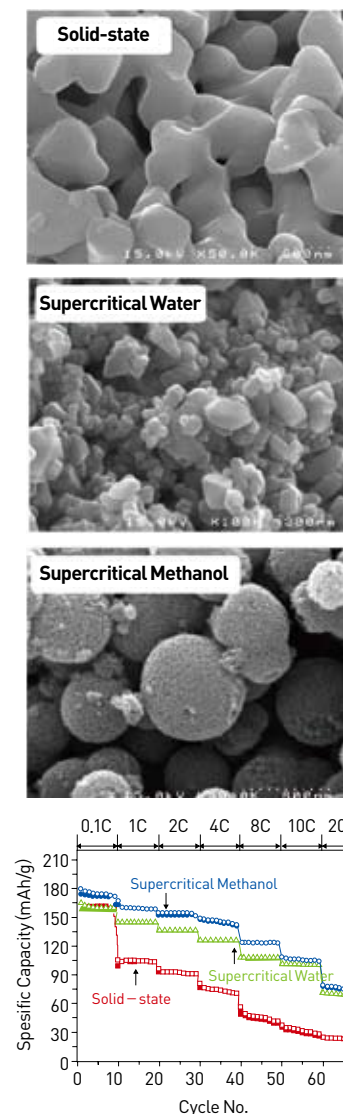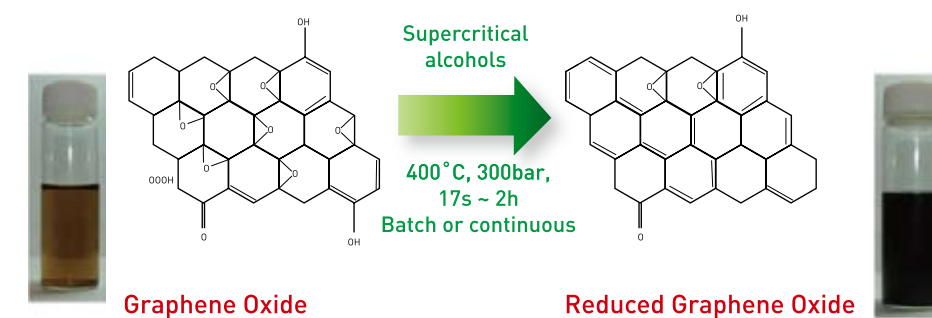
FIGURE 4 Morphology and electrochemical performance comparison of $Li_4Ti_5O_{12}$ synthesized using solid-state, supercritical water, and supercritical methanol methods

Supercritical alcohols

400°C, 300bar, 17s ~ 2h
Batch or continuous

Graphene Oxide   Reduced Graphene Oxide

FIGURE 5 Synthesis of reduced graphene oxide in supercritical methanol
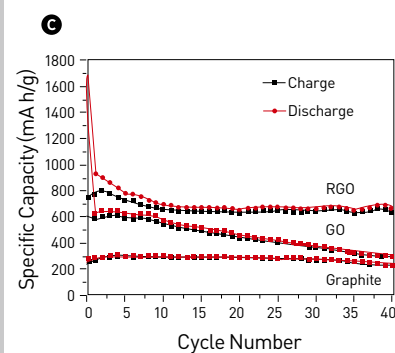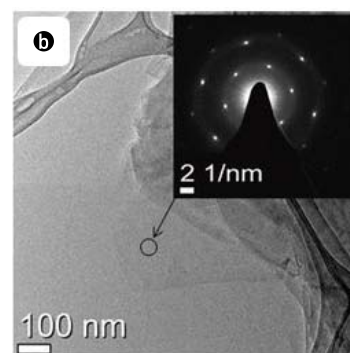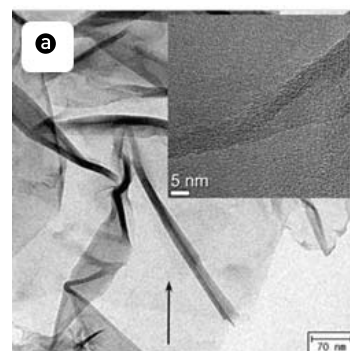
FIGURE 6 RGO synthesized in supercritical methanol and its cycling performance

These values are comparable to those of the hydrazine-based methods. Indeed, high reduction power and extremely fast reaction rate in supercritical alcohol suggest that the RGO nanosheets are capable of effectively removing the oxygen-containing functional groups to produce individual graphene sheets. Furthermore, supercritical alcohols act as a 'green' alternative to other toxic reducing agents [16].

Figure 6 shows TEM images of the RGO synthesized in supercritical methanol. Most of the RGO sheets aggregated to form thick graphene flakes with sizes ranging from 50 nm-2 μm. There are some corrugations and scrollings in the graphene stacks resulting in a curled morphology. As shown in Figure 6a (inset), single graphene nanosheets also tend to scroll at the edge, which is an intrinsic characteristic of graphene nanosheets. On the periphery of these stacks, single sheets of graphene were frequently observed, as confirmed by selected area electron diffraction (SAED) patterns in Figure 6b (inset). The graphitic crystalline structure with a hexagonal symmetry was clearly observed, indicating successful restoration of graphite structure in the RGO sample.

The electrochemical performance of the prepared RGO was examined to evaluate its potential for use as an anode material in next generation lithium-ion batteries. Figure 6c shows cycling performance of the graphite, GO and RGO samples. The reversible capacity of graphite at the 40th cycle was 224 mAh g^{-1}. Different from the natural graphite, the GO and RGO exhibit large irreversible capacity decay during the first cycle, which may be due to the formation of a solid electrolyte interphase (SEI) layer by the reaction between oxygenated functional groups and the lithium ion. The first discharge capacities were 1450 mAh g^{-1} and 604 mAh g^{-1}, followed by the first charge capacities, which were 1673 mAh g^{-1} and 738 mAh g^{-1} for GO and for RGO, respectively. The cycling performance of RGO showed that the discharge capacity gradually decreased from 926 to 664 mAh g^{-1} following the first 15 cycles (except for the first large irreversible cycle) and displayed relatively stable cycling capacities from 660-652 mAh g^{-1} for the last 40 cycles. For the GO sample, however, the discharge capacity approached that of the graphite following 40 cycles. This clearly indicates that RGO retains a much higher discharge capacity and an excellent cycling performance compared to the pristine graphite and GO samples.
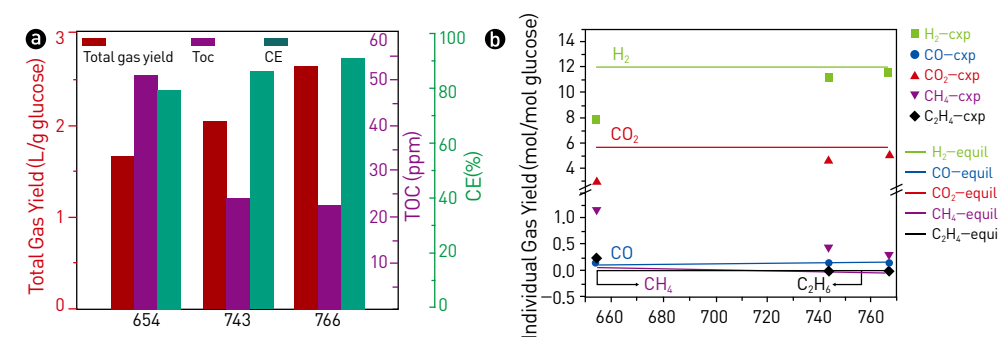
Hydrogen production in supercritical fluids

Hydrogen is considered as one of the most promising clean energy alternatives to fossil fuels due to the depletion of fossil fuels depletion and global warming. The production of hydrogen by supercritical water gasification (SCWG) (high-pressure steam reforming conducted above the critical point of water) has several advantages over conventional gasification techniques due to the unique physical properties of supercritical water. The low dielectric constant of supercritical water (2-20) allows a homogeneous phase reaction of various organic feedstocks in supercritical water. This can eliminate the mass transfer limitation that is inherent to multiple-phase reactions, and thus can increase the reaction rate. Supercritical water has extremely low viscosity, extremely high diffusivity, and adjustable density depending on the temperature and pressure, which is beneficial for fast reactions. High energy efficiency, environmental benignity, compact equipment, high hydrogen gas yield, feedstock flexibility, ability to handle high-water-content feedstocks (e.g., see Figure 8), and in-situ separation of CO_2 because of its high solubility at high pressure are some of the advantages of SCWG when compared to other conventional reforming methods. In addition, SCWG can be conducted in the absence of catalysts, avoiding challenges inherent to catalytic gasification such as catalyst deactivation due to the presence of heteroatoms (sulfur, nitrogen, phosphorus, etc) in some feedstocks, carbon deposition and reactor plugging issues [17-19].

FIGURE 7 Supercritical water gasification apparatus installed at KIST
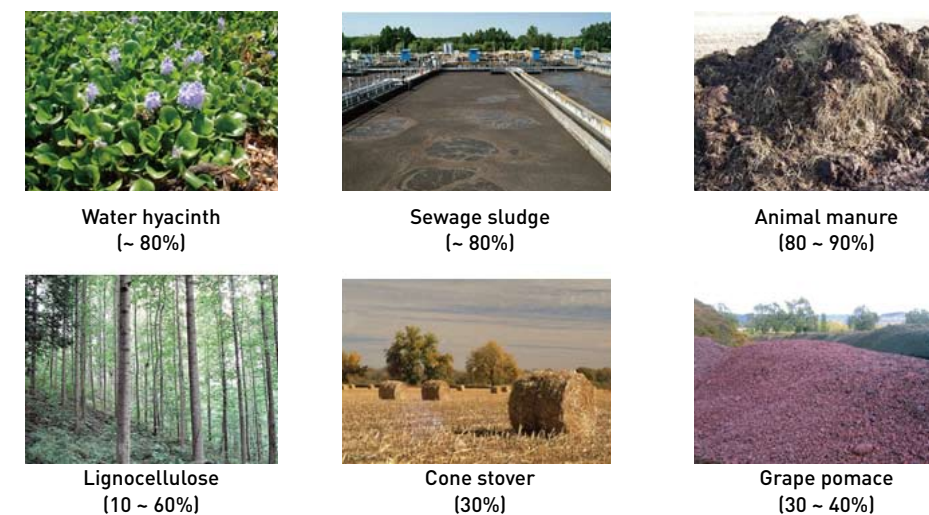
FIGURE 8 Possible feedstocks for supercritical water gasification. The percentages refer to water content in the feedstocks.

Water hyacinth (~ 80%)

Sewage sludge (~ 80%)

Animal manure (80 ~ 90%)

Lignocellulose (10 ~ 60%)

Cone stover (30%)

Grape pomace (30 ~ 40%)

FIGURE 9 The effect of temperature on (a) total gas yield, TOC and CE, and (b) individual gas yields, determined from the experiments and from equilibrium calculations.

The supercritical water gasification of glucose as a function of temperature at 25 MPa, 60 s and 1.8 wt% were carried out and the results are shown in Figure 9. As the temperature increased from 654 to 766℃, the total gas yield increased from 1.66 to 2.65 L/g glucose, carbon gasification efficiency (CE) increased from 79.5 to 91.0% and total organic compound (TOC) decreased from 51 to 23 ppm. The high CE values and the low TOC values indicate high conversion levels of glucose to gaseous products. The effect of temperature on the individual gas yields are shown in Figure 9b. Theoretically estimated gas yields are also shown for comparison with the experimental data. The gaseous products mainly consisted of H_2 (68.0-71.4 mol%) and CO_2 (24.8-29.4 mol%). Minor gas products include CH_4 (2.1-1.7 mol%), C_2H_6 (0.3-0.1 mol%) and CO (1.4-0.9 mol%). No other gases with carbon number equal to or higher than C3 was detected. The extremely low CO content observed in this study may be because the water-gas shift (WGS) reaction was enhanced significantly with the current reactor system. When the reaction temperature increased from 654 to 767℃, the experimentally-determined hydrogen gas yield increased from 7.91 to 11.5 mol/mol glucose. It is noteworthy that the current reactor system can produce almost the theoretical maximum hydrogen gas yield (12 mol/mol glucose) at temperatures higher than 740 ℃. Thus noncatalytic SCWG is a very promising method to produce hydrogen from renewable feedstocks.

In this feature article, we have described a range of strategies to synthesize nanomaterials in supercritical fluids for energy storage applications and to produce hydrogen from renewable sources. It is clear that there is a wide range of potential applications including separation, phamaceuticals, extraction, clean fuel production, biomass liquefaction, waste water treatment, and catalysis. A key conclusion is that supercritical fluid technologies provide a very flexible and clean route for novel nanomaterial synthesis and for developing new energy production processes.

References

[1] Veriansyah B, Susanti RF, Nugroho A, Min BK, Kim J. Mater Lett. 2011; 65: 772-774.

[2] Veriansyah B, Chun MS, Kim J. Chem Eng J. 2011; 168: 1346-1351.

[3] Nugroho A, Kim SJ, Chung KY, Cho BW, Lee YW, Kim J. Electrochem Commun. 2011; 13: 650-653.

[4] Jeon HS, Nugroho A, Kim J, Kim H, Min BK. Int J Hydrogen Energy. 2011; 36: 10587-10592.

[5] Hong SA, Nugroho A, Kim SJ, Kim J, Chung KY, Cho BW, Kang JW. Res Chem Intermediat. 2011; 37: 429-440.

[6] Hong SA, Kim SJ, Kim J, Chung KY, Cho BW, Kang JW. J Supercrit Fluids. 2011; 55: 1027-1037.

[7] Han NS, Shim HS, Seo JH, Park SM, Min BK, Kim J, Song JK. Chem Phys Lett. 2011; 505: 51-56.

[8] Veriansyah B, Kim JD, Min BK, Shin YH, Lee YW, Kim J. J Supercrit Fluids. 2010; 52: 76-83.

[9] Veriansyah B, Kim JD, Min BK, Kim J. Mater Lett. 2010; 64: 2197-2200.

[10] Shin NC, Lee YH, Shin YH, Kim J, Lee YW. Mater Chem Phys. 2010; 124: 140-144.

[11] Shin YH, Koo SM, Kim DS, Lee YH, Veriansyah B, Kim J, Lee YW. J Supercrit Fluids. 2009; 50: 250-256.

[12] Kim J, Park YS, Veriansyah B, Kim JD, Lee YW. Chem Mater. 2008; 20: 6301-6303.

[13] Kim J, Kim D, Veriansyah B, Kang JW, Kim J-D, Mater Lett. 2009; 63: 1880-1882.

[14] Choi H-M, Veriansyah B, Kim J-H, Kim J-D, Kang J-W. J Supercrit Fluids. 2010; 52: 285-291.

[15] Veriansyah B, Kim J-D, Min B-K, Kim J-H. Mater Lett. 2010; 64: 2197-2200.

[16] Nursanto EB, Nugroho A, Hong SA, Kim SJ, Chung KY, Kim J. Green Chem. 2011; 13: 2714-2718.

[17] Susanti RF, Nugroho A, Lee J, Kim Y, Kim J. Int J Hydrogen Energy. 2011; 36: 3895-3906.

[18] Susanti RF, Veriansyah B, Kim JD, Kim J, Lee YW. Int J Hydrogen Energy. 2010; 35: 1957-1970.

[19] Veriansyah B, Kim J, Kim JD, Lee YW. Int J Green Energy. 2008; 5: 322-333.

Development of Efficient and Stable Organic Solar Cells

Bong Su Kim
Photo-electronic Hybrids Research Center
• bongsoo@kist.re.kr

Introduction

Fossil fuels such as coal, oil and gas account for close to 80% of the energy supply worldwide. The transformation of these resources into usable energy in the forms of electricity and heat generates a massive amount of CO_2 gas. The CO_2 emission contributes significantly to the greenhouse effect. Moreover, the price of oil and gas is skyrocketing because reserves of these fossil fuels are decreasing while the demand for energy resources is increasing. Therefore, it is of great importance to find renewable energy resources. Biomass, hydropower, wind power, geothermal energy, and solar energy appear to be the most promising. Among them, harnessing solar energy is certainly one of the most viable, attractive approaches. The yearly energy demand of the entire world corresponds to the amount that the earth receives in an hour from the abundant, CO_2-free energy resource of the sun.[1] However, solar energy still provides less than 0.1% of the total energy supply.[2,3] With this great potential, the market for solar cells is growing rapidly and research to improve the efficiency and stability of solar cells has been conducted intensively.

Silicon-based photovoltaic (PV) cells have dominated the market for the past 50 years. However, thin-film PV technologies such as a-Si (amorphous silicon), CIGS (copper indium gallium diselenide), and CdTe (cadmium telluride) have rapidly improved their PV performance and production technologies. They already represented about 12.2% of overall PV production in 2010, and are expected to reach 20.7% by 2015.[2] Organic photovoltaic cells (OPVs) have recently attracted extensive research and development, because they can be applied to flexible, light-weight, low-cost, and large-area applications using cost-effective solution processing such as roll-to-roll. Power conversion efficiencies (PCEs) of OPV cells composed of poly(3-hexylthiophene)(P3HT) and [6,6]-phenyl-C61-butyric acid methyl ester (PCBM) were reported to be 4-5% previously. Recently OPVs incorporating low band gap polymers as electron donors have reached PCEs greater than 10%. Accelerating tests predict lifetimes greater than 6 years, and PCEs of OPV modules are in the range of 2-3%. Initial applications for OPVs include battery chargers for portable electronic devices. Integration of OPVs into functional devices such as OPV-enhanced lighting systems has also been demonstrated and tested for off-grid lighting applications in remote areas. However, widespread deployment of OPVs in large-area, rooftop applications for residential and commercial buildings would require higher module efficiencies (7–10%) and longer lifetimes (7–10 years).

To achieve these performance goals, KIST has been actively conducting research on OPVs for more than 6 years and has become one of the leading OPV labs in Korea. This article presents results achieved by KIST researchers in the synthesis of photoactive materials, development of device structure and interlayers, and improvement of long-term stability.

OPV cell structure and principle of operation

OPV cells are typically fabricated with one of two geometrical device structures, normal or inverted. Figure 1 illustrates device architectures and the energy level alignment in each OPV structure where interlayers present ideal contacts and carrier selectivity at electrodes. The normal cell is composed of an indium tin oxide (ITO) positive electrode, a hole extraction layer (HEL), a photoactive layer, an electron extraction layer (EEL), and a metal (e.g., Al, Ca) negative electrode, while the inverted cell consists of an ITO *negative* electrode, an EEL, an photoactive layer, an HEL, and a metal (e.g., Ag) *positive* electrode. The role of the transparent conducting oxide (TCO) here dictates the type of the device structure. The interlayers of HELs and EELs facilitate transport and collection of photo-generated holes and electrons, respectively (details are discussed below). The photoactive layer is a so-called bulk heterojunction (BHJ) type blend of electron-donating (p-type) and electron-accepting (n-type) organic materials
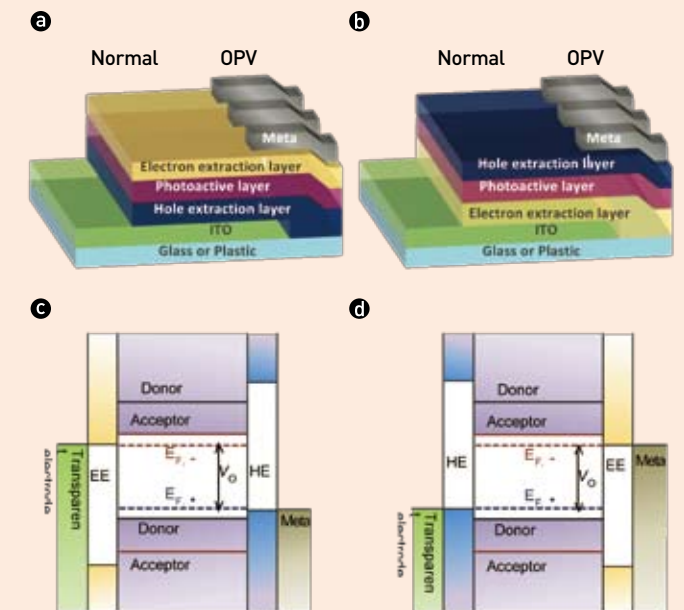
FIGURE 1 Device architecture of (a) normal and (b) inverted OPV structures. Illustration of the energy level alignment in (c) normal and (d) inverted OPV structures, where interlayers present ideal contacts and carrier selectivity at electrodes.
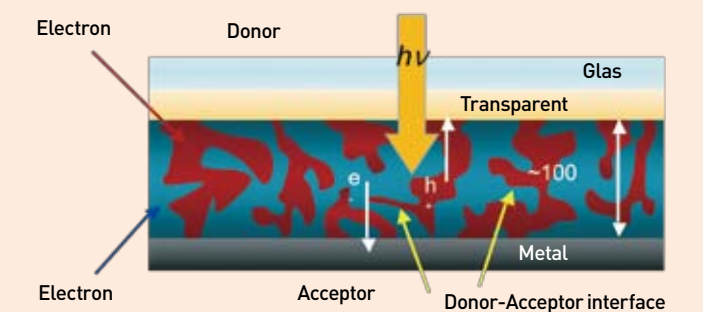
FIGURE 2 Schematic representation of a bulk heterojunction (BHJ) OPV cell, showing the phase separation between electron donor (*p-type*) and electron acceptor (*n-type*) materials.

(Figure 2). It is well known that the photoenergy conversion process goes through four fundamental steps: 1) light absorption by photoactive materials and then generation of Coulombically-bound hole-electron pairs, or excitons, 2) diffusion of excitons to the interface between p-type and n-type material, 3) dissociation of the excitons into free holes and electrons due to the energy difference between
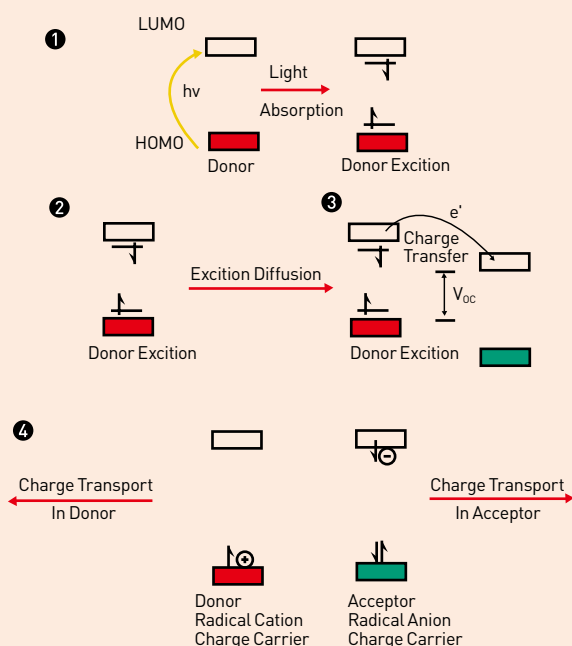
FIGURE 3 General mechanism for photoenergy conversion in OPV devices. Donor material is typically conjugated polymers/small molecules and acceptor is fullerene derivatives.
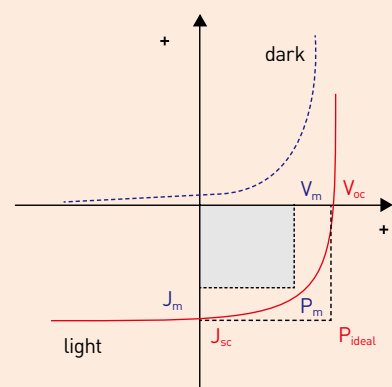
FIGURE 4 The typical current-voltage characteristics for dark and light current in an OPV cell illustrating the important parameters: J_{sc} is the short circuit current density, V_{oc} is the open circuit voltage, J_m and V_m are the current and voltage at the maximum power point, and FF is the fill factor. The power conversion efficiency (PCE) is defined as the ratio of output power (P_{out}) to input power (P_{in}).

donor's LUMO and acceptor's LUMO, and 4) free carrier transport and collection. Figure 3 illustrates each step with light absorption in the p-type donor material since donors have a high extinction coefficient. Of course, n-type acceptor materials participate in generating excitons, where hole transfer occurs in the step of exciton dissociation. Note that the BHJ blend has merit for use in OPV cells due to the exciton diffusion length of only about 10 nm. That is, the intimate contact of p-type and n-type materials induces high carrier generation. However, care must be taken because the probability of recombination of dissociated free carriers increases unless charge transporting channels are well connected to the electrodes.

Figure 3 illustrates typical current density-voltage curves for dark and light current in an OPV cell where J_{sc} is the short-circuit current density, V_{oc} is the open circuit voltage, J_m and V_m are the current and voltage at the maximum power point, and FF is the fill factor. The power conversion efficiency (PCE) is defined as the ratio of power out (P_{out}) to power in (P_{in}).

Development of new photoactive materials

The OPV team at KIST has been targeting several issues in order to fabricate highly-efficient, stable OPV cells. First, we have developed new low bandgap polymers and fullerene derivatives. Conjugated polymers have the advantage of offering high absorption coefficients for efficient light harvesting and exciton generation in thin films. In addition, composites of polymers and fullerenes form bicontinuous nanophase morphology for efficient charge separation and transport. For instance, the most investigated P3HT:PCBM system is able to harvest most of the photons of the solar spectrum from 400 nm to 675 nm and form nanoscale phase separation between P3HT and PCBM with domain sizes of 10–20 nm upon thermal or solvent annealing, resulting in
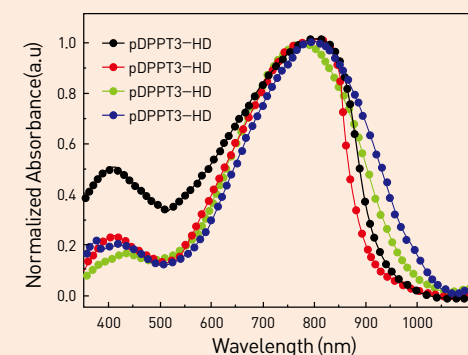

FIGURE 5 UV-visible spectra of low bandgap polymers

PCEs of 4–5%.[4,5] However, P3HT is not the ideal polymer as it has a relatively large bandgap (1.85 eV) and its high-lying highest occupied molecular orbital (HOMO) limits the V_{oc} of P3HT:PCBM devices.

To increase the light-harvesting abilities of polymers for improving BHJ device efficiencies, new low bandgap polymers with E_g down to ca. 1.4 eV have been synthesized. One successful approach to low bandgap materials involves the donor–acceptor copolymers, in which electron-rich units and electron-deficient moieties are integrated into a single conjugated polymeric system. For example, alternating copolymers containing carbazole-alt-benzothiadiazole,[6] bithiophene-alt-diketopyrrolopyrrole,[7] and benzo[1,2-b:4,5-b0]dithiophene-alt-thieno[3,4-b]thiophene units[8] have demonstrated efficiencies of 4–7% when paired with [6,6]-phenyl C71 butyric acid methyl ester in BHJ solar cells. Our team has synthesized several low bandgap polymers based on diketopyrrolopyrroles that are good acceptors. To date, we were able to achieve an exceptionally low bandgap of 1.2 eV (Figure 5), which value is nearly the limit of the optical bandgap for organic photovoltaics.

In addition, we have made efforts to develop fullerene derivatives having their lowest occupied molecular orbital (LUMO) high. The high-lying LUMO level of *n-type* materials is an important factor in increasing V_{oc}, because V_{oc} is proportional to the difference between the HOMO of a *p-type*
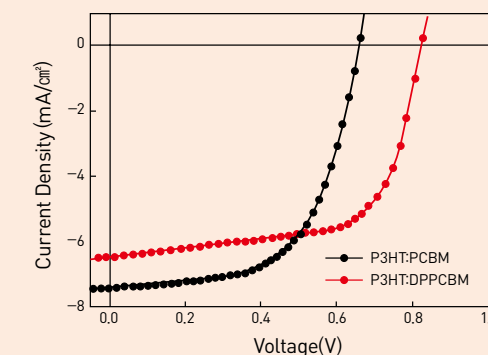

FIGURE 6 Current density-voltage curves of P3HT:PCBM and P3HT:bisadduct

material and the LUMO of a *n-type* material. In order to pose LUMO levels higher than PCBM's LUMO, we attached another pendant to PCBM forming a so-called bisadduct. This chemical modification induces a partial conjugation break in the PCBM molecules, thereby controlling molecular energy levels. In this strategy we were able to achieve a 0.84 V of V_{oc} in the P3HT:bisadduct system, which is considerably higher than the 0.66 V of V_{oc} in the P3HT:PCBM combination (Figure 6).

With these p-type and n-type materials in hand, we have fabricated OPV devices in various ways not only to improve PCEs but also to reduce production costs. For instance, to form bicontinuous p- and n-channels in the photoactive materials, a thermal annealing process has been used but it is not cost-effective. To eliminate the thermal process, we have developed a low-temperature process with a chemical additive such as 1,8-diiodooctane (DIO). With the addition of 3 vol % DIO to a processing solvent, P3HT:PCBM devices showed nearly equivalent cell efficiency of 3.5%. When we also applied the same strategy to a photoactive blend of low bandgap polymer and [6,6]-phenyl-C71-butyric acid methyl ester (PC70BM), we were able to obtain an efficiency of 7.3% using ITO/glass substrates (Figure 7). Moreover, we are fabricating OPV cells using flexible substrates. Since OPV cells are very thin, they are a good candidate for flexible, portable applications.
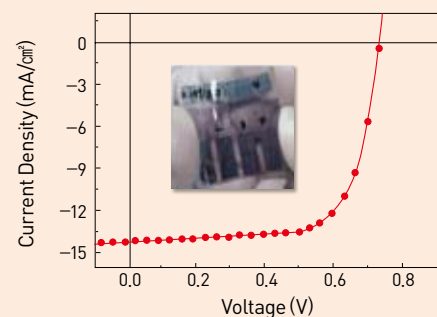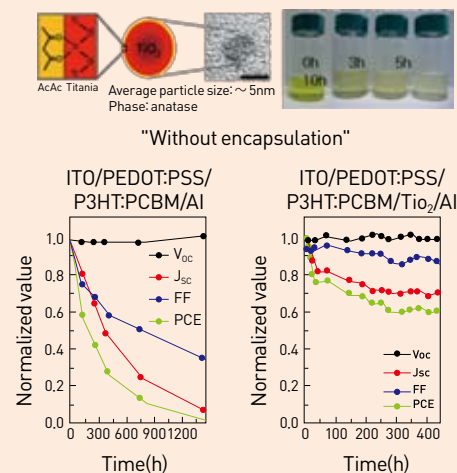
FIGURE 7 Current density-voltage curve of a device employing a low bandgap polymer:PC70BM. The inset shows a flexible OPV cell using a transparent flexible substrate.
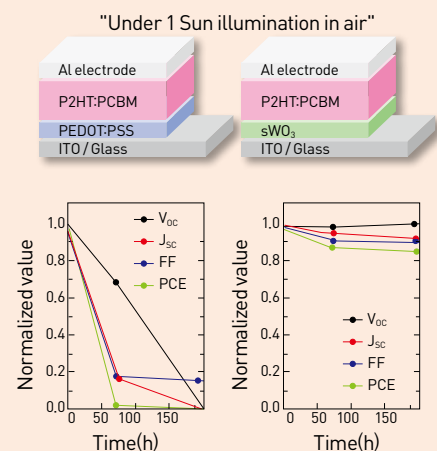
FIGURE 8 Stability test of P3HT:PCBM devices employing PEDOT:PSS (left) or sWO₃ (right) under continuous 1 Sun illumination without encapsulation

FIGURE 9 Stability test of P3HT:PCBM devices employing TiO_2 nanoparticle interlayer without encapsulation

Improvement of stability using interlayers

Intensive studies have been carried out to understand degradation mechanisms and to improve the stability of OPVs. Representative degradation pathways include photo-degradation of organic materials, gradually proceeding phase separation in the active film, oxidation of metal electrode (e.g. Al_2O_3 formation), and instability of poly(ethylenedioxythiophene) doped with poly(styrenesulfonate) (PEDOT:PSS) in the conventional type solar cell.[9] In particular, the PEDOT:PSS layer causes several detrimental effects. First, the PEDOT:PSS is highly hygroscopic. When the PEDOT:PSS layer absorbs water, its conductivity decreases and thus device lifetime shortens. Secondly, the PEDOT:PSS layer is highly acidic (a measured pH of 1.2). Chemical degradation occurs at the interface between ITO and PEDOT:PSS in the presence of water. Third, the PEDOT:PSS is known to be easily photo-oxidized. In order to replace this problematic PEDOT:PSS layer, several metal oxides such as V_2O_5,[10] MoO_3,[10,11] NiO,[12] and WO_3[13,14] have been employed as a HEL in OPVs. OPVs using such layers showed comparable efficiencies to those using the PEDOT:PSS layer. Moreover, they are advantageous compared to the PEDOT:PSS layer since they are neutral, chemically stable, and photo-stable. However, these metal oxide layers have so far been predominantly accessible via sputtering, thermal evaporation, and pulsed laser deposition, which methods are neither scalable nor cost effective. There are only a few reports of solution processed CuO_x,[15] NiO,[16] and V_2O_5[17] as HELs in OPVs.

At KIST, we explored a new kind of solution-processed WO_3 (sWO_3) layer as HEL. Uniform sWO_3 layers were prepared in a controlled manner. The sWO_3 layer allows us to fabricate devices with a structure of ITO/sWO_3/P3HT:PCBM/Al whose PCE is comparable to that of devices employing the PEDOT:PSS layer. Further, we observed considerably improved air/photo-stability of devices compared to the PEDOT:PSS layer (Figure 8). Besides hole extraction layers, we have developed an excellent electron extraction layer of TiO_2 nanoparticles.[18] Though we originally synthesized and applied TiO_2 nanoparticles to enhance electron extraction, we also found that there are several other advantages of TiO_2 nanoparticle layers. TiO_2 nanoparticle layers act as a good hole blocking layer because of their low-lying valence band, thereby reducing charge recombination. Moreover, TiO_2 nanoparticles improve air stability. Figure 9 shows the air stability test result. Since the Al electrode is highly susceptible to oxidation, P3HT:PCBM devices degrade rapidly. However, when TiO_2 nanoparticle layers were inserted in between the photoactive layer and the Al electrode, the degradation was greatly mitigated.

Conclusion

We are making a great effort in the areas of development of photoactive materials and interlayers, and in the improvement of long-term stability to push the PCE high and make OPV cells stable for commercial applications. Building on our previous experience, we are succeeding in upgrading controllability in molecular design and our skills in device fabrication. Moreover, our results employing metal oxide layers as interlayers demonstrated that they have a significant role in charge extraction as well as in enhancing cell stability. Besides the above-presented work, we are investigating unconventional approaches, including organic/inorganic hybrid structures and tandem cells. This research to achieve higher levels of efficiency and stability will continue.

We are taking on, in addition, the challenge of producing large-area OPV cells by printing. We believe our efforts will contribute ultimately to the earlier commercialization of OPVs.

References

[1] Ameri T, Dennler G, Lungenschmied C, Brabec CJ. Energy Environ Sci. 2009; 2: 347-363.

[2] "Global PV Market & Thin Film Solar Trends", Solar & Energy, 2011.

[3] U.S. Energy Information Administration, Annual Energy Review, 2009.

[4] Ma WL, Yang CY, Gong X, Lee K, Heeger AJ. Adv Funct Mater. 2005; 15: 1617-1622.

[5] Li G, Shrotriya V, Huang JS, Yao Y, Moriarty T, Emery K, Yang Y. Nat Mater. 2005; 4: 864-868.

[6] Park SH, Roy A, Beaupre S, Cho S, Coates N, Moon JS, Moses D, Leclerc M, Lee K, Heeger AJ. Nat Photonics. 2009; 3: 297-303.

[7] Wienk MM, Turbiez M, Gilot J, Janssen RAJ. Adv Mater. 2008; 20: 2556-2560.

[8] Chen H-Y, Hou J, Zhang S, Liang Y, Yang G, Yang Y, Yu L, Wu Y, Li G. Nat Photon. 2009; 3: 649-653.

[9] Jorgensen M, Norrman K, Gevorgyan SA, Tromholt T, Andreasen B, Krebs FC. Adv Mater. 2012; 24: 580-612.

[10] Shrotriya V, Li G, Yao Y, Chu CW, Yang Y. Appl Phys Lett. 2006; 88: 073508.

[11] So F, Kim DY, Subbiah J, Sarasqueta G, Ding HJ, Irfan, Gao YL. Appl Phys Lett. 2009; 95: 093304.

[12] Irwin MD, Buchholz B, Hains AW, Chang RPH, Marks TJ. Proc Nat Acad Sci USA. 2008; 105: 2783-2787.

[13] Han S, Shin WS, Seo M, Gupta D, Moon SJ, Yoo S. Org Electron. 2009; 10, 791-797, 2009.

[14] Tao C, Ruan SP, Xie GH, Kong XZ, Shen L, Meng FX, Liu CX, Zhang XD, Dong W, Chen WY. Appl Phys Lett. 2009; 94: 043311.

[15] Lin MY, Lee CY, Shiu SC, Wang IJ, Sun JY, Wu WH, Lin YH, Huang JS, Lin CF. Org Electron. 2010; 11: 1828-1834.

[16] Steirer KX, Chesin JP, Widjonarko NE, Berry JJ, Miedaner A, Ginley DS, Olson DC. Orga Electron. 2010; 11: 1414-1418.

[17] Zilberberg K, Trost S, Schmidt H, Riedl T. Adv Energy Mater. 2011; 1: 377-381.

[18] Chung W-S, Lee H, Lee W, Ko MJ, Park N-G, Ju B-K, Kim K. Org Electron. 2010; 11: 521-528.

Sensitive and Advanced Methods for Detecting Thyroid Hormonal Changes

Jae Chun Ryu
Center for Integrated
Risk Research
• ryujc@kist.re.kr

Youn Jung Kim

Mi Kyung Song

Mee Song

Introduction

The sensitive and tightly regulated feedback control system of thyroid gland autoregulation and the large intrathyroidal and extrathyroidal storage pools of thyroid hormone serve to provide a constant supply of thyroid hormone to peripheral tissues in the face of perturbations imposed by the external environment, chemicals, and a variety of diseases processes. According to the National Health Insurance Corporation (NHIC) of Korea, the number of operations performed to fix thyroid glands, compared to the other most widely performed types of surgery, increased at the steepest rate, up 68% to 38,412 in 2009 from 22,905 in 2006. Although we may not know how many chemicals in today's environment are affecting our health, a number of recent studies have linked changes in thyroid function to a variety of chemicals in our environment. Furthermore, many studies have reported that the hormones in the human body are particularly sensitive to chemicals.

The biosynthesis of thyroid hormone (TH; triiodothyronine [T3] or thyroxine [T4]) can be considered as a six-step process (Figure 1): 1) iodide is transported from the circulatory system into follicular cells by the sodium iodide symporter and converted to iodine; 2) thyroglobulin (Tg) is synthesized and transported to the colloidal space; 3) the tyrosine residues on Tg are converted to mono-iodotyrosine (MIT) and di-iodotyrosine (DIT) by thyroid peroxidase (TPO) in the presence of hydrogen peroxide (H_2O_2); 4) T4 and T3 are formed by the coupling of two DITs or a DIT and an MIT, respectively, on Tg; 5) Tg is endocytosed into follicular cells, degraded by hydrolytic enzymes, and reabsorbed into the cytoplasm, leaving T4, T3, DIT, and MIT in the endosome; and 6) T4 and T3 are released into the bloodstream [1, 2].
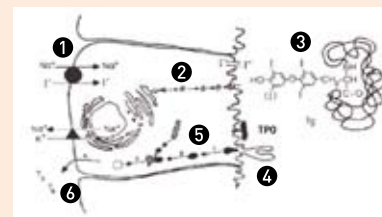
FIGURE 1 A six-step process for the biosynthesis of thyroid hormone [4]

TH synthesis is regulated at several points, including at the level of TPO, iodide transport, type I 5'-deiodinase (5'DI), and the TH receptor (TR) [3].

Classical assays for measuring the disruptive impact of TH on target points *in vitro* and *in vivo* are complex and very time- and labor-intensive. Currently, there are no fast in vitro screening assays for the detection of thyroid-disrupting chemicals. The traditional techniques for identifying interference of targets within the complex regulatory network of TH synthesis by chemicals *in vitro* need improvement. Therefore, omics-based assays have become a useful alternative [5]. Technological advancements using microarray, which is a powerful functional and transcriptomic-based method, in biology and engineering have provided more sensitive, comprehensive, time-effective, and cost-effective approaches that allow for more accurate transcriptomic analysis and identification of classifiers [6]. Omics-based assays offer the possibility of screening for the presence of whole classes of contaminants and toxins based on their biological effects. As a result, such assays are able to detect both known and as-yet-unknown compounds [5].

Here, we present a few examples of sensitive and advanced omics-based screening methods for detecting thyroid hormonal changes caused by environmental chemicals.

Determination of thyroid peroxidase activity in recombinant human cell line, and by microarray technology
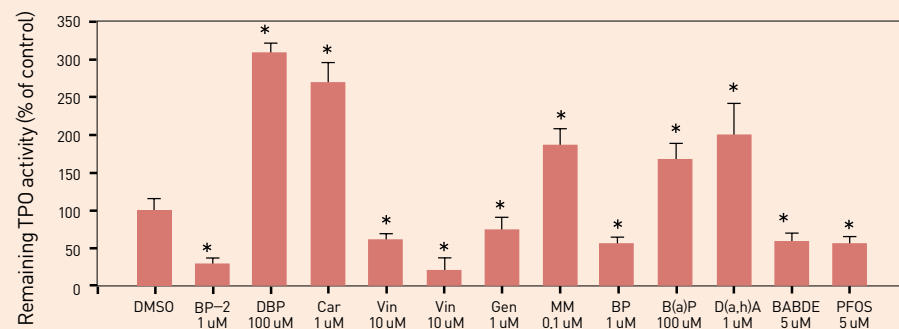
The ability to detect changes in thyroid peroxidase (TPO) activity is important, as TPO represents a primary factor in the thyroid hormone (TH) axis. Decreased TPO activity is indicative of the early stages of hypothyroidism, and increased TPO activity represents potential hyperthyroidism [7]. The guaiacol assay can be used to detect effects on TPO activity, but this assay is complex and time-consuming. This assay requires large amounts of TPO extraction, reaction time, and compounds as well as limited space because of the strong and characteristic smell of guaiacol. Therefore, microarray-based applications to assess the disruption of TPO activity have been conducted. Changes in gene expression that are characteristic of exposure to an environmental chemical can provide an early marker of toxicity, as changes in gene expression are often detectable before histopathological, or clinical indications [8].

This study focused on devising an easy method, using microarrays, to detect disruption of the TH axis [6] in order to identify a set of classifier genes that could be used to build a predictive model capable of accurately categorizing chemicals as TPO inducers or TPO inhibitors. Using transcriptomic-based analysis, we identified and optimized classifier genes based on changes in global gene expression profiles in human follicular thyroid carcinoma (FTC-238) cells expressing human recombinant TPO (hrTPO). This study was conducted to examine the potential utility of transcriptomic endpoints as enhancements to the guaiacol assay for assessing the disruption of TPO activity.

First, we established an *in vitro* guaiacol assay for TPO activity based on hrTPO stably transfected into FTC-238 cells. From this assay, we detected changes in the activity of TPO in response to various chemicals, including benzophenones (BPs), polycyclic aromatic hydrocarbons (PAHs), and persistent organic pollutants (POPs). Benzophenone-2, benzophenone, perfluorooctane sulfonate, bisphenol A bis ether, and vinclozolin all decreased TPO activity, and dibutyl phthalate,

carbaryl, dibenzo(a,h)anthracene, benzo(a)pyrene, and methylmercury increased TPO activity (Figure 2). From these data, we were able to predict the disruption of TPO activity, as a sensitive TH endpoint, by various chemicals.

Second, we devised a simplified method using microarrays to detect changes in TPO activity based on the results from the guaiacol assay. In this study, we used human oligonucleotide chips to examine changes in the gene expression profile of FTC-238 human follicular thyroid carcinoma cells expressing human recombinant TPO after exposure of the cells to TPO activity-disrupting agents. This study identified characteristic gene expression patterns for compounds that stimulated rather than inhibited TPO activity, and showed that these molecular signatures could be used to determine exposure to specific environmental compounds. We identified 362 classifiers that could predict the effect of the compounds on TPO activity with about 70% accuracy (Figure 3). These data indicated that the disruption of TPO activity displayed a robust transcriptomic response upon exposure to TPO activity-disrupting chemicals and yielded a number of responses of comparable sensitivity to the traditional guaiacol assay. These classifiers are potential markers for predicting the effects of chemicals on TH production.

Identification of biomarkers for screening deiodinase-disrupting chemicals

Iodothyronine deiodinase types I, II, and III (D1, D2, and D3, respectively) activate and inactivate thyroid hormones (TH; T3 and T4) through the removal of specific iodine moieties from thyroxine and its derivatives. Prohormone T4 must be converted into the active form, T3, to function in tissues [9]. The conversion of T4 to T3 and the degradation of T3 are important steps in TH regulation [9]. T3 is mainly produced locally from T4 by type 1 (D1) and type 2 (D2) deiodinases [9]. Then T3 is further deiodinated by type 3 deiodinase (D3) [9]. Thus, these deiodinases play vital roles in the physiological effects of TH.
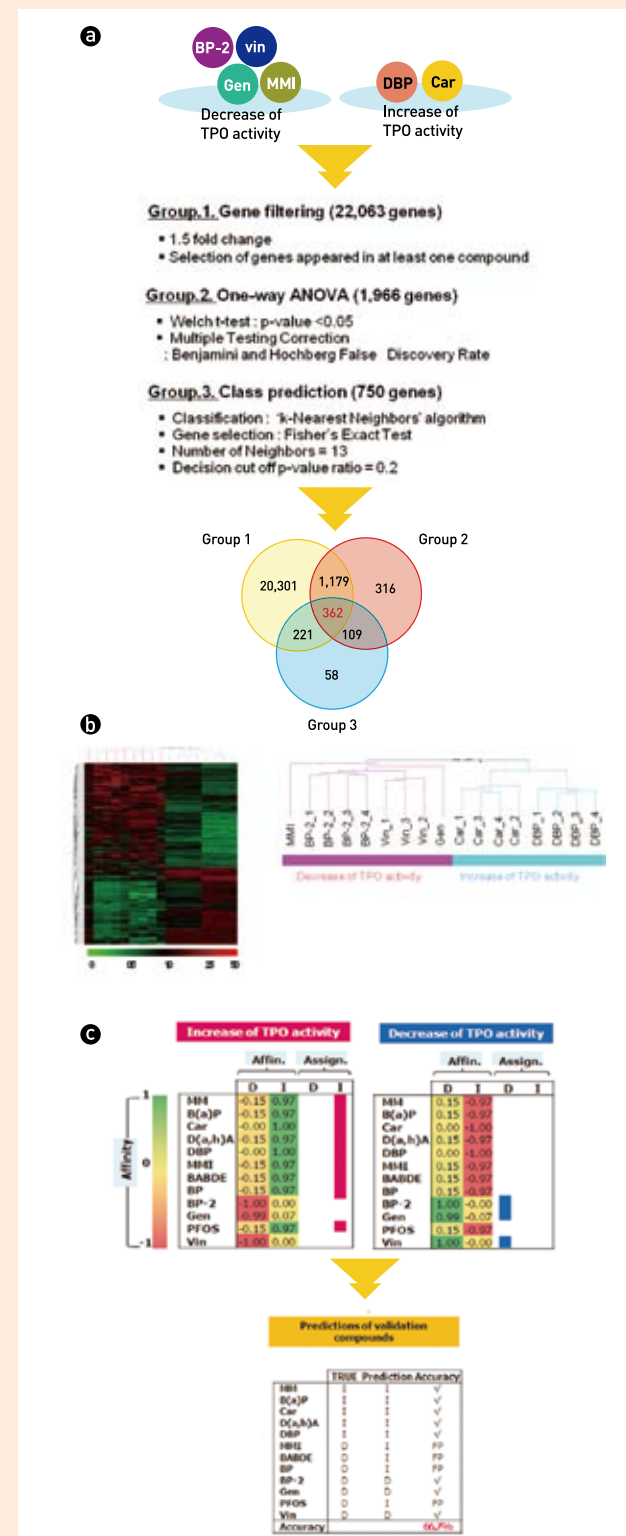
The expression of activating and inactivating deiodinases plays a critical role in a number of cell systems, including the neuronal system, during the developmental as well as adult stages of vertebrates. To investigate deiodinase-disrupting chemicals based on transcriptomic responses, we examined differences in gene expression profiles between T3-treated cells, which represented T3 exposure, and deiodinase-knockdown SH-SY5Y cells, which represented TH deprivation, using microarray analysis and quantitative real-time reverse transcriptase-polymerase chain reaction (RT-PCR)(Figure
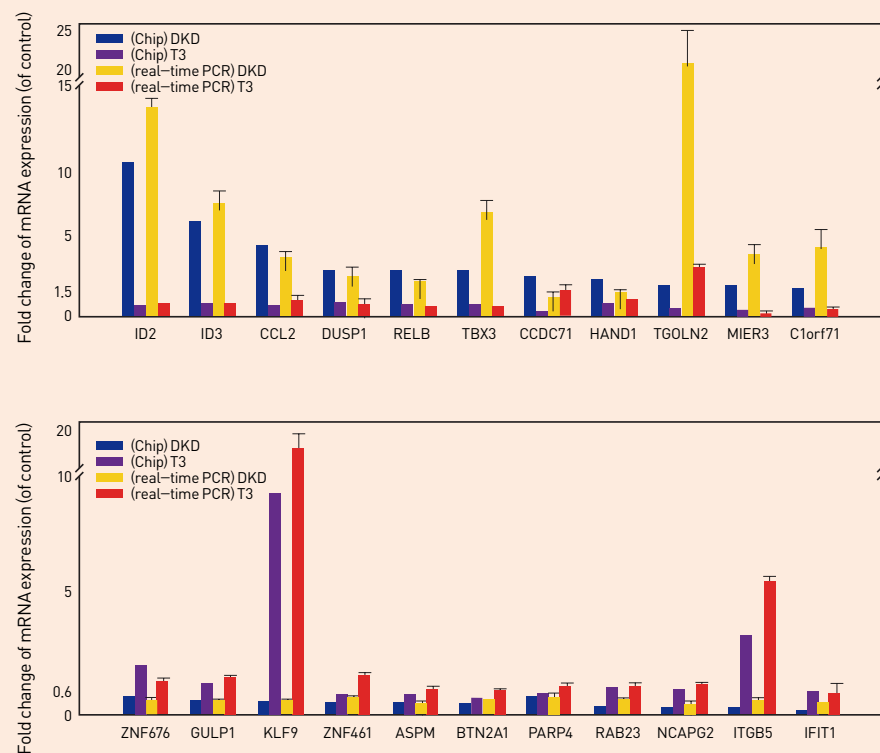
4). A total of 1,558 genes, consisting of 755 upregulated and 803 downregulated genes, were differentially expressed between the T3-treated and deiodinase-knockdown cells [10]. The expression levels of 10 of these genes *(ID2, ID3, CCL2, TBX3, TGOLN2, C1orf71, ZNF676, GULP1, KLF9,* and *ITGB5)* were altered by deiodinase-disrupting chemicals (2,3,7,8-tetrachlorodibenzo-p-dioxin, polychlorinated biphenyls, propylthiouracil, iodoacetic acid, methylmercury, β-estradiol, methimazole, 3-methylcholanthrene, aminotriazole, amiodarone, arochlor 1254, cadmium chloride, dimethoate, fenvalerate, octylmethoxycinnamate, iopanoic acid, methoxychlor, and 4-methylbenzylidene-camphor). These genes are potential biomarkers for detecting deiodinase-disrupting chemicals and predicting their effects on TH production.

Chemical Thyroid Target (CTT)-Array: a gene-based oligonucleotide microarray for rapid detection and identification of thyroid hormone-disrupting chemicals

The aim of this study was to develop an oligo-nucleotide microarray-based approach to the rapid detection and identification of thyroid hormone (TH)-disrupting

FIGURE 3 Identification of discernable molecular markers of TPO activity-disrupting chemicals. (a) Schema of the combination of gene filtering, one-way ANOVA, and class prediction analysis. (b) Dendrogram cluster of toxicants, showing two clusters according to the expression profiles of the 362 predictive molecular markers. (c) Predictions for TPO activity-disrupting chemicals according to TPO activity class in transcription levels. The outcome of the classification is an affinity value to each of the two classes. The affinities of all samples to TPO activity classes are displayed according to the color scales on the left side of each diagram. The right side shows the assignment of each sample to a class on the basis of the affinity. Zero was set as the threshold, and samples with affinities below zero for two classes remained unclassified. MM, methylmercury; B(a)P, benzo(a)pyrene; Car, carbaryl; D(a,h)A, dibenzo(a,h)anthracene; DBP, dibutyl phthalate; MMI, methimazole; BABDE, bisphenol A bis ether; BP, benzophenone; BP-2, 2,2′,4,4′-tetrahydroxybenzophenone; Gen, genistein; PFOS, perfluorooctane sulfonates; Vin, vinclozolin; D, decrease; I, increase; Affin., affinity; Assign, assignment. [6]

FIGURE 2 Disruption of human TPO activity chemical toxicants. BP-2, 2,2′,4,4′-tetrahydroxybenzophenone; DBP, dibutyl phthalate; Car, carbaryl; Vin, vinclozolin; MMI, methimazole; Gen, genistein; MM, methylmercury; BP, benzophenone; B(a)P, benzo(a)pyrene; D(a,h)A, dibenzo(a,h)anthracene; BABDE, bisphenol A bis ether; PFOS, perfluorooctane sulfonates; *, p ← 0.05 compared with control by one-way ANOVA with Dunnett's test. [6]
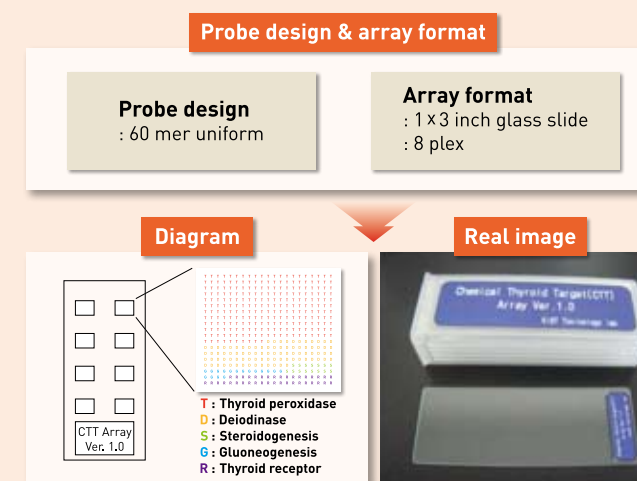
FIGURE 4 Validation of the microarray data by quantitative real-time RT-PCR for deiodinase deficiency-related genes. The mRNA expression levels of (a) upregulated and (b) downregulated genes under deiodinase deficiency were analyzed by quantitative real-time RT-PCR. The expression levels detected by quantitative real-time RT-PCR were generally consistent with the microarray data. The values were normalized to RPLP0, and the relative gene expression values were determined using the 2^{-ΔΔCT} method. The results are expressed as means ± SD of three independent experiments (DKD, deiodinase-knockdown cells; T3, T3-treated cells).

FIGURE 5 Specifications of chemical thyroid target (CTT)-array

of toxins involved, and the output will have relevance for its bioeffect level.

Note
This article is based on our recent paper: Environ Sci Technol. 2011; 45: 7906.

References

[1] Bovee TF, Hendriksen PJ, Portier L, Wang S, Elliott CT, van Egmond HP, Nielen MW, Peijnenburg AA, Hoogenboom LA. Environ Sci Technol. 2011; 45: 8965.

[2] Song M, Kim YJ, Ryu JC. Environ Sci Technol. 2011; 45: 7906.

[3] Gavaret JM, Cahnmann HJ, Nunez J. J Biol Chem. 1981; 256: 9167.

[4] De La Vieja A, Dohan O, Levy O, Carrasco N. Physiol Rev. 2000; 80: 1083.

[5] Ohye H, Sugawara M. Exp Biol Med (Maywood). 2010; 235: 424.

[6] Schmutzler C, Bacinski A, Gotthardt I, Huhne K, Ambrugger P, Klammer H, Schlecht C, Hoang-Vu C, Grüters A, Wuttke W, Jarry H, Köhrle J. Endocrinology. 2007; 148: 2835.

[7] Köhrle J. Thyroid. 2005; 15: 841.

[8] Li Y, Wang N, Perkins EJ, Zhang C, Gong P. PLoS One. 2010; 5: e13715.

[9] Galton VA, Wood ET, St Germain EA, Withrow CA, Aldrich G, St Germain GM, Clark AS, St Germain DL. Endocrinology. 2007; 148: 3080.

[10] Song M, Kim YJ, Ryu WI, Park YK, Ryu JC. Mol Cell Toxicol. 2010; 6: 34.

[11] Song M, Kim YJ, Ryu JC. Mol Cell Toxicol. 2011; 7: 64.

chemicals. From the results of the previous studies, we developed a custom human oligonucleotide microarray, the Chemical Thyroid Target (CTT)-Array, which consists of 440 classifiers targeted to thyroid peroxidase, deiodinase, thyroid receptor, gluconeogenesis, and steroidogenesis in various regulatory targets for TH synthesis (Figure 5). We also attempted to validate the classifiers for each of the TH targets using the CTT Array. Ten TH-disrupting chemicals (2,2′,4,4′-tetrahydroxy-benzophenone, genistein, carbaryl, di-n-butyl phthalate, iodoacetic acid, methylmercury, methimazole, PCB, propylthiouracil, and TCDD) were correctly identified as affecting particular TH targets [11]. This technique offers a reliable alternative to conventional methods for the detection and identification of TH-disrupting chemicals. It can be applied to various TH targets and has higher efficiency and specificity than other screening methods commonly used *in vitro*.

Summary
Thyroid-disrupting environmental compounds are a problem for which a good analytic approach is urgently needed. Omics-based assays can be used as early warning systems for new emerging risks and can also be helpful for characterizing the modes of action of newly detected contaminants. Additionally, this tool will help to develop methods that can be used for high-throughput quality control of environmental agents and for replacement of currently used, unethical, *in vivo* tests. This study demonstrated the ability to detect and identify as-yet-unknown toxic compounds and contaminants. The benefits of this approach are clear: detection might no longer be dependent on *a priori* knowledge of the type and chemistry

Extracellular Electron Shuttle Mediated Biodegradation of Explosive Compounds and Its Application to Multi-Contaminant Removal

Man Jae Kwon
Gangneung Branch
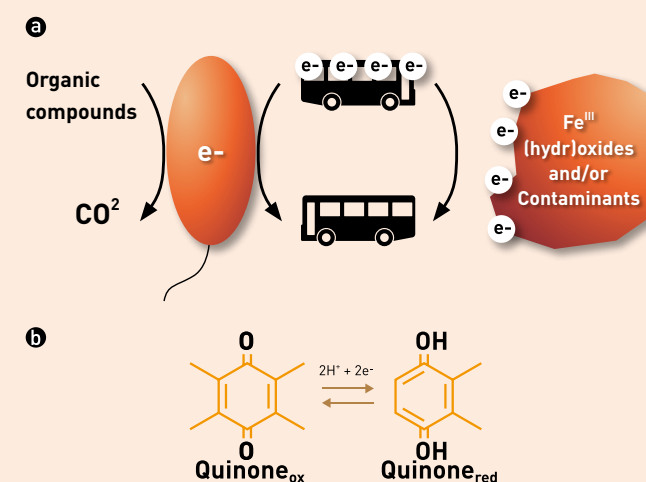• mkwon@kist.re.kr

Yeong Tae Park

Jung Seok Yang

Jae Yeong Choi

FIGURE 1 Schematic diagram showing extracellular electron shuttling between bacteria and Fe^{III} (hydr)oxides (a) and the structures of qunione and hydroquinone (b)

FIGURE 2 Structure of AQDS (a), humic substance (b), RDX (c), HMX (d), and RDX reduction to its nitroso metabolites (hexahydro-1-nitroso-3,5-dinitro-1,3,5-triazine (MNX), hexahydro-1,3-dinitroso-5-nitro-1,3,5-triazine (DNX), hexahydro-1,3,5-trinitroso-1,3,5-triazine (TNX)) through a series of two electron transfers

Introduction

Extracellular electron shuttles (EES) have been proposed as an electron transfer mediator between microorganisms and solid phase minerals to stimulate FeIII reduction by eliminating the need for cell-oxide contact (Figure 1)[1]. Quinones are redox active molecules that cycle between oxidized and reduced forms in biological systems (Figure 1). Quinones accept electrons from lower redox potential electron carriers and transfer the electrons to higher redox potential electron acceptors. Humic substances (HS) and anthraquinone-2,6-disulfonic acid (AQDS), which contain quinone moiety, are often used as a surrogate for natural EES (Figure 2a, b).

Electron shuttling from bacteria can be relevant to in situ remediation strategies since native bacterial communities provide the necessary reducing power, eliminating the need for a bulk reductant within the system [2]. EES are catalytic, and thus are available for numerous oxidation/reduction cycles. This suggests that in situ applications may only require a low concentration of these compounds to stimulate contaminant reduction. In addition, t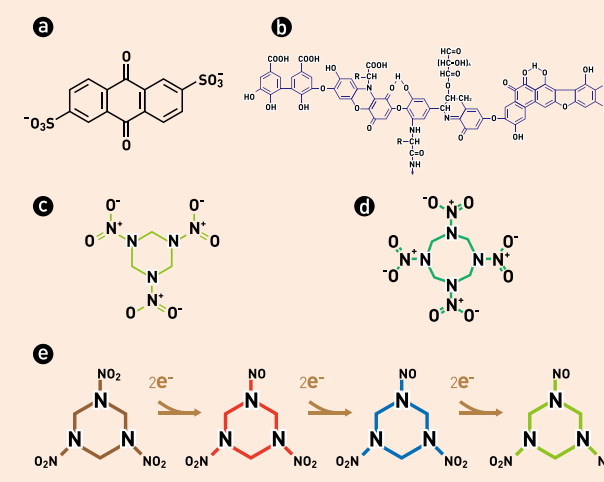he ubiquity of Fe^{III}- and EES-reducing bacteria increases the likelihood that remediation strategies predicated on their physiology will be successful in many subsurface environments.

This article focuses on how EES stimulate the biodegradation of explosive compounds, and what other compounds can be applied for EES-mediated biodegradation. The EES-mediated biodegradation technology is also discussed in terms of applicability and general engineering considerations associated with in situ treatments.

Electron shuttle mediated biodegradation of explosive compounds

The cyclic nitramine explosives hexahydro-1,3,5-trinitro-1,3,5-triazine (RDX) and octahydro-1,3,5,7-tetranitro-1,3,5,7-tetrazocine (HMX) are contaminants at many military sites and live-fire training installations (Figure 2c, d). Groundwater contaminated by these explosives is of growing environmental concern because of human health effects. RDX is a possible human carcinogen, and HMX damages the central nervous system (lifetime health advisory for exposure to RDX and HMX in drinking water is 2 μg/L and 0.4 mg/L, respectively) [3].

Several cost-effective technologies exist for the treatment of explosive compounds in groundwater. Pump-and-treat systems are typically inefficient for the remediation of groundwater plumes largely because they do not address the source of contamination, and because of the large volumes of groundwater that must be treated for hydraulic control and regulatory compliance [4]. Permeable reactive barriers employing zero-valent-iron show promise in treating explosive compounds, but PRB installation is known to be technically and economically infeasible at sites with deep or wide plumes.

Bioremediation is one alternative for explosives contamination and several mechanisms have been proposed using contaminated sediment or soil or pure and mixed cultures. Most studies of explosives bioremediation

have been investigated under anaerobic conditions because subsurface RDX or HMX plumes are mostly anaerobic and these compounds degrade more readily under anaerobic conditions [5, 6]. Similar to an aerobic strategy, several anaerobic bacteria utilized explosives as a nitrogen source. Anaerobic biodegradation through the nitro → nitroso degradation pathway (initial reductive step) has also been suggested as an effective strategy for RDX and HMX degradation [7]. Transformation of RDX through mono-, di-, and tri-nitroso products has been proposed (Figure 2e) [8] and such reduction leads to destabilization, ring cleavage, and mineralization of RDX under anaerobic conditions. Degradation intermediates are susceptible to aerobic as well as anaerobic mineralization; however, mineralization is nearly an order of magnitude greater under anaerobic conditions. Direct bacterial RDX or HMX reduction has been reported [9], and this process can be catalyzed by bacteria that specifically transfer electrons to explosive compounds; however, without these bacteria, the overall biodegradation kinetics will be limited.

Several studies have investigated EES (i.e., HS and AQDS) via fermentative bacteria for explosive transformation [10, 11]. The data demonstrated that EES-mediated bioremediation contributed to potential strategies for the degradation of explosives residues. However, it is unclear whether the specific fermentative bacteria utilized within these experiments are competitive in Fe^{III}-reducing environments contaminated with the explosive compounds. Fermentative bacteria do not gain energy and grow via reactions with EES or FeIII, and may not directly participate in electron shuttling reactions *in situ*. Thus, most recent studies have specifically investigated EES via Fe^{III}-reducing bacteria as one possibility to increase the rate and extent of explosive transformation [12-14].

Fe^{III}- and EES-reducing bacteria have been identified in shallow and deep aquifer material, freshwater [15] and marine sediment [16], soil [17], and extreme environments

such as hot springs and volcanic sediment [18]. The ubiquity of Fe^{III}- and EES-reducing bacteria increases the likelihood that remediation strategies predicated on their physiology will be successful in many subsurface environments [19].

EES increased the rate and extent of RDX transformation in pure culture incubations. Adding EES (i.e., AQDS or HS) to the resting cell suspensions (*Geobacter metallireducens* GS15) increased RDX (or HMX) biodegradation and prevented significant accumulation of the nitroso metabolites relative to electron donor alone, which has been the primary strategy to date [12] (Figure 3a, b). This work was the first to demonstrate EES-mediated RDX (or HMX) biodegradation with environmentally relevant pure cultures. A variety of Fe^{III}- and/or EES-reducing bacteria (i.e., G. *sulfurreducens* PCA, *Anaeromyxobacter dehalogenans* K, *Shewanella oneidensis* MR1, and *Desulfitobacterium chlororespirans* Co23) also reduced RDX (or HMX) most rapidly with EES amendments [13].

The study also investigated EES-mediated RDX biodegradation and the distribution of ring cleavage metabolites generated by biological degradation (cells) versus the products formed by abiotic degradation (reduced EES), and when the two pathways were acting simultaneously [14]. All pathways were influenced by pH. As pH increased, the rates of RDX reduction by AH$_2$QDS also increased (Figure 3c, d). Cells alone reduced RDX faster at the lower pH values. However, at all pH the rates of the EES-mediated pathways were consistently the fastest, and the proportion of carbon present as formaldehyde, which is a precursor to mineralization, was highest in the presence of EES. Understanding the different products formed in the abiotic versus biological pathways and the influence of pH is critical to developing mixed biotic-abiotic remediation strategies for RDX.

Multiple electron transfer pathways for RDX biodegradation in the presence of bioavailable Fe^{III} and EES
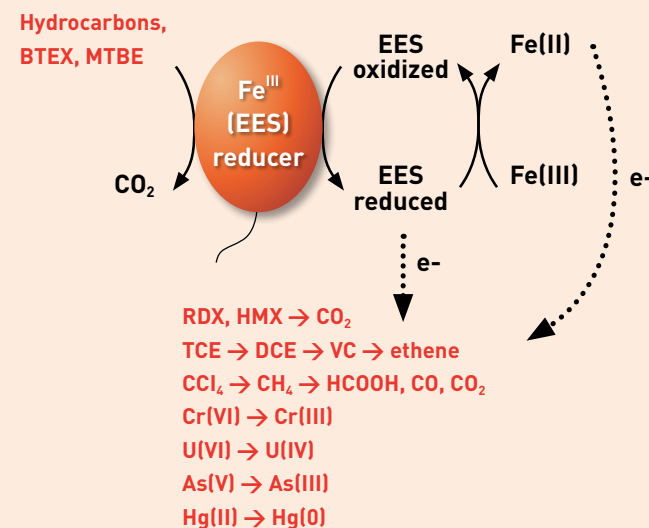
were examined using aquifer material incubations, abiotic experiments, and cell suspensions [20]. EES stimulated RDX reduction in aquifer sediment (Figure 4a). RDX was reduced before onset of significant accumulation of Fe(II) indicating that reduced EES transferred electrons to Fe^{III} rapidly, and Fe(II) generated reduced RDX. This hypothesis was also supported by kinetics experiments; the rate of electron transfer from AH$_2$QDS to Fe(III) (i.e., ferric citrate) was approximately 10^5 times faster than the rate of AH$_2$QDS electron transfer to RDX. There were four possible electron transfer pathways for RDX (or HMX) biodegradation; however, the rates of EES-mediated pathways were consistently the fastest. When the Fe(II)-mediated electron transfer pathway was inhibited with the Fe(II) ligand Ferrozine, the rate and extent of RDX/HMX degradation decreased, but reduction continued. This suggests that multiple electron transfer pathways overlap in the presence of Fe^{III}, but inhibiting one pathway does not deter degradation.

EES also stimulate RDX mineralization in contaminated aquifer sediment [21]. RDX loss was similar in EES-amended and donor-alone treatments; however, the concentrations of nitroso metabolites, in particular TNX, and ring cleavage products (e.g., HCHO, MEDINA, NDAB, and NH$_4^+$) were different in EES-amended incubations. Nitroso metabolites accumulated without EES (i.e., acetate alone). Most notably, 40%-50% of [^{14}C]-RDX was mineralized to ^{14}CO$_2$ in EES-amended incubations (Figure 4b). Mineralization in acetate amended or unamended incubations was less than 12% within the same time frame. The other differences in the presence of EES were the increased presence of 4- nitro-2,4-diazabutanal (NDAB), and the proliferation of Fe^{III}-reducing bacteria. NDAB has previously been identified as an aerobic biological metabolite, or product of abiotic RDX transformation. However, we demonstrated that it was also produced biologically by Fe^{III}-reducing bacteria, including model
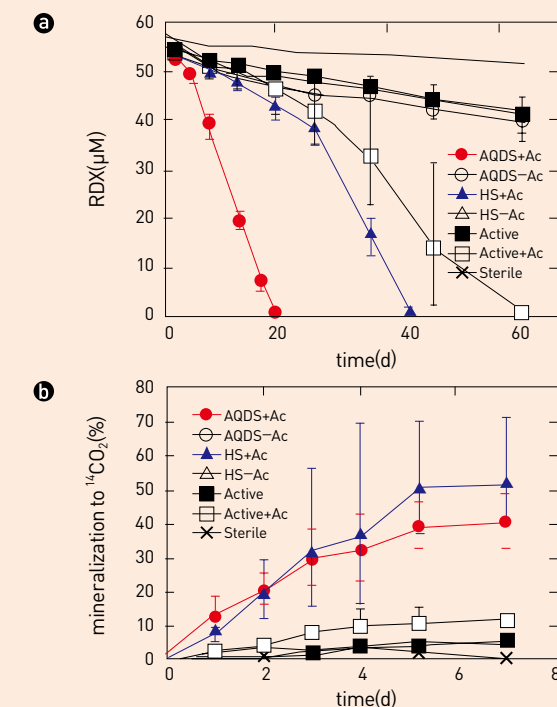
FIGURE 4 RDX reduction in contaminated aquifer material with AQDS (100 μM) or HS (0.15 g/L), and/or acetate (2 mM) (a); reproduced in part with permission from [20]. RDX mineralization in contaminated aquifer material (b); reproduced in part with permission from [21]. U-[14C]-RDX was amended at day 32 of non-radiolabeled RDX experiment. No additional amendments were added or re-added at this time point. Note that the results of (a) and (b) are from two different types of microcosm study. Results are the means of triplicate analyses and bars indicate one standard deviation.

pure cultures. RDX was reduced concurrently with Fe^{III} reduction rather than nitrate or sulfate reduction. Amplified 16S rDNA restriction analysis (ARDRA) indicated that unique Fe^{III}-reducing bacterial communities (β- and ɣ-proteobacteria) predominated in EES-amended incubations. These results demonstrate that indigenous Fe^{III}-reducing bacteria in RDX-contaminated environments utilize EES to enhance RDX mineralization.

Hydrocarbons, BTEX, MTBE

Fe^{III} (EES) reducer

EES oxidized   Fe(II)

CO_2

EES reduced   Fe(III)   e-

e-

RDX, HMX → CO_2
TCE → DCE → VC → ethene
CCl_4 → CH_4 → HCOOH, CO, CO_2
Cr(VI) → Cr(III)
U(VI) → U(IV)
As(V) → As(III)
Hg(II) → Hg(0)

FIGURE 5 Potential of extracellular electron shuttling for the bioremediation of both organic and inorganic contaminants

Future application of electron shuttle mediated biodegradation to multicontaminant removal

Recent studies on EES-mediated explosive biodegradation have provided unique insights into contaminant transport and have aided the development of *in situ* bioremediation technologies for treatment and long-term-stewardship strategies addressing subsurface contamination by explosive compounds. Beside the results of RDX biodegradation introduced in this article, EES-mediated contaminant transformation has also been demonstrated for a variety of inorganic and organic compounds including BTEX compounds [22-24], methyl tert butyl ether (MTBE) [23, 25], carbon tetrachloride [26, 27], chlorinated compounds such as dicholoroethene and vinyl chloride [28], and metals such as uranium [25, 29-32]. This suggests that EES-mediated biodegradation and biotransformation can be applied for various contaminants simultaneously (Figure 5). Most contaminated sites have multiple contaminants of

organic and inorganic compounds such as hydrocarbons, chlorinated compounds, explosives, heavy metals and radionuclides. However, *in situ* bioremediation can be effective only where environmental conditions permit microbial growth and activity; its application often depends on the manipulation of environmental parameters to allow microbial growth and degradation (or transformation) to proceed at a faster rate. In addition, the success of *in situ* bioremediation is highly site dependant.

To control and optimize EES-mediated bio remediation processes, many factors should be considered including the existence of a microbial population capable of degrading or transforming the contaminants, sediment type, temperature, pH, other competitive electron acceptors, and nutrients. In the following section, EES-mediated bioremediation of contaminants is discussed in terms of *in situ* applications.

The presence of indigenous bacteria responsible for contaminant reduction is a key factor in successful bioremediation. Indigenous bacterial communities capable of using Fe^{III} and EES are already present at contaminated sites. The study by Kwon et al (2011) showed that amending an electron donor to aquifer sediment stimulated Fe^{III}-reducing bacterium, *Rhodoferax ferrireducens*, up to 60% (Figure 6). Thus, in situ bioremediation of contaminants may not need to introduce exogenous bacteria into the subsurface.

To be successful, EES-mediated bioremediation requires a procedure for stimulating and maintaining the activity of microorganisms. In other words, *in situ* bioremediation requires a continuous supply of a suitable electron donor and shuttle, and a carbon source for energy and cell material. In addition, these amendments should be added based on the consideration of financial, thermodynamic, and kinetic reasons. There are many commercially or naturally available carbon sources (or electron donors) for *in situ* application.

Various kinds of electron donor can be applied *in situ*. However, there are a number of alternative electron acceptors (e.g., oxygen, nitrate, Mn^{VI}, Fe^{III}, sulfate etc.) that can act as competitors for the electron donor [33]. Thus, careful design is required for selective reduction of these alternative electron acceptors (i.e., concentrations of target electron acceptors that need to be reduced by the electron donor). For instance, since sulfate-reducing conditions may be less favorable for EES-mediated bioremediation of explosives, stoichiometric concentration of the electron donor must be added in order not to stimulate sulfate-reducing bacteria.

The most important factor in EES-mediated bioremediation is the use of suitable EES [12] as the rate and extent of contaminant transformed with EES is much greater than with electron donor alone. For *in situ* applications, Kwon and Finneran (unpublished data) tested different EES to identify an option that is both mechanistically feasible and cost efficient. In this study, raw humics extract and military smoke dyes (Figure 7) increased the rate of RDX reduction relative to cells-only controls for GS15. The results suggest that these quinone-containing compounds could be an alternative source of EES for *in situ* application. Similar to purified humics-amended incubations, adding raw humics extract as an EES stimulated RDX reduction. A slightly lower concentration of raw humics extract, compared

to purified HS, was needed for similar RDX degradation. This suggests that the mulch obtained for this study may have had similar or slightly more HS content initially, and other commercially available sources would likely yield different results. Low molecular weight HS extracted from mulch are soluble and may likely promote the reduction of explosives *in situ*. In addition, low molecular weight HS are relatively benign in that they are naturally derived and catalytic – i.e., only a low concentration is needed to promote these reactions [34]. These data demonstrate the potential for raw HS extracted from mulch to be a source of EES, which may be an economical choice for environmental applications. There are a variety of options for natural EES including river sediment humic or fulvic extracts, and leaf litter extracts [35]. The success of military smoke dye (i.e., Red9) in accelerating the degradation of both RDX and HMX also suggests that other electronegative explosive compounds and heavy metals may be degraded or transformed effectively. Smoke dyes derived from quinone have been extensively used for military purposes. Therefore, the bioremediation strategies predicated on the catalytic effects of these dyes may be a reasonable approach at military sites where explosives and heavy metals are co-contaminated.

The electron donor and EES can be introduced into a hydraulically controlled system to assure that the
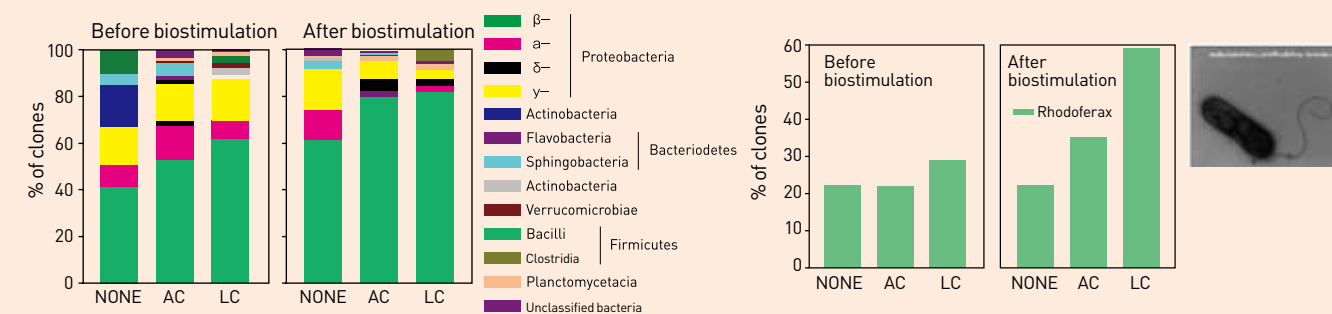
FIGURE 6 Composition of the bacterial community and the population of *Rhodoferax* spp. in contaminated aquifer material before and 25 days after amendment with 2 mM of acetate or lactate (day 59)

Military Smoke Dyes

↑ Purified HS   ↑ Raw HS   Red9
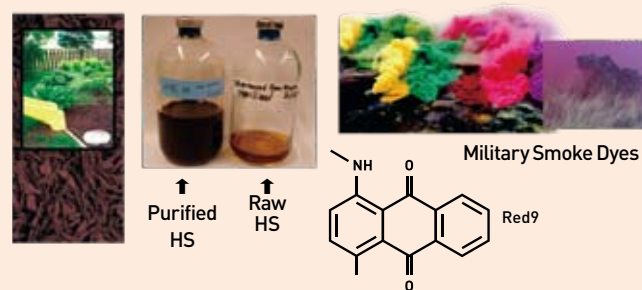
FIGURE 7 Examples of alternative extracellular electron shuttles and the structure of Red9, a military smoke dye, which also contains a quinone functional group.

microorganisms, donor, and EES are in contact with explosive compounds long enough to be utilized. To increase availability of electron donor and EES during the reaction, groundwater can be pumped from recovery wells and inoculated with nutrients, electron donor, and EES, and reintroduced into an upgradient area of the aquifer. Treated groundwater can be returned through injection wells or monitoring wells. The process of a reintroduction procedure will depend on geological settings and geochemical conditions of the sites and local regulations.

The electron donor and EES can also be introduced as a type of Permeable Reactive Barrier Wall. For instance, a mulch wall can be installed on a down gradient from the flow path of contaminated plume. This mulch wall can provide slow distribution of humic material into the contaminant area. In addition, the wall can be mixed with a solid form of electron donor (e.g., chitin as source of acetate). Therefore, the contaminants in the contaminated plume may react with the electron donors and EES from the barrier to break down or transform the contaminants into less harmful products and phases.

pH will also have a marked effect on the biodegradation and biotransformation of contaminants in the presence of EES. Since groundwater pH ranges between 6.5 and 8 in general, EES-mediated biodegradation strategy will work at many sites. However, pH effects on the degradation and transformation of contaminants must be considered

when designing remediation strategies for contaminated sites with extreme pH values (← 5); while EES ultimately facilitates RDX degradation, pH variation will impact the rate of contaminant reduction and transformation.

In summary, EES-use strategies offer many advantages for the decontamination of explosives and other inorganic and organic compounds (e.g., quicker cleanup time, lower cost, easy delivery, environmentally friendly treatment, low maintenance, and risk reduction). The findings in this EES-mediated bioremediation study can join other bioremediation strategies in a growing list of available tools for the engineered cleanup of various contaminated environments. EES-mediated bioremediation may also help remediation scientists and engineers understand the natural attenuation reactions that contribute to contaminant transformation in anaerobic, subsurface environments.

References

[1] Lovley DR, Coates JD, Blunt-Harris EL, Phillips EJP, Woodward JC. Nature. 1996; 382: 445-448.

[2] Schwarzenbach RP, Stierli R, Lanz K, Zeyer J. Environ Sci Technol. 1990; 24(10), 1566-1574.

[3] U.S. Environmental Protection Agency, Washington, DC, EPA 822-R-04-005, 2004.

[4] Abdelouas A, Li Y, Lutze W, Nuttall HE. J Contam Hydrol. 1998; 35, 217-233.

[5] Adrian NR, Arnett CM. Curr Microbiol. 2004; 48(5): 332-340.

[6] Garg R, Grasso D, Hoag G. Hazard Waste Hazard Mater. 1991; 8: 319-340.

[7] Adrian NR, Arnett CM, Hickey RF. Water Res. 2003; 37: 3499-3507.

[8] McCormick NG, Cornell JH, Kaplan HS. Appl Environ Microbiol. 1981; 42(5): 817-823.

[9] Zhao J-S, Halasz A, Paquet L, Beaulieu C, Hawari J. Appl Environ Microbiol. 2002; 68: 5336-5341.

[10] Borch T, Inskeep WP, Harwood JA, Gerlach R. Environ Sci Technol. 2005; 39(18): 7126-7133.

[11] Bhushan B, Halasz A, Hawari J. J Appl Microbiol. 2006; 100(3): 555-563.

[12] Kwon MJ, Finneran KT. Appl Environ Microbiol. 2006; 72(9): 5933-5941.

[13] Kwon MJ, Finneran KT. Soil Sediment Contam. 2008; 17(2): 189-203.

[14] Kwon M, Finneran K. Biodegradation. 2008; 19(5): 705-715.

[15] Lovley DR, Phillips EJP. Appl Environ Microbiol. 1986; 52(4): 751-757.

[16] Hayes LA, Nevin KP, Lovley DR. Org Geochem. 1999; 30(8B): 937-945.

[17] Coates JD, Lonergan DJ, Philips EJP, Jenter H, Lovley DR. Arch Microbiol. 1995; 164(6): 406-413.

[18] Kashefi K, Lovley DR. Science. 2003; 301(5635): 934.

[19] Coates JD, Ellis DJ, Blunt-Harris EL, Gaw CV, Roden EE, Lovley DR. Appl Environ Microbiol. 1998; 64(4): 1504-1509.

[20] Kwon MJ, Finneran KT. Environ Eng Sci. 2009; 26(5): 961-971.

[21] Kwon M, Finneran K. Biodegradation. 2010; 21(6): 923-937.

[22] Lovley DR, Woodward JC, Chapelle FH. Nature. 1994; 370: 128-131.

[23] Finneran KT, Lovley DR. Environ Sci Technol. 2001; 35(9): 1785-1790.

[24] Cervantes FJ, Dijksma W, Duong-Dac T, Ivanova A, Lettinga G, Field JA. Appl Environ Microbiol. 2001; 67(10): 4471-4478.

[25] Finneran KT, Lovley DR, Moyer E. J Contam Soil, Sediment, and Water. 2001; Spring 2001 (Special Oxygenated Fuels Issue): 91-94.

[26] Doong R-A, Chiang H-C. Environ Sci Technol. 2005; 39(19): 7460-7468.

[27] Cervantes FJ, Vu-Thi-Thu L, Lettinga G, Field JA. Appl Microbiol Biotechnol. 2004; 64(5): 702-711.

[28] Bradley PM, Chapelle FH, Lovley DR. Appl Environ Microbiol. 1998; 64(8): 3102-3105.

[29] Boyanov MI, Fletcher KE, Kwon MJ, Rui X, O'Loughlin EJ, Loffler FE, Kemner KM. Environ Sci Technol. 2011; 45(19): 8336-8344.

[30] Jeon BH, Kelly SD, Kemner KM, Barnett MO, Burgos WD, Dempsey BA, Roden EE. Environ Sci Technol. 2004; 38(21): 5649-5655.

[31] Lloyd JR, Lovley DR. Curr Opin Biotechnol. 2001; 12(3): 248-253.

[32] Fredrickson JK, Kostandarithes HM, Li SW, Plymale AE, Daly MJ. Appl Environ Microbiol. 2000; 66(5): 2006-2011.

[33] Kwon MJ, O'Loughlin EJ, Antonopoulos DA, Finneran KT. Chemosphere. 2011; 84(9): 1223-1230.

[34] Lovley DR, Fraga JL, Blunt-Harris EL, Hayes LA, Phillips EJP, Coates JD. Acta Hydrochim Hydrobiol. 1998; 26(3): 152-157.

[35] Nevin KP, Lovley DR. Geomicrobiol J. 2002; 19(2): 141-159.

RECENT PUBLICATIONS

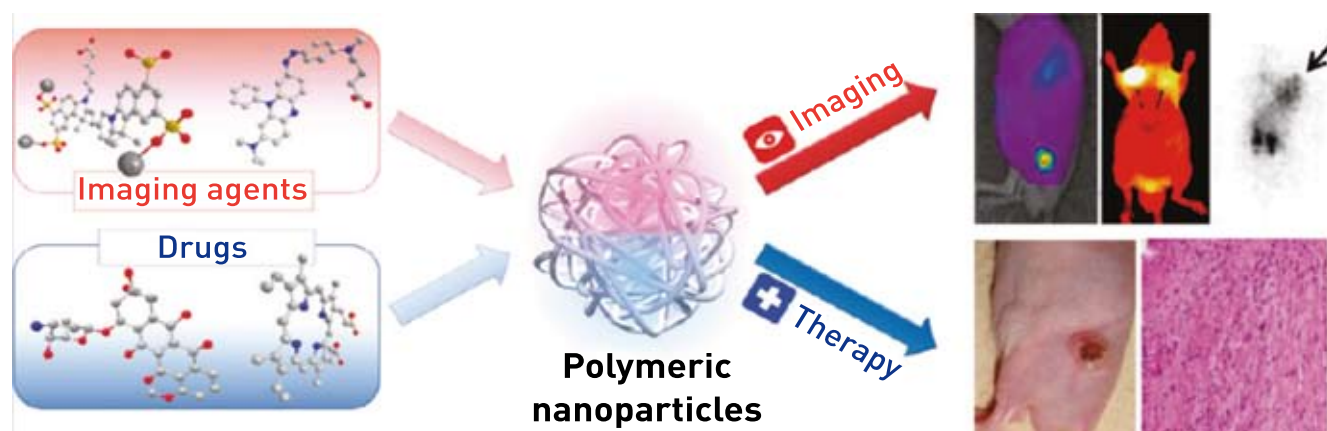## In Vivo Targeted Delivery of Nanoparticles for Theranosis

Heebeom Koo, Myung Sook Huh, In-Cheol Sun, Soon Hong Yuk, Kuiwon Choi, Kwangmeyung Kim, Ick Chan Kwon

Therapy and diagnosis are two major categories in the clinical treatment of disease. Recently, the word "theranosis" has been created, combining the words to describe the implementation of these two distinct pursuits simultaneously. For successful theranosis, the efficient delivery of imaging agents and drugs is critical to provide a sufficient imaging signal or drug concentration in the targeted disease site. To achieve this purpose, biomedical researchers have developed various nanoparticles composed of organic or inorganic materials. However, the targeted delivery of these nanoparticles in animal models and patients remains a difficult hurdle for many researchers, even if they show useful properties in cell culture conditions.

In this article, we review our strategies for developing theranostic nanoparticles to accomplish in vivo targeted delivery of imaging agents and drugs. By applying these rational strategies, we achieved fine multimodal imaging and successful therapy. Our first strategy involved physicochemical optimization of nanoparticles for long circulation and an enhanced permeation and retention (EPR) effect. We accomplished this result by testing various materials in mouse models and optimizing the physical properties of the materials with imaging techniques. Through these experiments, we developed a glycol chitosan nanoparticle (CNP),which is suitable for angiogenic diseases, such as cancers, even without an additional targeting moiety. The in vivo mechanism of this particle was examined through rationally designed experiments. In addition, we evaluated and compared the biodistribution and target-site accumulation of bare and drug-loaded nanoparticles.

We then focused on the targeting moieties that bind to cell surface receptors. Small peptides were selected as targeting moieties because of their stability, low cost, size, and activity per unit mass. Through phage display screening, the interleukin-4 receptor binding peptide was discovered, and we combined it with our nanoparticles. This product accumulated efficiently in atherosclerotic regions or tumors during both imaging and therapy. We also developed hyaluronic acid nanoparticles that can bind efficiently to the CD44 antigen receptors abundant in many tumor cells. Their delivery mechanism is based on both physicochemical optimization for the EPR effect and receptor-mediated endocytosis by their hyaluronic acid backbone.
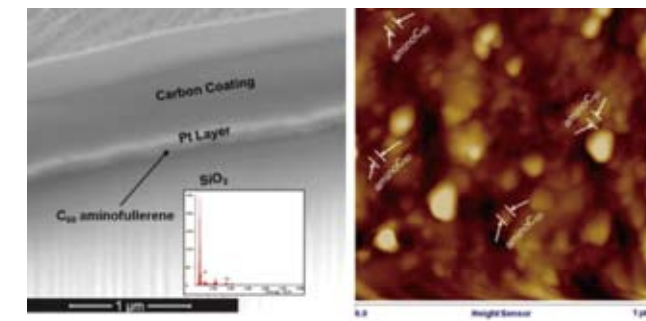
Finally, we introduced a stimuli-responsive system related to the chemical and biological changes in the target disease site. Considering the relatively low pH in tumors and ischemic sites, we applied pH-sensitive micelle to optical imaging, magnetic resonance imaging, anticancer drug delivery, and photodynamic therapy. In addition, we successfully evaluated the in vivo imaging of enzyme activity at the target site with an enzyme-specific peptide sequence and CNPs.

On the basis of these strategies, we were able to develop self-assembled nanoparticles for in vivo targeted delivery, and successful results were obtained with them in animal models for both imaging and therapy. We anticipate that these rational strategies, as well as our nanoparticles, will be applied in both the diagnosis and therapy of many human diseases. These theranostic nanoparticles are expected to greatly contribute to personalized medicine involving optimized therapy for individual patients in the near future.
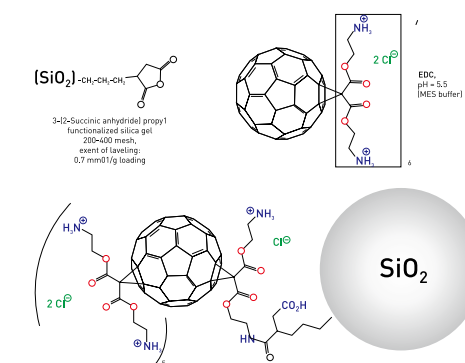

Imaging agents
Drugs
Imaging
Therapy
Polymeric nanoparticles

Cross-sectional (left) and topographic surface images (right) of tetrakis C60 aminofullerene-deposited on the functionalized silica. The small (20 to 60 nm) clusters bracketed in panel (right) appear to be C60 aminofullerene, based on comparison with the surface topology of the bare silica support.

The scheme for tetrakis-aminofullerene immobilization on 3-(2-succinic anhydride)propyl silica gel

Photosensitized Oxidation of Emerging Organic Pollutants by Tetrakis C_{60} Aminofullerene-Derivatized Silica under Visible Light Irradiation

Jaesang Lee, Seokwon Hong, Yuri Mackeyev, Changha Lee, Eunhyea Chung, Lon J. Wilson, Jae-Hong Kim, Pedro J. J. Alvarez

We recently reported that C60 aminofullerenes immobilized on silica support (aminoC60/silica) efficiently produce singlet oxygen (1O2) and inactivate virus and bacteria under visible light irradiation. We herein evaluate this new photocatalyst for oxidative degradation of 11 emerging organic contaminants, including pharmaceuticals such as acetaminophen, carbamazepine, cimetidine, propranolol, ranitidine, sulfisoxazole, and trimethoprim, and endocrine disruptors such as bisphenol A and pentachlorophenol. Tetrakis aminoC60/silica degraded pharmaceuticals under visible light irradiation faster than common semiconductor photocatalysts such as platinized WO3 and carbon-doped
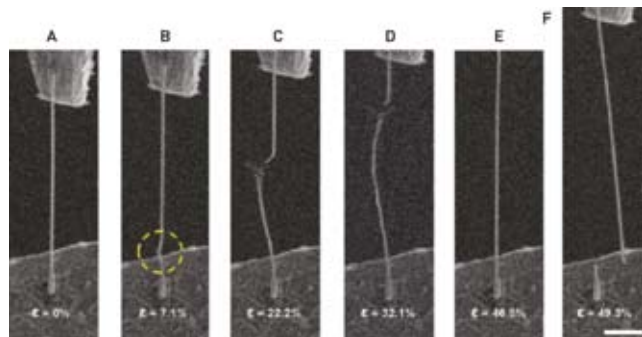
RECENT PUBLICATIONS

TiO2. Furthermore, aminoC60/silica exhibited high target-specificity without significant interference by natural organic matter. AminoC60/silica was more efficient than unsupported (water-suspended) C60 aminofullerene. This was attributed to kinetically enhanced 1O2 production after immobilization, which reduces agglomeration of the photocatalyst, and to adsorption of pharmaceuticals onto the silica support, which increases exposure to 1O2 near photocatalytic sites. Removal efficiency increased with pH for contaminants with a phenolic moiety, such as bisphenol A and acetaminophen, because the electron-rich phenolates that form at alkaline pH are more vulnerable to singlet oxygenation.

Superplastic Deformation of Defect-Free Au Nanowires via Coherent Twin Propagation

Nano Letters, 2011, 11, 3499-3502

Jong-Hyun Seo, Youngdong Yoo, Na-Young Park, Sang-Won Yoon, Hyoban Lee, Sol Han, Seok-Woo Lee, Tae-Yeon Seong, Seung-Cheol Lee, Kon-Bae Lee, Pil-Ryung Cha, Harold S. Park, Bongsoo Kim, Jae-Pyoung Ahn

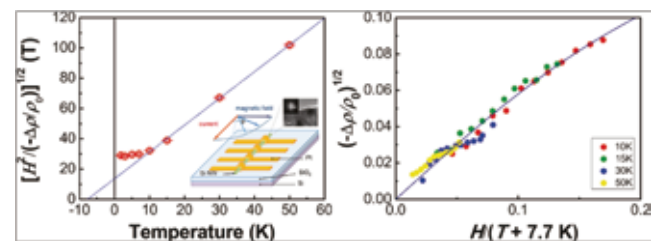We report that defect-free Au nanowires show super-plasticity on tensile deformation. Evidence from high resolution electron microscopes indicated that the plastic deformation proceeds layer-by-layer in an atomically coherent fashion to a long distance. Furthermore, the stress-strain curve provides full interpretation of the deformation. After initial superelastic deformation, the nanowire showed superplastic deformation induced by coherent twin propagation, completely reorienting the crystal from ←110→ to ←100→. Uniquely well disciplined and long-propagating atomic movements deduced here are ascribed to the superb crystallinity as well as the radial confinement of the Au nanowires.

Exchange-Induced Electron Transport in Heavily Phosphorus-Doped Si Nanowires

Nano Letters, 2011, 11, 4730-4735

Tae-Eon Park, Byoung-Chul Min, Ilsoo Kim, Jee-Eun Yang, Moon-Ho Jo, Joonyeon Chang, Heon-Jin Choi

Heavily phosphorus-doped silicon nanowires (Si NWs) show intriguing transport phenomena at low temperature. As we decrease the temperature, the resistivity of the Si NWs initially decreases, like that of metals, and starts to increase logarithmically below a resistivity minimum temperature (T_{min}), which is accompanied by (i) a zero-bias dip in the differential conductance and (ii) anisotropic negative magnetoresistance (MR), depending on the angle between the applied magnetic field and current flow. These results are associated with the impurity band conduction and electron scattering by the localized spins at phosphorus donor states. The analysis on the MR reveals that the localized spins are coupled antiferromagnetically at low temperature via the exchange interaction.

Solution-Processable Reduced Graphene Oxide as a Novel Alternative to PEDOT:PSS Hole Transport Layers for Highly Efficient and Stable Polymer Solar Cells

Advanced Materials, 2011, 23, 4923-4928

Jin-Mun Yun, Jun-Seok Yeo, Juhwan Kim, Hyung-Gu Jeong, Dong-Yu Kim, Yong-Jin Noh, Seok-Soon Kim, Bon-Cheol Ku, Seok-In Na

The preparation of a reduced graphene oxide (pr-Go) with a novel p-TosNHNH2 reducing agent is demonstrated for use as an efficient anode interfacial layer for high-performance
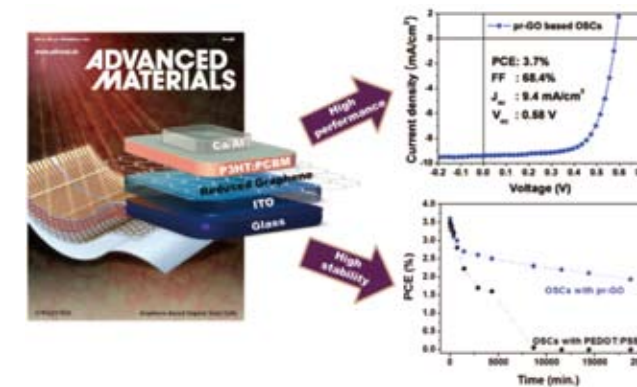

Schematic representation of organic solar cells fabricated using solution-processed pr-GO thin films as hole transport layers
Current density-voltage characteristics of the cell with pr-GO hole transport layer
Changes in PCE of a conventional PEDOT:PSS based OSC and an OSC with the pr GO hole transport layer during exposure to air

and high-stability organic solar cells (OSCs). The efficiency of the cells with pr-GO is highly comparable to those of PEDOT:PSS-based devices. Furthermore, the pr-GO-based OSCs show a much longer cell life in air stability tests in comparison with PEDOT:PSS-based cells.

Tumor-Targeting Gold Particles for Dual Computed Tomography/ Optical Cancer Imaging

Angewandte Chemie International Edition, 2011, 50, 9348~9351

In-Cheol Sun, Dae-Kyung Eun, Heebeom Koo, Chang-Yong Ko, Han-Sung Kim, Dong Kee Yi, Kuiwon Choi, Ick Chan Kwon, Kwangmeyung Kim, and Cheol-Hee Ahn*
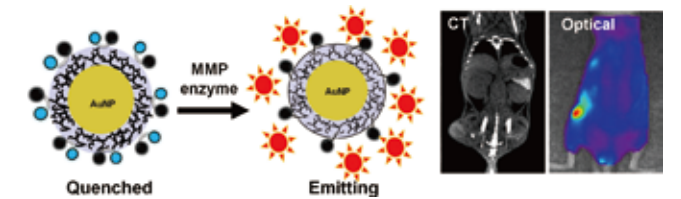
We developed a dual imaging probe with gold nano-particles (AuNPs) for computed tomography (CT) and optical imaging. The excellent stability, selective tumor targeting, enhanced X-ray absorption and MMP-activatable fluorescence recovery was achieved by surface modification of AuNPs with glycol chitosan and MMP substrate with fluorescent dye. It provided accurate anatomical information of tumors in CT images as well as sensitive locational information with optical images. Therefore, this gold nanoprobe is expected to provide a platform for multimodal imaging probes for cancer detection and various other applications.
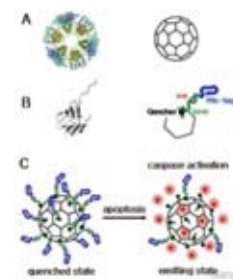
NEW PATENTS

Fusion Protein Comprising Small Heat Shock Protein, Cage Protein Formed Thereby, and Novel Use Thereof

WO11/162492

Ahn, Hyung-Jun
• hjahn@kist.re.kr

The present invention relates to a fusion protein comprised of a small heat shock protein, a cage protein formed thereby, and the novel use thereof; specifically, a fusion protein comprised of a small heat shock protein, a recognition site of a protease, and a histidine polymer, wherein the recognition site and the histidine polymer are sequentially linked to a carboxyl terminal of the small heat shock protein, a cage protein formed thereby, and the novel use thereof. The fusion protein of the present invention and a cage protein formed by the self-assembly properties of the fusion protein are not cytotoxic, and emit a fluorescence signal of about 20 to 50 times higher than a single peptide for conventional molecular imaging per unit of protein. Additionally, cell permeability is very excellent, making it effective for use as a biosensor or a bioactive material carrier.
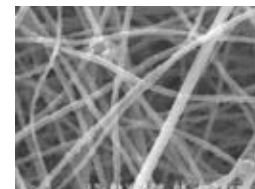
Schematic diagram of a Hsp cage as a multifunctional scaffold for the integrated tumor accumulation and caspase sensing in vivo. Genetically and chemically modified Hsp cage remains quenched in the absence of caspase but visualizes activation of caspase by emitting fluorescence signals.

Ultrafine Continuous Fibrous Ceramic Filter and Method of Manufacturing Same

U.S. 20110266213

Jo, Seong Mu
• smjo@kist.re.kr

An ultrafine continuous fibrous ceramic filter, which is comprised of a filtering layer of a fibrous porous body, wherein the fibrous porous body is comprised of continuous ultrafine fibers of metal oxide which are randomly arranged and layered, and powdery nano-alumina incorporated into the ultrafine fibers or coated thereon, the ultrafine fibers being obtained by electrospinning a spinning solution comprised of a metal oxide precursor sol-gel solution, and optionally, a polymer resin, and sintering the electrospun fibers, in which t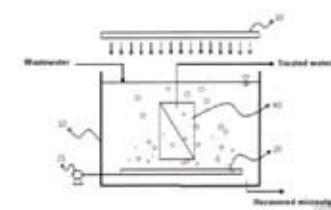he ultrafine fibers have an average diameter of 10~500 nm, and the fibrous porous body has a pore size of maximum frequency ranging from 0.05 to 2 μm, exhibits high filtration efficiency at a high flow rate, and can be regenerated.

Alumina/silica ultrafine fiber-based ceramic filter incorporated with nanoalumina

Device for Treating Wastewater Comprising Nitrogen and Phosphorus and a Method for the Same

U.S. 20110247977

Song, Kyung Guen
• kgsong@kist.re.kr

Disclosed is a device for treating the nitrogen and phosphorus present in wastewater, composed of an algal culture tank for culturing microalgae capable of treating nitrogen and phosphorus in wastewater and a separation membrane for separating thus treated water from the microalgae, and a method for the same. According to the disclosed device and method, microalgae are cultured at high concentrations using wastewater, instead of an artificial culture medium, as a culture medium. As a result, nitrogen and phos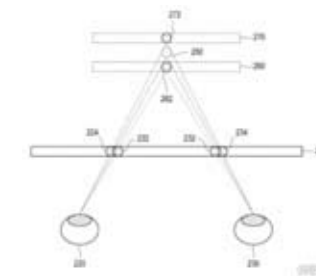phorus can be effectively treated in wastewater, and the microalgae, which are useful as biomass, may be cultured and recovered stably.

Apparatus and Method for Displaying Three-Dimensional Images

U.S. 20110187831

Kim, Sung Kyu
• kkk@kist.re.kr

According to the present invention, there is disclosed a method and device for displaying a 3-dimensional image which may provide improved depth perception. The method is comprised of forming parallax images for the left and right eyes, each of the parallax images including a plurality of images corresponding to images at different depths for the same object; controlling image brightness for each of the parallax images for the left and right eyes; and displaying the parallax images for the left and right eyes.

Method for Producing a Membrane-Electrode Assembly for a Fuel Cell

U.S. 20110240203

Cho, Eun Ae
• eacho@kist.re.kr

Disclosed is a method for producing a membrane electrode assembly for a fuel cell, including: dispersing a catalyst and a conductive binder into a dispersion solvent to provide catalyst slurry; subjecting the catalyst slurry to stirring, sonication and homogenization; applying the catalyst slurry onto a substrate, followed by drying; transferring the substrate coated with the catalyst slurry to either surface or both surfaces of an electrolyte membrane to form a catalyst layer; dipping the substrate, the catalyst layer and the electrolyte membrane obtained after the preceding operation into liquid nitrogen; and removing the substrate to provide an electrolyte membrane having the catalyst layer formed thereon.
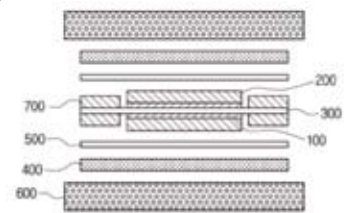
Pharmaceutical Composition Containing Extracts of Native Plants as Active Ingredients for Preventing or Treating Cancer

WO11/052846

Pan, Cheol-ho
• panc@kist.re.kr

The present invention relates to a pharmaceutical composition containing extracts of native plants as active ingredients for preventing or treating cancer, and more particularly, to a pharmaceutical composition for preventing or treating cancer, which contains extracts from native plants as active ingredients, the extracts being obtained from at least one element selected from the group consisting of Adenocaulon himalaicum, Aralia cordata, Astilboides tabularis, Carpesium abrotanoides, Erigeron canadensis, Gymnaster koraiensis, Ligularia fischeri var. spiciformis Nakai, Lythrum salicaria, Oenothera biennis, Rheum undulatum, Rhus trichocarpa and Rosa multiflora. When the native plant extracts of the present invention are treated with Aldo-keto reductase 1B10 (AKR1B10), which is related to acceleration in the growth of cancer cells, the activation of the AKR1B10 is effectively reduced. Accordingly, the pharmaceutical composition of the present invention may be useful for preventing or treating cancer.

2011 Seoul S&T Forum Held
2011. 10. 5~8

The 2011 Seoul S&T Forum was held from October 5 to 8 at Lotte Hotel and KIST in Seoul. The 2nd Seoul S&T Forum was organized in response to Korea joining the OECD DAC in 2009 and the international requests regarding sharing Korea's development experiences. The Forum was aimed at initiating ODA projects and building a cooperative network among 32 developing and developed countries.

The Forum was significant in that it provided a gathering place for discussion among developing and developed countries in Korea, the only country that has transitioned from a recipient to now a donor nation. The Forum also highlighted KIST's contributions to Korea's economic development.

Last year, the 2010 Seoul S&T Forum, themed "International Cooperation of Public Research Institutes for Green Growth," was attended by about 70 leaders of public research institutes.

Nano Truck Delivery
Driving the dream of nano scientists! – KIST offers "Nano Truck Delivery" with cutting–edge nano equipment.
2011.10.15

KIST carried out the "Nano Truck Delivery" program from October 15 to the middle of November, visiting middle and high schools in the local area and introducing cutting–edge nano equipment to the students, for the sharing of scientific technology and knowledge and to make an educational contribution.

"Nano Truck Delivery" is a program for adolescents in local areas where experiencing scientific technology and culture is difficult. The program introduces the students to nano science – which is not included in the normal school curriculum – and let them experience the actual nano world with expensive equipment such as Atomic Force Microscopy (AFM) equipment and Scanning Electron Microscope (SEM).

In addition to introducing cutting–edge nano equipment through "Nano Truck Delivery" to 16 schools in 7 local areas, participating Korean experts in nano science and technology provided special lectures.

For the effective operation of the program and to create sustainable impact, science teachers participated in "Nano Korea 2011" on August 30 and received nano science training; schools wishing to participate were selected per local area.

"Magical 18 Minutes" in Hongreung – First TEDxHongreung
2011.10.29

Hongreung was home to the "empty grave" of Empress Myeongseong. It was also the cradle of development of the Korean economy, realized by KIST's contributions in science and technology and KDI's role in creating effective economic development plans. Prestigious universities such as Korea University, Kyunghee University, and Korea National University of Arts are its neighbors; it also houses the Korean Film Commission, which produced many excellent film directors including Choi Donghoon and Bong Joon–ho. In Hongreung, the home to many of Korea's leading institutions and talented people, the TEDxHongreung event called "Magical 18 Minutes" was held in KIST at 2 pm on October 29. During this event, six speakers with ties to Hongreung shared their memorable life moments and turning points with the audience under the theme "At that moment, I was....." The second speaker was Dr. Park Wanchul of KIST. For 30 years, he had dedicated himself to research on the purification of human and animal excrement. The audience was able to hear his story of various inventions, including septic tank for night soil and wastewater and one using microorganisms, as well as the history of his research up to his current research on native microorganisms. In addition, three more speakers shared about their memorable life moments. When all lectures were finished, the participants shared their thoughts on the lectures in the reception hall. Speakers and participants formed groups and held active discussions. The lectures from TEDxHongreung have been shared with people around the world via the homepage of TED, Youtube, and KISTory (official blog of KIST). This event was held by the office of TEDxHongreung and supported by KIST and Kyung Hee Cyber University.

International Conference for the Tenth Anniversary of KIST IRDA
2011.11.16

Ghana, Nigeria, Costa Rica – this is not the list of participants in the World Cup finals. Rather, these are the home countries of students who applied for admission to the International R&D Academy (IRDA), which has been in operation for 10 years by KIST.

For spring and autumn semesters, IRDA has recruited talented new students and gathered potential scientists and engineers from developing and underdeveloped countries. The acceptance rate to gain admission to IRDA is more than 2.5:1, thanks to the apprentice system and good infrastructure for cutting–edge research, unlike other universities and graduate schools of science and engineering, which suffer from insufficient applicants.

Since 2001, IRDA has produced 147 master's and doctorate degree holders in 21 nations; currently, it educates 118 students from 19 nations. On November 18, on its tenth founding anniversary, 60 alumni who are active in the political, academic, research, and industrial fields were invited to the "International Conference for the Tenth Anniversary of IRDA."

KIST created the IRDA program to promote human resources who will act as a bridge for the cooperation of science and technology with developing nations by implementing a nationwide human resource development project for people in those nations. It continues to foster technical experts who will support international economic activities, commerce, and diplomacy by actively responding to the demands of developing nations wishing to learn from our experience of successful industrial development.

With this huge event for graduates, KIST will create an International R&D Network. "We will develop and select global international joint research agenda based on the graduates of IRDA and establish a multi–dimensional human resource network between graduate–graduate, graduate–student, and graduate–KIST to tackle global agenda such as scientific technology ODA projects with developing nations and global warming," President Kil–Choo Moon said.

Opening of the KIST Global Lounge
2011.12.20

The opening ceremony for the KIST Global Lounge was held on December 20, 2011 at the 2nd floor of Laboratory 2 Building. The Global Lounge was created to foster a pleasant research and working environment for international scientists and students

Many new services include orientations for new international scientists, administrative support, and opportunities for group activities and events.

First KIST–KMSA Research Camp – Introduced biomedical engineering and brain science research to medical students
2012.2.3~2.5

The first KIST–KMSA Research Camp was held at KIST on February 2 (Fri.) ~ 5 (Sun.) with the Korean Medical Student Association (KMSA).

In this Research Camp, 70 students in KMSA including students from Yonsei University, Catholic University, and Korea University formed research groups for seven different research areas (biomaterials, molecular imaging, medical simulation, medical robot, neurobionics, basic neuroscience, and micro medical device) and received training regarding the laboratories, research projects, and research process by the researchers of the biomedical engineering and brain science laboratories at KIST.

In addition, there were special lectures by professors from the Asan Medical Center and Kyungpook National University.

This event was held to encourage medical students to pay more attention to research in basic science, provide an opportunity to maintain close cooperation between KIST and medical researchers, as well as sustain research in related fields.
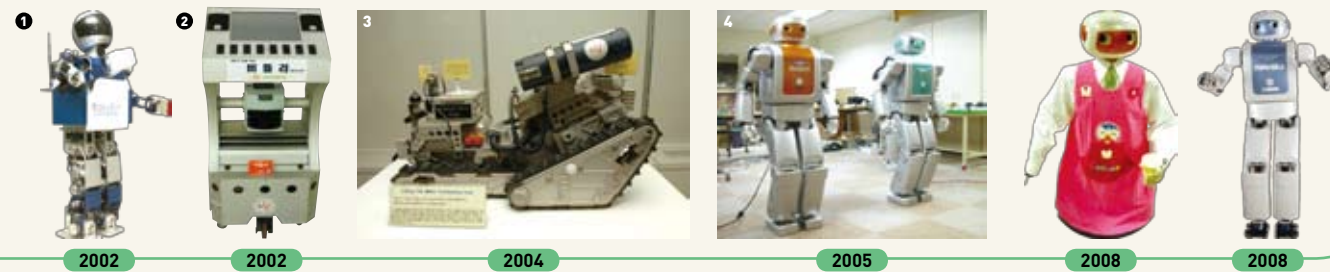
The History of KIST Robots

From robots for home service to robots for hazardous jobs

'Like a Friend, Like a Teacher'

Developed Various Human-Friendly Robots

A variety of robots are being developed, from playful puppy robots to home-cleaning domestic robots to English-teaching robots. Let's take a look at the robots that have been developed at KIST.

Human-Friendly Home Service Robot 'Isaac'

- Developed in order to assist people when using high—tech products, including the Internet, cell phones and PDAs.
- Able to provide Internet—based voice information, intruder detection, autonomous vacuum cleaning, interactions with users through speech input, and vision—based target tracking.

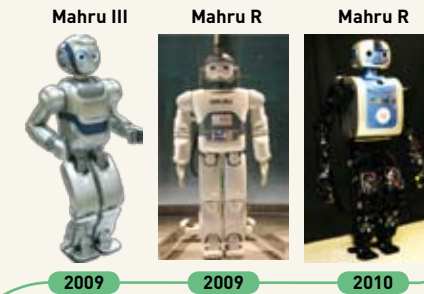2000

❶ Baby Robot 'Babybot'

- Follow—up to Mimot in an endeavor to develop a biomimetic robot.
- Manufactured based on physical data from one—year—olds and the intelligence of three—year—olds in Korea.
- 75—centimeter tall – Korea's first standing robot.

❷ Visitor's Guide Robot 'Butler'

- Manufactured to guide visitors and interact with people.
- Able to recognize the interior environment on its own and navigate autonomously to assist visitors.

❹ Smart Humanoid Robots 'Mahru' & 'Ahra'

- First version of the network—based humanoid, using a different concept from the existing two—legged walking robots.
- Able to recognize human motion and learn from human gestures.
- Able to work with other humanoids by sharing necessary information through a network.
- Continuously being upgraded from Mahru M (2008) ➡ Mahru II (2008) ➡ Mahru III (2009) ➡ Mahru R (2009) ➡ Mahru Z (2010)

Mahru III   Mahru R   Mahru R

2009   2009   2010

❺ Domestic Robot 'Ciros'

- As a research platform robot, it is manufactured to cook and do house chores.
- Autonomously recognizes where to place dishes and when to stop pouring water.
- Able to set the table twice as fast as humans.

❺   ❻
2005   2008

❻ Remotely Controlled Mobile Robot for English Conversations 'Vani'

- Able to be remotely controlled in real time by English native speakers for conversations.
- Equipped with video—based remote control and monitoring functionalities. It has a safety function to limit mobility in case of network error.

2008   2008
❼   ❽

❼ Elder Care Robot 'Sil-Bot'

- Manufactured to assist the silver generation, which consists of the elderly living alone.
- provides simple games and basic information, including weather and transportation information.
- Reborn as an educational robot called 'Engkey' in 2009, after a performance upgrade to be used as tele—type or autonomous—type teaching assistant robot in English, science and math classes. Now it is being developed to be able to provide health & medical information and for Alzheimer prevention programs.
- Used in adult day care centers.

❽ Robot with Various Facial Expressions 'Mero'

- Consists of only a face and a neck in order to maximize facial expressions.
- Able to make human facial expressions using eyes, eyebrows and lips.
- Upgraded from Mero 0.1 (2009) ➡ Mero 2.0 (2011).
- Able to make about a 100 different facial expressions and lip—sync in real time.
- Chosen as one of TIME's 50 best inventions of 2010, along with the English teaching robot 'Engkey.'

Ahra   Mahru   Mahru M   Mahru II

❶ ❷ 3 4
2002   2002   2004   2005   2008   2008

1999

Intelligent Humanoid Robot 'Centaur'

- Korea's first humanoid robot that has both intelligence and the ability to walk using its four legs.
- Has the power to hold an object of up to 1 kilogram. It also has the cognitive ability similar to that of a child, to recognize the surrounding environment on its own.

2000

Biomimetic Robot 'Mimot'

- Developed for biomimetic controlled experiments based on human mechanisms.
- Upper body has a human structure suitable to perform various jobs; lower body has an effective mobile robot structure.

❸ Remotely Controlled Robot Performing Hazardous Jobs 'Robhaz'

- Manufactured to work in dangerous environments in place of humans.
- Able to detect and handle harmful materials and rescue people in disasters, including fires and earthquakes, with the use of a remote control.
- Able to move freely up and down the stairs, steep slopes, and rough terrains. It also has the capability to run down a 45—degree slope or an uneven road at a speed of 12 kilometers per hour.
- Used for military operation in Zaytun Division dispatched in the Iraq War.

2005

Two-Legged Humanoid Robot with Facial Expressions 'Kibo'

- Manufactured to interact emotionally with people.
- Able to perform effective human—robot interaction (HRI) through various facial expressions and lip—synching.
- Continuously being upgraded from Kibo 2.0 (2008) → Kibo 3.0 (2011).
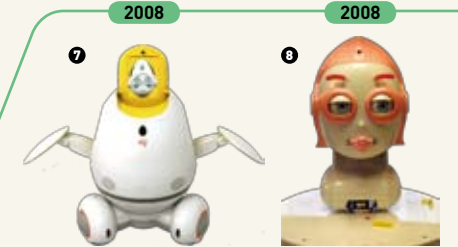
2006

A Celebrity or a Robot? 'Mannequin Robot'

- Developed for display purposes in order to apply the humanoid robot system in actual daily lives, using control technology in the upper body.
- Able to move the upper body, including the neck and arms, and able to move arms according to music. It is also able to act as a helper at an information desk as it recognizes voices.

KIST SCF Lab Seeks Core Technologies for Low—Carbon Green Growth

What is the highest temperature or pressure humans can endure? What if our bodies burn? What if our organs get crushed? Just like any other lab dealing with high temperature or pressure, the Supercritical Fluid Research Laboratory at KIST puts a priority on safety above all else when working with supercritical fluids (any substance at a temperature or pressure above its critical point, where distinct liquid and gas phases do not exist).

Established in 1984, the SCF lab has developed not only core technologies for low—carbon green growth using supercritical fluids but also technologies for commercialization, focusing in the areas of (1) food and medicine extraction, (2) organic particle synthesis, including polymers and drug molecules in drug delivery systems, (3) nano—energy material synthesis, including anode and cathode in secondary cells, (4) breaking down and processing of non—degradable waste, (5) polymer synthesis, (6) manufacturing process of biofuel and biochemical products, (7) hydrogen energy production, and (8) semiconductor cleaning and drying processes.

Through the development of cutting—edge SCF technologies, the KIST SCF lab has produced

numerous thesis publications, patent registrations, and technology transfers, and has engaged in various domestic and overseas activities, including participating at lectures and thesis presentation conferences.

The lab is currently pursuing experiments to create hydrogen energy, which requires the use of hydrogen. What if hydrogen catches fire and spreads? "At first I was scared, because the temperature went up to 700 degrees and the pressure was also quite high, but the safety system works pretty well. I make sure to wear safety gear when doing any experiments," answered Dr. Seung—Ah Park, a researcher in the lab.

So when asked how useful hydrogen energy is, Dr. Jae—Hoon Kim noted that even though many countries are keen on getting energy from hydrogen and devote themselves to research in hydrogen energy, the main issue is price. It needs to be cheaper than crude oil in order to have competitiveness. Despite the difficulties, he says the reason for continuing this research is because "crude oil is limited and we need alternative energy." He continued, "We also do research on renewable energy processes and biofuel synthesis, using hydrogen. It is not easy to compete with the petrochemistry process, but I believe that it has a competitive edge, unless you believe the availability of oil is infinite."

Dr. Kim adds that the process using supercritical fluids works especially well with the synthetic process in which hydrogen is involved. "Biomass contains around 40% water, up to as much as 80%. In order to make use of biomass, the drying process is necessary to remove water. However, it requires significant energy and funds. On the contrary, hydrogen synthesis using supercritical fluids has an advantage because it does not have to remove water from biomass," he said.

This research center has been selected for this special interview among those with a thesis publication featured in the current issue of KISToday, to give a brief introduction of the center and to highlight its various activities, researchers, staff, and/or the working environment.

The Fifth Great Seal of the Republic of Korea: Balancing Art and Advanced Science

The Fifth Great Seal of Korea, symbolizing national sovereignty, was reborn with the help of advanced science and technology.

The Korea Institute of Science and Technology (KIST) created a strong, durable, yet artistic Great Seal by adding the iridium in the gold alloy to improve the color and strength of the seal.

The Seal was made using a combination of KIST's advanced technologies. From the alloy design stage to the testing of the seal, various technologies such as vacuum pressure casting, ceramic shell removal, fabrication of welding rods with electrical discharge machining, activated tungsten inert gas welding, color measurement using CIELab, and non—destructive testing methods were used.

Unlike the previous Great Seals, a feasibility study for its creation was conducted to map out specific plans and procedures. By following the proposed methods and steps, it was possible for the Seal to undergo thorough and proper supervision at each step.